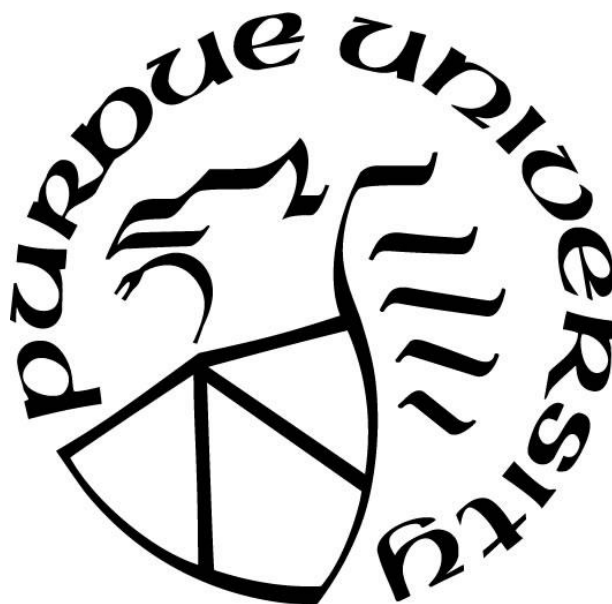# TUNABLE MULTIFUNCTIONALITIES ACHIEVED IN OXIDE-BASED NANOCOMPOSITE THIN FILMS

by

Xingyao Gao

A Dissertation

Submitted to the Faculty of Purdue University

In Partial Fulfillment of the Requirements for the degree of

Doctor of Philosophy

School of Materials Engineering

West Lafayette, Indiana

December 2019

THE PURDUE UNIVERSITY GRADUATE SCHOOL
STATEMENT OF COMMITTEE APPROVAL

Dr. Haiyan Wang, Chair

School of Materials Engineering

Dr. Xinghang Zhang

School of Materials Engineering

Dr. John Blendell

School of Materials Engineering

Dr. Elliott Slamovich

School of Materials Engineering

Approved by:

Dr. David Bahr

Dedicated to all my families

ACKNOWLEDGMENTS

TABLE OF CONTENTS

LIST OF TABLES

LIST OF FIGURES

9

NOMENCLATURE

AFM	Antiferromagnetic
AFM	Atomic force microscopy
AMR	Anisotropic magnetoresistance
CMR	Colossal magnetoresistance
CVD	Chemical vapor deposition
DC	Dielectric current
DE	Double exchange
DME	Domain matching epitaxy
E_c	Coercive field
EDS	Energy dispersive X-ray spectroscopy
EELS	Electron energy loss spectroscopy
E_s	Switching field
ETO	Electrical transport option
FE	Ferroelectric
FFT	Fast-Fourier transform
FM	Ferromagnetic
FMI	Ferromagnetic insulator
FMM	Ferromagnetic metal
FRAMs	Ferroelectric random access memories
FWHM	Full width at half maximum
GMR	Giant magnetoresistance
H	Magnetic field
HAADF	High angle annular dark field
H_c	Coercive field
H_s	Switching field
IP	In-pane
LFMR	Low-field magnetoresistance
M	Magnetization
MBE	Molecular beam epitaxy

14

MBE	Molecular beam epitaxy
ME	Magnetoelectric
MJT	Magnetic tunneling junction
MPMS	Magnetic property measurement system
MR	Magnetoresistance
M_r	Remanent magnetization
M_s	Saturation magnetization
OP	Out-of-plane
PFM	Piezoelectric force microscopy
PLD	Pulsed laser deposition
PM	Paramagnetic
PPMS	Physical property measurement system
P_r	Remanent polarization
P_s	Saturation polarization
PVD	Physical vapor deposition
RSM	Reciprocal space mapping
SAED	Selected area electron diffraction
SC	Supercell
STEM	Scanning transmission electron microscopy
T_c	Curie temperature
TEM	Transmission electron microscopy
T_{MI}	Metal-insulator transition temperature
TMR	Tunneling magnetoresistance
VAN	Vertically aligned nanocomposite
VSM	Vibrating sample magnetometer
XRD	X-ray diffraction

ABSTRACT

Functional oxide-based thin films have attracted much attention owing to their broad applications in modern society. The multifunction tuning in oxide thin films is critical for obtaining enhanced properties. In this dissertation, four new nanocomposite thin film systems with highly textured growth have been fabricated by pulsed laser deposition technique. The functionalities including ferromagnetism, ferroelectricity, multiferroism, magnetoelectric coupling, low-field magnetoresistance, transmittance, optical bandgap and dielectric constants have been demonstrated. Besides, the tunability of the functionalities have been studied via different approaches.

First, varies deposition frequencies have been used in vertically aligned nanocomposite $BaTiO_3$:$YMnO_3$ (BTO:YMO) and $BaTiO_3$:$La_{0.7}Sr_{0.3}Mn_3$ (BTO:LSMO) thin films. In both systems, the strain coupling effect between the phases are affected by the density of grain boundaries. Increasing deposition frequency generates thinner columns in BTO:YMO thin films, which enhances the anisotropic ferromagnetic response in the thin films. In contrast, the columns in BTO:LSMO thin films become discontinuous as the deposition frequency increases, leading to the diminished anisotropic ferromagnetic response. Coupling with the ferroelectricity in BTO, the room temperature multiferroic properties have been obtained in these two systems.

Second, the impact of the film composition has been demonstrated in $La_{0.7}Ca_{0.3}MnO_3$ (LCMO):CeO_2 thin film system, which has an insulating CeO_2 in ferromagnetic conducting LCMO matrix structure. As the atomic percentage of the CeO_2 increases, enhanced low-field magnetoresistance and increased metal-to-insulator transition temperature are observed. The thin films also show enhanced anisotropic ferromagnetic response comparing with the pure LCMO film.

Third, the transition metal element in $Bi_3MoM_TO_9$ (M_T, transition metals of Mn, Fe, Co and Ni) thin films have been varied. The thin films have a multilayered structure with M_T-rich pillar-like domains embedded in Mo-rich matrix structure. The anisotropic magnetic easy axis and optical properties have been demonstrated. By the element variation, the optical bandgaps, dielectric constants as well as anisotropic ferromagnetic properties have been achieved.

The studies in this dissertation demonstrate several examples of tuning the multifunctionalities in oxide-based nanocomposite thin films. These enhanced properties can broaden the applications of functional oxides for advanced nanoscale devices.

1. INTRODUCTION[*]

Oxide-based nanocomposite thin films have attracted extensively research interests owing to their tunable microstructures and functionalities (electric, magnetic, magnetotransport and optical properties), which presents strong potential for device applications. In this chapter, the background of the dissertation, including an introduction of functional oxides thin films (overview, crystal structure and epitaxial growth), the functionalities in functional oxide thin films, the strain engineering in oxide thin films and the motivation of the dissertation are discussed.

1.1 Functional oxide thin films

1.1.1 Overview of functional oxides

From their literal meaning, functional oxides indicate the oxides with functionalities, which are recognized as the potential next-generation electronic materials due to their wide variety of crystal structures and properties. Over the past decades, driven by the development of fabrication and device manufacture techniques, more functional oxides with varies applications have been discovered: The biocompatible oxide Al_2O_3 have been extensively studied in biomedical applications.[1,2] The ferroelectric oxides with high dielectric permittivities, such as $BaTiO_3$ (BTO), $LiNbO_3$ and $Pb(Zr, Ti)O_3$ (PZT) have been widely used in capacitors, sensors and thermistors.[3-8] The transparent conducting oxide ZnO and TiO_2 have been studied in solar cells.[9,10] The single-phase multiferroic $BiMnO_3$ and $BiFeO_3$ can be used in data storage devices.[11,12] The superconducting $YBa_2Cu_3O_7$ (YBCO) and $FeSe$ have been utilized in high temperature superconductors.[13-15] The lithium-based oxides $LiMn_2O_4$ and $LiCoO_2$ have been extensively studied as the cathode for lithium ion batteries.[16,17] Since the functionalities (electrical, magnetic, magnetoelectric and optical properties) of functional oxides are strongly related to their crystal structures, the study of tunable microstructures of functional oxides have attracted extensive research interests.

---

[*] Part of this chapter has been reprinted with permission from *"Ferroelectric thin films and nanostructures: current and future" by J. Huang, X. Gao, J. L. MacManus-Driscoll and H. Wang, Nanostructures in Ferroelectric Films for Energy Applications: Domains, Grains, Interfaces and the Engineering Methods,* (2019). Copyright © Elsevier 2019

1.1.2 Functional oxide thin films

Comparing to their bulk states, the functional oxide thin films, which have the thickness of tens to thousands of nanometers, are meeting the demand of decreasing device dimensions and are more capable in advanced electronic devices. Moreover, the oxide thin film can provide flexible tuning approaches for enhanced functionalities. Strain engineering is one of the most promising methods that can help to enhance the properties of the thin films. For example, in the strained BTO thin film, the ferroelectric transition temperature and remanent polarization can be tremendously increased by 500 ^oC and 250%, respectively.[18] Strain will be generated in the thin films if there are lattice mismatches between the neighboring materials. In epitaxy thin films, strain can be classified into three categories according to its origin: substrate induced strain, multilayer induced strain and vertically aligned nanocomposite (VAN) induced strain. As a comparison, the strain will be relaxed in bulk materials by the formation of defects such as dislocations due to their large dimensions.

In functional oxide nanocomposite thin films, new functionalities, which are generally difficult to obtain in bulk materials or single-phased thin films, can be achieved by combining different materials together. One typical example: multiferroism, which combines two or more ferroic orders (ferroelectricity, ferromagnetism and ferroelasticity) and is rare to find in single-phase materials, is demonstrated in two-phase nanocomposite thin films. The magnetoelectric multiferroic property (ferroelectricity combined with ferromagnetism) can be found in the two-phase thin films by growing a ferromagnetic material together with a ferroelectric material.

In last two decades, tremendous progress of the thin film growth techniques such as pulsed laser deposition (PLD), magnetron sputtering, spin coating and molecular beam epitaxy (MBE) has been made.[19] With the development of these techniques, high quality and precise control of the thin film growth can be achieved.

1.1.3 Crystal structures of functional oxide materials

1.1.3.1 Category of oxides crystal structures

As the properties are strongly correlated to the crystal structures, extensive research has been conducted on the crystallography of the functional oxides. There is a wide variety of crystal structures in functional oxides, which exhibits several unique properties. In functional oxides

(indicating metal oxides in here), the ions and cations are bonded ironically, which can typically be categorized into binary or ternary oxides according to the number of cations in the oxides. Binary oxides occupy different crystal structures including Rock salt, Wurtzite, Fluorite, Antifluorite, Rutile, Curprite and Corundum. Ternary oxides include a series of structures including Perovskite, Spinel, Ilmenite, Layered perovskite, Ruddlesden-popper series, Aurivillius phases and Dion-Jacobson. Table 1.1 shows the representative materials for some commonly studied crystal structures. The schematic drawings in Figure 1.1 and Figure 1.2 illustrate the atomic structure of some binary and ternary oxides.[19]

Table 1.1 Category of common oxide crystal structures

System	Crystal structure	Representative materials
Binary oxides	Rock salt	MgO, MnO, TiO, VO, NiO, SrO, ZrO, CoO
	Wurtzite	ZnO, BeO
	Fluorite	CeO_2, ZrO_2, PrO_2, TbO_2, HfO_2, ThO_2
	Antifluorite	Li_2O, Na_2O, K_2O, Rb_2O
	Rutile	TiO_2, IrO_2, MoO_2, RuO_2, SnO_2, WO_2
	Curprite	Cu_2O, Ag_2O, Pb_2O
	Corundum	Al_2O_3, V_2O_3, Cr_2O_3
Ternary oxides	Perovskite	$SrTiO_3$, $BaTiO_3$, $LaMnO_3$, $La_xSr(Ca)_{1-x}MnO_3$, $BiFeO_3$, $SrRuO_3$, $CaTiO_3$, $BaZrO_3$
	Spinel	$LiTi_2O_4$, $MgAl_2O_4$, $CoFe_2O_4$, $NiFe_2O_4$, $MnFe_2O_4$
	Ilmenite	$FeTiO_3$, $NiTiO_3$, $CoTiO_3$, $MnTiO_3$, $LiNbO_3$, $NiMnO_3$, $CoMnO_3$
	Layered perovskite	$YBa_2Cu_3O_7$
	Ruddlesden-popper series	$A_{n+1}B_nO_{3n+1}$ ($SrRuO_3$, Sr_2RuO_4, $Sr_3Ru_2O_7$)
	Aurivillius phases	$(Bi_2O_2)(A_{n-1}B_nO_{3n+1})$ (Bi_2WO_6, Bi_2MoO_6)
	Dion-Jacobson	$A(A_{n-1}B_nO_{3n+1})$ ($KLaNb_2O_7$, $CsLaNb_2O_7$)
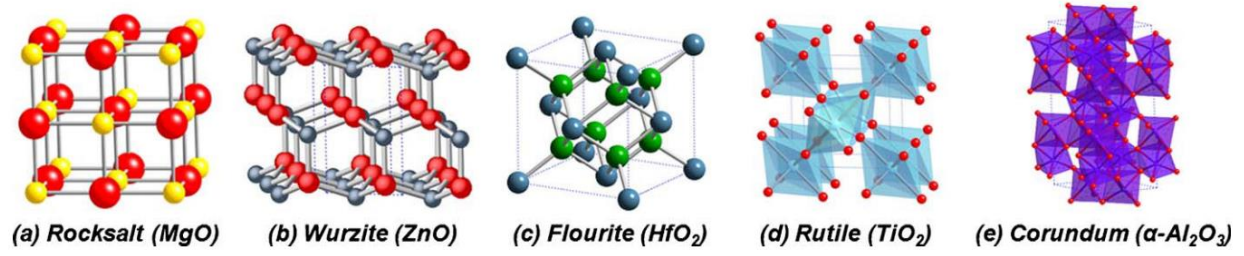
Figure 1.1 Schematic illustration of some common binary oxide crystal structures.[19]
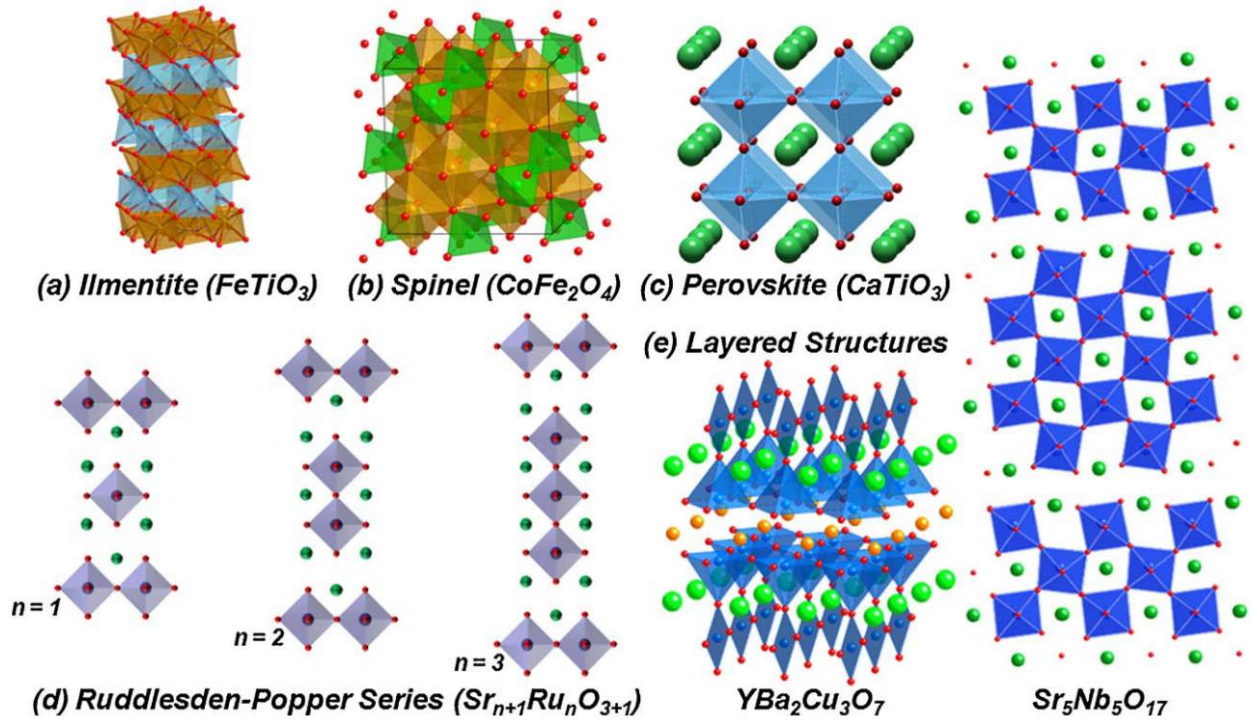
Figure 1.2 Schematic illustration of some common ternary oxide crystal structures.[19]

Among the above functional oxides, perovskite and perovskite-related materials have gained tremendous research interest, which is also the main crystal structure studied in this thesis. Perovskite oxides have either cubic or pseudocubic structure with a formula of ABO_3, while the A cations with larger ionic radius sit at the corners, B Cation sits at the body center and oxygen anions sit at the face centers. The valence states of the A and B cations can have different combinations ($A^{+1}B^{+5}O_3$, $A^{+2}B^{+4}O_3$, $A^{+3}B^{+3}O_3$) to obtain an overall +6 charge. Perovskite materials have shown a variety of physical properties including ferroelectricity, ferromagnetism, multiferroism, magnetoresistance, superconductivity, etc.

1.1.3.2 Crystal structure of BaTiO₃

BTO is one of the most well studied ferroelectric materials, which has the ABO_3 perovskite structure. A Ti cation is located at the center of the unit cell, which is surrounded by the Ba cations at the cube corners and the oxygen anions at the face centers. It has a centrosymmetric cubic structure (space group: *Pm-3m*) and a Curie temperature of around 120 ℃.[20] Between 0 ℃ and 120 ℃, BTO has a non-centrosymmetric tetragonal crystal structure and is ferroelectric. Under the action of an electric field, the Ti cation shifts from the center of the unit cell along the elongated cell direction, leading to polarization.[21] This system has been most widely studied in terms of thin film strain effects on ferroelectricity. The atomic structures of the BTO unit cells are shown in Figure 1.3.
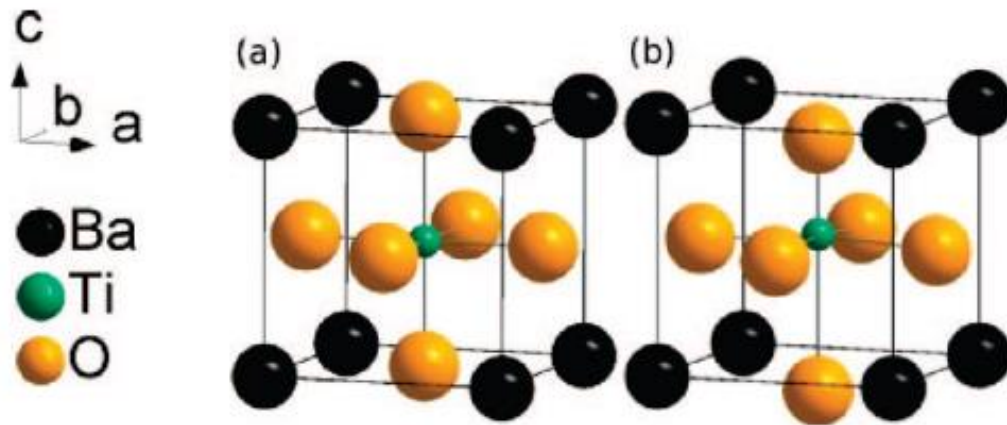
Figure 1.3 Unit cell of BTO with (a) cubic and (b) tetragonal structure.[20]

1.1.3.3 Crystal structure of La₁₋ₓSr(Ca)ₓMnO₃

$La_{1-x}Sr(Ca)_xMnO_3$ belongs to the rare earth manganese oxides with the formula of $RE_{1-x}A_xMnO_3$, where RE indicates the trivalent rare earth elements (La, Pr, Sm, Nd) and A indicates the divalent alkaline earth elements (Sr, Ca, Ba, Pb). $La_{1-x}Sr(Ca)_xMnO_3$ is obtained by doping Sr or Ca cations with the La cations at the A sites of the perovskite $LaMnO_3$. The property of the $La_{1-x}Sr(Ca)_xMnO_3$ varies with the doping level, i.e. the atomic percentage of Sr or Ca atoms in the system. For instance, the $La_{1-x}Sr_xMnO_3$ undergoes a phase transition from ferromagnetic insulator (FMI) to ferromagnetic metal (FMM) with the increasing Sr doping ratio from 0 to 60%. Highest Curie temperature of 360 K and almost 100% of the spin polarization can be obtained as the x increases to 0.3, which leads to the intensive study of $La_{0.7}Sr_{0.3}MnO_3$ (LSMO). Figure 1.4 (a)

shows the atomic structure of a LSMO unit cell and Figure 1.4 (b) shows the phase diagram of the $La_{1-x}Sr_xMnO_3$ with doping levels and temperatures, where highest Curie temperature can be observed when x = 0.3. The ferromagnetic response in the LSMO can be explained by the double exchange (DE) mode proposed by Zener in 1951.[22] The doping of Sr cations results in the valence state change of the Mn cations from +3 to +4 and causes the Mn^{3+}-O-Mn^{4+} interactions, which has better electron delocalization and the magnetic spin alignments.
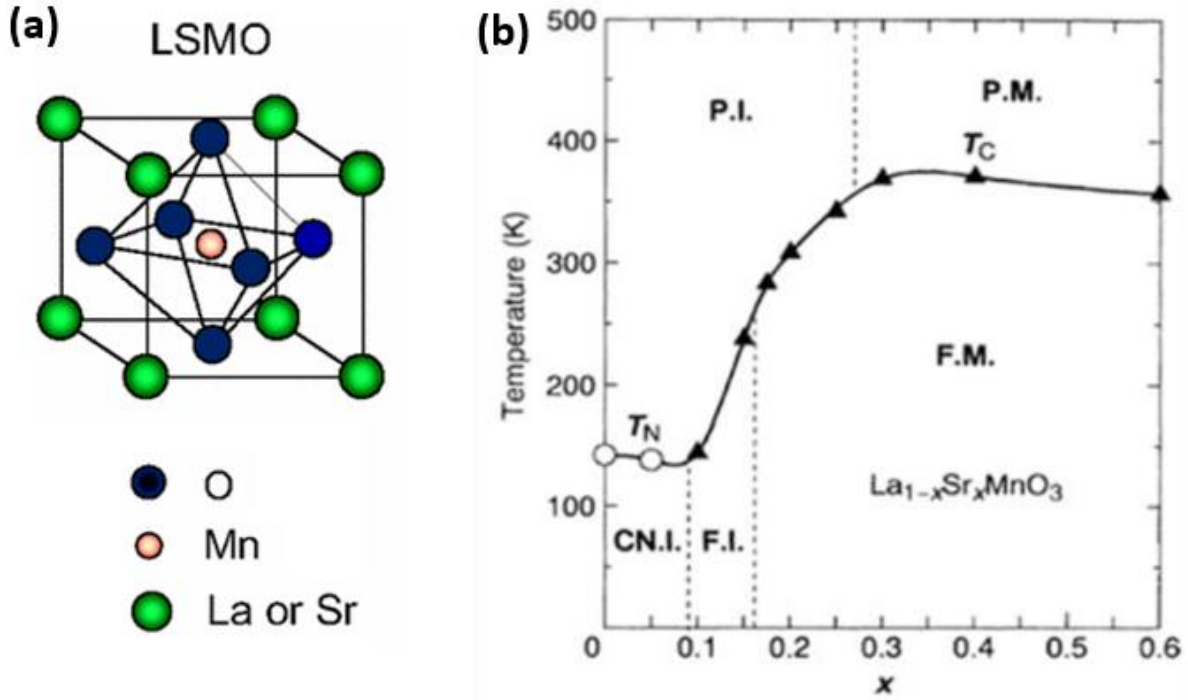
Figure 1.4 (a) Unit cell structure of LSMO (Reproduced from Ref. 23).[23] (b) Phase diagram of $La_{1-x}Sr_xMnO_3$ versus doping levels and temperatures.[24]

1.1.3.4   Crystal structure of CeO₂

CeO_2 has a fluorite crystal structure with a lattice parameter of 5.41 Å. In the CeO_2 lattices, the Ce^{4+} cations locate at the corners and face centers to form a face center cubic, while the O^{2-} anions occupy four octahedral interstitial sites, as shown in Figure 1.5. The structure can also be view as the superposition result from a cubic structured O^{2-} anions with the lattice constant of a/2 and a face centered cubic structured Ce^{4+} cations with the lattice constant of a. From the schematic drawing, it can be seen that each O^{2-} anion is coordinated by four Ce^{4+} cations while each Ce^{4+}

cation is coordinated by eight O^{2-} anions. CeO_2 is a wide bandgap insulator and similar to other fluorite structure oxides, it has high radiation tolerance and high thermal stability.
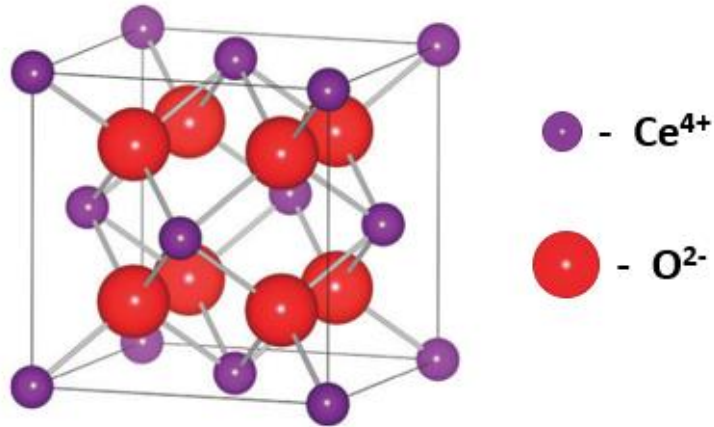
Figure 1.5 Unit cell structure of CeO_2, the red atoms represent the O^{2-} anions and the purple atoms represent Ce^{4+} cations (Reproduced from Ref. 25).[25]

1.1.4 Epitaxial growth of functional oxide thin films

1.1.4.1 Growth techniques of functional oxide thin films

As mentioned above, the exploration of the functional oxide thin films is driven by the development of the integration techniques. There are two representative thin film fabrication techniques, including physical vapor deposition (PVD) and chemical vapor deposition (CVD). PVD is a vacuum-based deposition technique that condenses the physically vaporized material (usually plume or plasma) onto the substrate surface. Some common PVD techniques include Molecular beam epitaxy (MBE), Pulsed laser deposition (PLD), Magnetron sputtering and E-beam evaporation. CVD is based on the chemical reactions of the volatile precursors to deposit the materials onto the substrate surface. Some typical CVD techniques include Atmospheric pressure CVD (ALCVD), Low-pressure CVD (LPCVD), Plasma-enhanced CVD (PECVD) and Metal-organic CVD (MOCVD). However, there are also other fabrication techniques such as liquid phase epitaxy (LPE) and solution-based deposition. Table 1.2 summarized the typical thin film deposition techniques for comparison.

Table 1.2 Comparison of typical oxide thin film deposition techniques

Deposition system	Deposition technique	Operating principle	Advantages	Disadvantages
Physical vapor deposition (PVD)	Molecular beam epitaxy (MBE)	Low energy molecular or atomic beam generated from effusion cells	High epitaxy growth quality, in-situ diagnosis (RHEED), no exhaust gas, no contamination, no residual	Expensive, low efficiency, multiple sources required
	Pulsed laser deposition (PLD)	Plume generated by high-energy laser and target interaction	Simple equipment design, precise stoichiometry control, wide material applicability	Expensive, small deposition area, formation of particulates
	Magnetron sputtering	The target bombard by energetic sputtering gas cations	Precise stoichiometry control, low temperature deposition	High flux of electrons/ions/neutral atoms, substrate heating due to energy input
	E-beam evaporation	The target boiled by high-energy beam	No contamination, wide material applicability	Expensive, imprecise film quality control
Chemical vapor deposition (CVD)	Atmospheric pressure CVD (ALCVD)	CVD at atmospheric pressure	Precise control of film thickness and uniformity	Expensive, low efficiency
	Low-pressure CVD (LPCVD)	CVD at low pressure	High efficiency, cheap, less by-product	Shadowing effect
	Plasma-enhanced CVD (PECVD)	Plasma assisted CVD	Low deposition temperature, high efficiency	No stoichiometry control, introduction of by-product
	Metal-organic CVD (MOCVD)	Metal-organic precursors based CVD	High film growth quality, large deposition area, high efficiency	High deposition temperature, narrow material applicability

Table 1.2 continued

Others	Liquid phase epitaxy (LPE)	Transition of material from the melt to substrate	High film growth quality, high efficiency, growth of multicomponent film	Ultra high deposition temperature, material waste, difficult to obtain thin films
	Solution-based deposition	Transition of material from the liquid to substrate	Simple equipment design, cheap	Imprecise film quality control, limited thickness, small deposition area

1.1.4.2 Growth modes of functional oxide thin films

During the study of the growth mechanisms of the thin films, three major modes are always discussed: the island growth Volmer-Weber mode, the layer-by-layer growth Frank-Van der Merwe mode and the combined Stranski-Krastanov mode, as shown in Figure 1.6.[19] In the island growth mode, the adatoms prefer to bond with each other to form the island clusters other than bond with the substrate, which usually occurs when the film and substrate are the dissimilar materials (metal and semiconductor on oxide substrates). In the layer-by-layer growth mode, the adatoms prefer to bond with the substrate to form a two-dimensional sheet, which is observed during the epitaxial growth of semiconductors and oxide materials. In the combined growth mode, the adatoms first form a planar sheet before the island growth occurs, which happens in the metal-metal or metal-semiconductor systems.
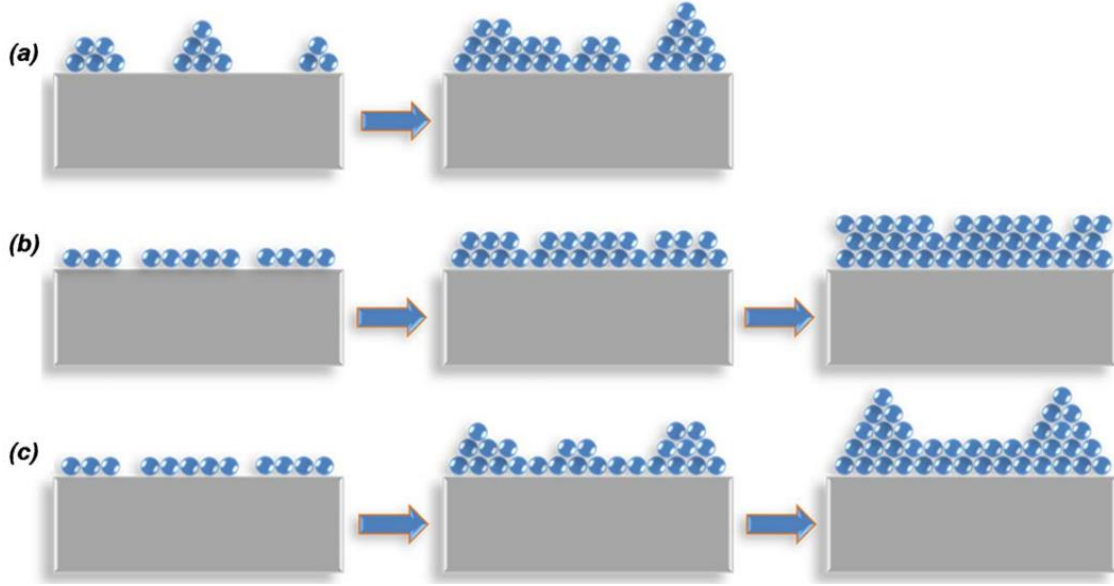
Figure 1.6 Three major thin film growth modes: (a) Volmer-Weber mode (b) Frank-Van der Merwe mode and (c) Stranski-Krastanov mode.[19]

The occurrence of the above-mentioned growth modes can be explained by the equilibrium among the interfacial energies at the nucleation stage during the thin film growth, as described by the equation:

$$\gamma_{sv} = \gamma_{fs} + \gamma_{fv} \cos\theta \qquad (1.1)$$

In this equation, γ indicates the interfacial energy among the substrate (*s*), film (*f*) and vapor (*v*) and θ indicates the wetting angle.[19] The schematic illustration of the model is shown in Figure 1.7. During the island growth, as the wetting angle $\theta > 0$, the interfacial energy relationship would be: $\gamma_{sv} < \gamma_{fs} + \gamma_{fv}$, which leads to the larger surface tension of the film than that of the substrate and the formation of the adatom clusters. However, during the layer-by-layer growth, as the wetting angle θ is close to zero, $\gamma_{sv} \geq \gamma_{fs} + \gamma_{fv}$, which causes the diffusion of the adatoms to wet the substrate surface. In the combined growth mode, the layered growth mechanism is favored at the early stage before it transits to the island growth mode because of the increase of the strain energy generated by the lattice mismatch during the growth.
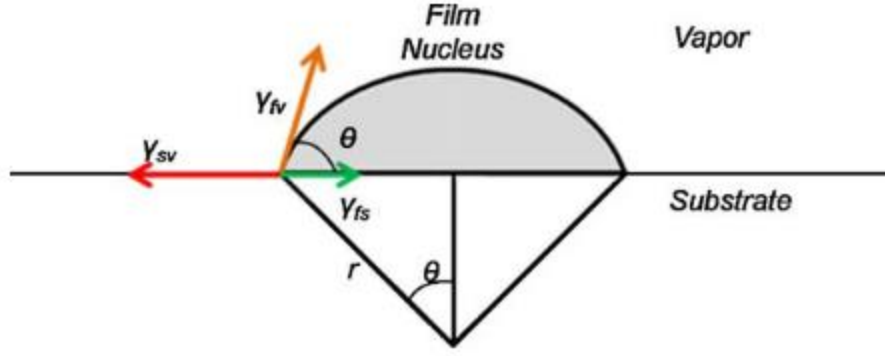
Figure 1.7 Schematic illustration of the atomic nucleation during thin film growth.[19]

1.1.4.3 Epitaxial growth of functional oxide thin films

The concept epitaxy refers to the extended single-crystal film formation on top of a crystalline substrate.[19] This term can be categorized to homoepitaxy and heteroepitaxy based on whether the film is grown on the substrate with the same material. Unlike the homoepitaxial thin films, in which the film and substrate have the same lattice parameters, the film and substrate lattices usually have different dimensions in heteroepitaxial thin films. A term called lattice mismatch f is used to scale this difference:

$$f = 2 \times \frac{a_f - a_s}{a_f + a_s} \tag{1.2}$$

Where a_f and a_s indicate the lattice parameters of the film and substrate, respectively. When $f \sim$ 0, the growth mode is called homoepitaxial film growth or nearly perfectly lattice matched heteroepitaxial film growth, as shown in Figure 1.8 (a). As the lattice mismatch increases (0 to 7%), strain will be generated inside the film to either elongate or compress the lattices towards the lattice parameter of the substrate, which is called strained heteroepitaxial film growth (Figure 1.8 (b)). This strain will be relaxed by the formation of defects (i.e. dislocations, boundaries) as the film thickness reaches certain value, which is called the "critical thickness". As the lattice mismatch continuing to increase (> 7%), the defects will be generated at the interface of the film and substrate to instantly relax the strain, which is called relaxed heteroepitaxial film growth (Figure 1.8 (c)). However, the lattice mismatch could be extensively reduced by the domain matching or the rotation of the lattices in this circumstance.
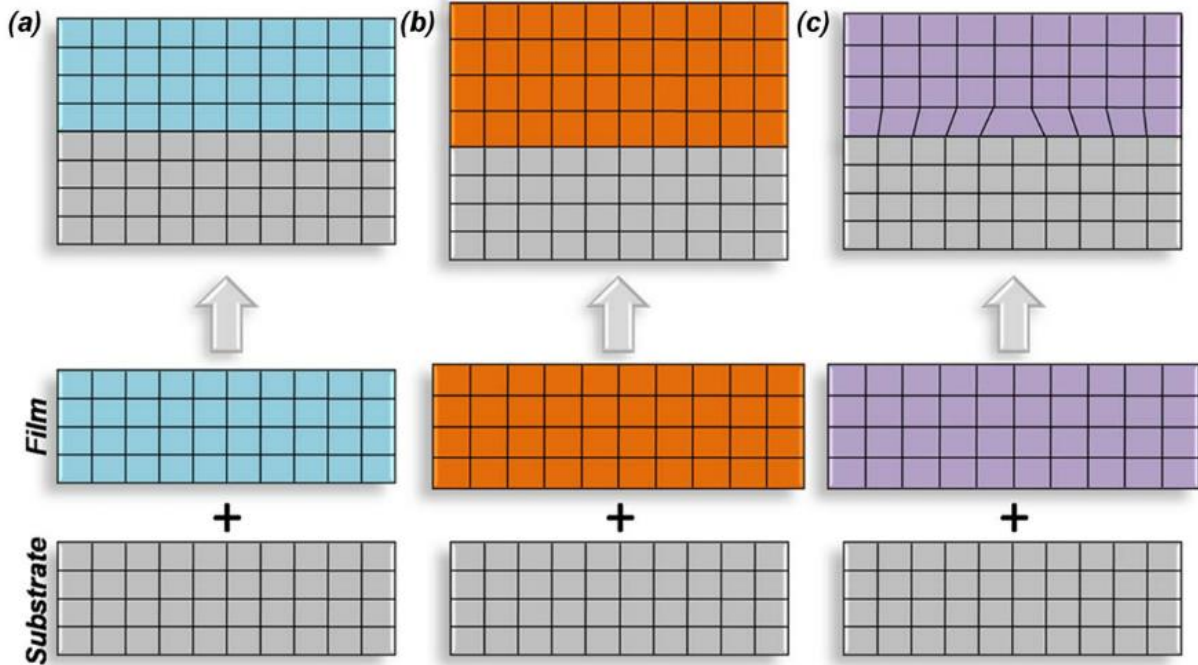
Figure 1.8 (a) Nearly perfectly lattice matched heteroepitaxial film growth. (b) Strained heteroepitaxial film growth and (c) Relaxed heteroepitaxial film growth.

1.2   Functionalities of oxide thin films

1.2.1   Ferromagnetism

Ferromagnetism was first discovered in some permanent metals like iron and that where its name derived from ("ferrum" means "iron" in Latin). Ferromagnetism indicates a physical property that the material has the spontaneous magnetization in the absence of external magnetic field and this magnetization can be inversed by applied magnetic field. The ferromagnetic property can be characterized by a magnetic hysteresis loop, as shown in Figure 1.9.[26] The magnetic moment of the material is a sum of the magnetic moment of each electron in the material, which is originated from the orbital motion and the spin of the electron. In the virgin state, the ferromagnetic material might have a zero net magnetization due to the random alignment of the spins. As a magnetic field is applied, the spins will start to rotate towards their favorable direction (parallel to the magnetic field). A maximum magnetization is achieved when all the spins are oriented parallel to the external field, which is called the saturation magnetization (M_s). The spins will start to rotate towards the opposite direction as a reversed magnetic field is applied. The magnetization retains at a non-zero value as the magnetic field drops to zero, which is called the

remanent magnetization (M_r). A reversed magnetic field is needed to drive the magnetization back to zero, which is named as the coercive field (H_c). The inversed magnetic field applied to orientate all the spins toward the opposite direction is called the switching field (H_s). Ferromagnetic materials can be categorized into "soft" and "hard" ferromagnetics according to the degree of their coercive fields, in which the "hard" ferromagnetic materials are difficult to demagnetize. The ferromagnetic material undergoes a phase transition at its Curie temperature (T_c), where the material becomes paramagnetic above the Curie temperature.
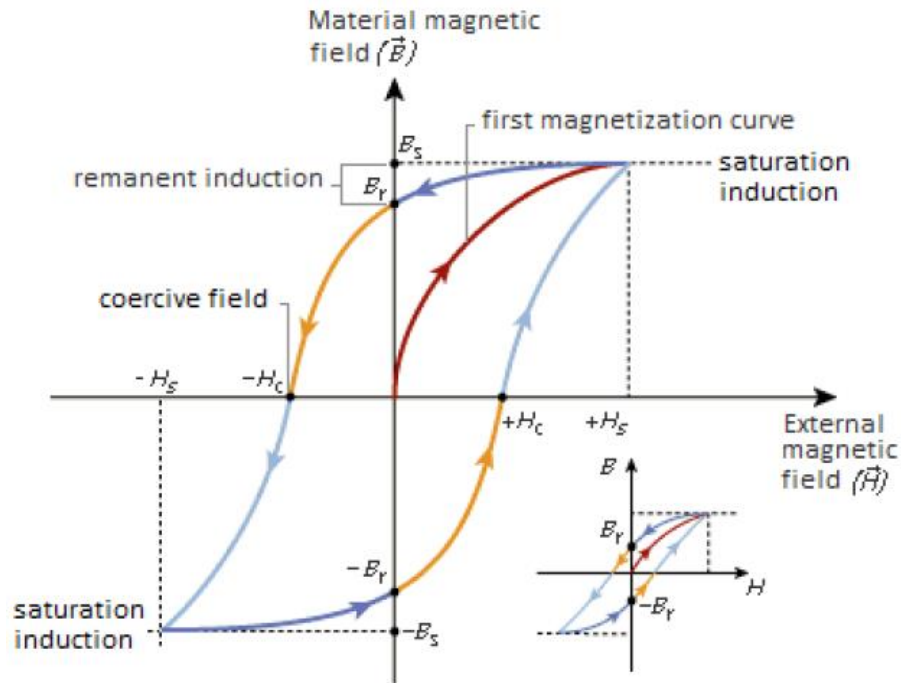
Figure 1.9 Hysteresis loop for ferromagnetic materials.[26]

1.2.2 Ferroelectricity

The history of ferroelectricity can be traced back to 1921, when Joseph Valasek published his discovery that the Rochelle salt showed an electric hysteresis loop when applying an electric field,[27] as shown in Figure 1.10. A hysteresis loop of polarization is plotted when applying the electric field back and forth. This result was "analogous" to the ferromagnetic hysteresis loop reported previously. This property was named as "ferroelectricity" later, as it was analogous to the magnetic hysteresis loop from ferromagnetic iron. In the next hundred years, ferroelectricity has attracted a tremendous amount of interests of scientists and engineers.

30
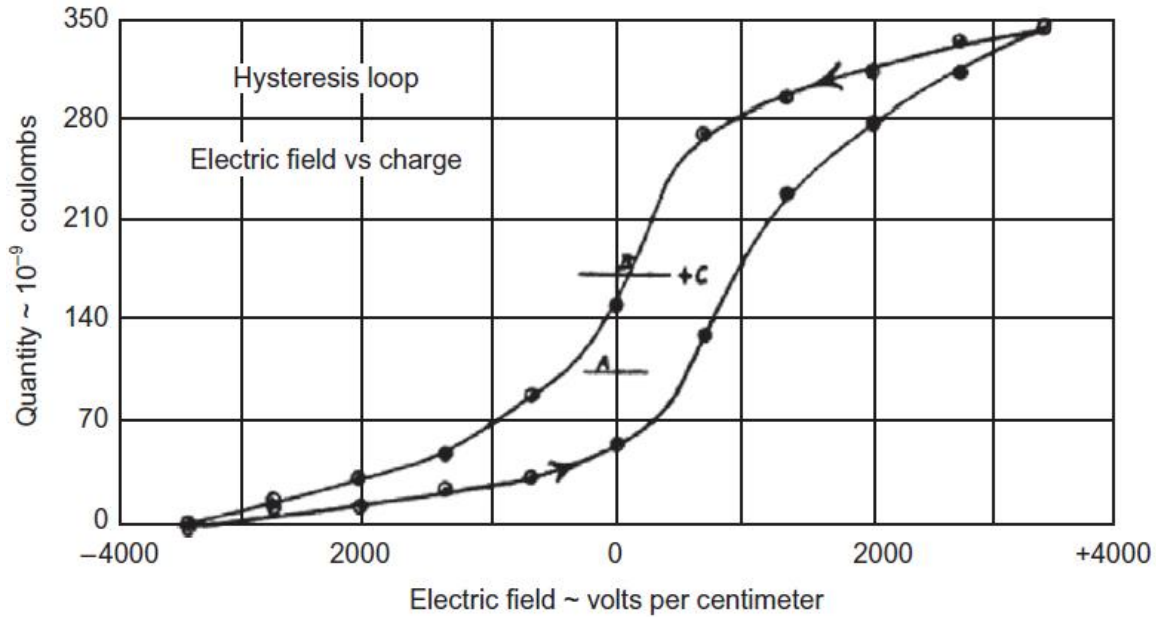
Figure 1.10 The first ferroelectric hysteresis loop published in history, reported by Valasek in 1921 (Reproduced from Ref. 27).[27]

Ferroelectrics indicate the materials that have the spontaneous polarization when an external electric field is applied, which usually occurs in nonsymmetrical crystal structures with the formation of electrical dipoles caused by the shift of the cations or anions. Figure 1.11 shows the atomic structure of a cubic perovskite $Pb(Zr_xTi_{1-x})O_3$ (PZT) or $(Pb_x La_{1-x})(Zr_yTi_{1-y})O_3$ (PLZT), where the ferroelectricity arises from the displacement of the central cation in six directions (up, down, forward, back, left and right).[28] In ferroelectric materials, the dipoles are randomly aligned with a zero net polarization at the virgin state. As the electric field increases, the dipoles begin to orient with the applied field, and saturation (P_s) is achieved when all of the dipoles are aligned in the same direction, which is the highest point of the ferroelectric hysteresis loop. Unlike dielectric and paraelectric materials, the polarization of ferroelectrics remains at the same value at zero field, which is called the remnant polarization (P_r). When an opposite electric is applied, dipoles begin to rotate to follow the reserved field direction until all of the dipoles are aligned in parallel with the electric field. The coercive field (E_c) indicates the electrical field to drive the net polarization to zero and the switching field (E_s) is the electrical field to align all the dipoles to the opposite direction. When the material is heated up to the Curie temperature, the ferroelectric becomes as paraelectric, which usually accompanying with a phase change.
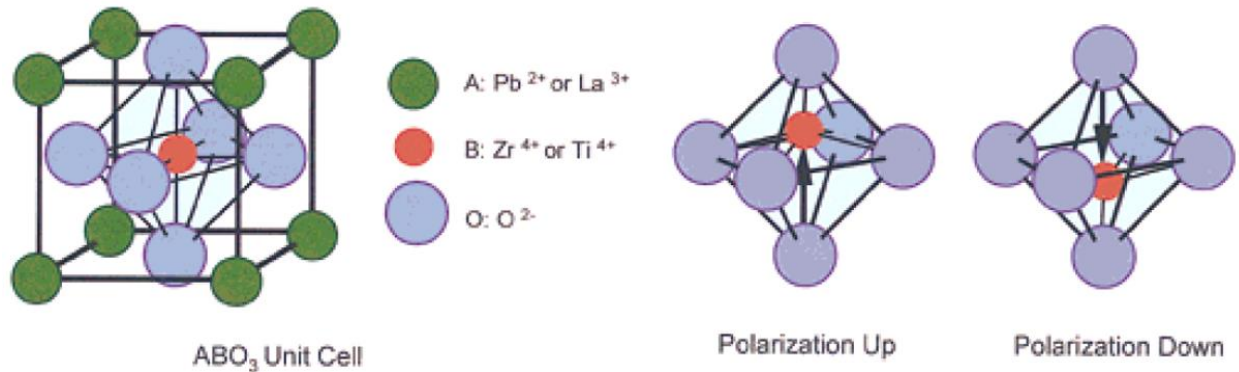
Figure 1.11 The unit cell structure of perovskite PZT or PLZT, illustrating two of six polarization states due to the movement of central cation (Reproduced from Ref. 28).[28]

1.2.3 Multiferroism

Multiferroism indicates a physical property when the material possesses two or more so-called "ferroic" orders simultaneously, which includes ferromagnetism, ferroelectricity and ferroelasticity. Ferromagnets and ferroelectrics, as mentioned above, indicate the materials that have the spontaneous magnetization/electric polarization that can be reversed by an external magnetic/electric field. Ferroelasticity refers to the property when materials have spontaneous strain that is revisable by stress. The fourth ferroic order called ferrotoroidicity, indicating the spontaneous ordering of the magnetic vortices in the materials, has been recently observed.[29] Figure 1.12 shows the correlation between different physical parameters in traditional ferroic orders and the comparison of all four ferroic orders under the parity operations of space and time.[29,30] In practice, the concept of multiferroism has been expanded which includes the non-primary ferroic orders (antiferromagnetism, ferrimagnetism, etc.).
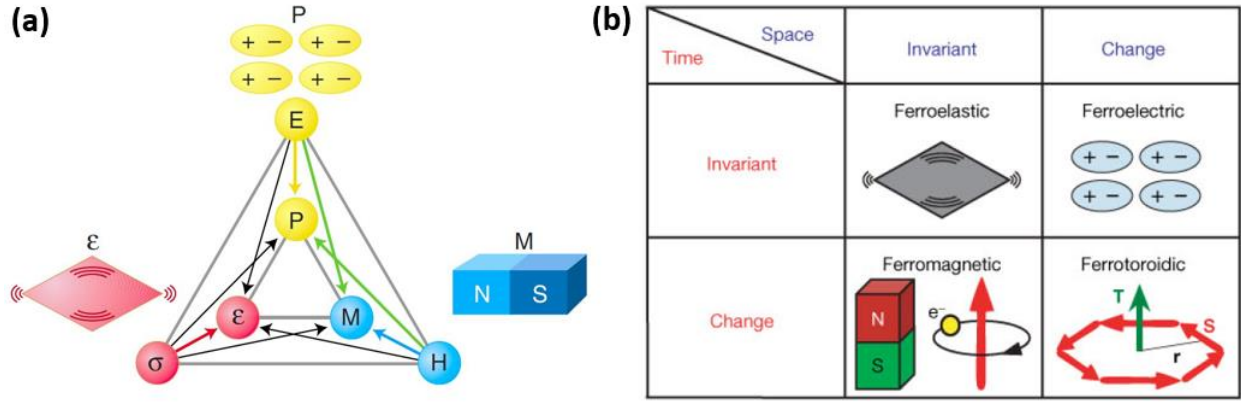
Figure 1.12 (a) Phase control in ferroic and multiferroics.[30] (b) Comparison of four ferroic orders under the parity operations of space and time.[29]

Among the multiferroic materials, the co-existing of ferromagnetism and ferroelectricity, which is called magnetoelectric multiferroism, has attracted extensive research interests due to the tunability of magnetic response to electric field and vice versa. Hereafter, the multiferroism will specifically refer to the magnetoelectric multiferroism. Figure 1.13 shows the relationship between the ferromagnets, ferroelectrics, multiferroics and magnetoelectrics, which have the coupling of the magnetic and electric properties. In device applications, multiferroic materials can be utilized to decrease the energy usage by switching magnetic states via electric field, instead of magnetic field.[31] However, the ferromagnetism and ferroelectricity are usually exclude each other: ferromagnetism requires partially filled d-orbitals while ferroelectricity requires non-symmetric structure with empty d-orbitals. These mechanisms lead to the rare amount of single-phase multiferroics found in nature or synthesized products. The single-phase multiferroic materials can be categorized into two groups.[32] For type-I multiferroics, the coupling between the magnetic and ferroelectric is weak, in which the magnetism and ferroelectricity have independent origins. Type-I multiferroics can be furtherly classified into four sub-groups according to the origin of the ferroelectricity: multiferroic perovskite, ferroelectricity due to lone pairs, ferroelectricity due to charge ordering and "geometric" ferroelectricity. In perovskite, the materials usually have the above mentioned "d^0 vs d^n problem". The multiferroism might be achieved by synthesizing perovskite structures with mixed d^0 and d^n ions. In $BiFeO_3$, $BiMnO_3$ and $PbVO_3$, the Bi^{3+} and Pb^{2+} cations have two electrons not forming chemical bonds, but the lone pairs or dangling bonds instead, which causes the ferroelectricity. In $LuFe_2O_4$ and Ca_3CoMnO_6, ferroelectricity is originated from the inequivalent sites and bonds after charge ordering. In hexagonal $YMnO_3$, the

ferroelectricity is caused by the geometrically tilted practically rigid MnO_5 block. On the other hand, the ferromagnetism and ferroelectricity are strongly coupled in type-II multiferroics, in which the ferroelectricity is in conjunction with a spiraling magnetic phase.
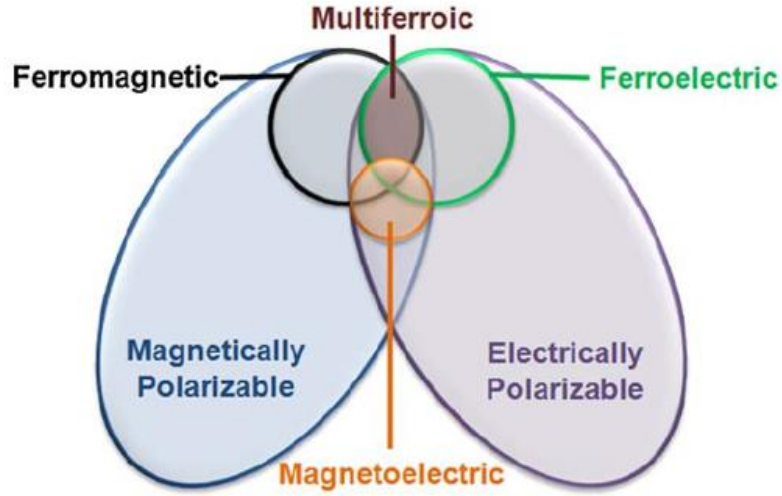
Figure 1.13 Illustration of the relationship between ferromagnetic, ferroelectric and magnetoelectric multiferroic materials.[19]

1.2.4 Magnetoresistance

1.2.4.1 Fundamental of magnetoresistance

Magnetoresistance (MR) refers to the phenomenon that, while an external magnetic field is applied, the electric resistivity of the material is changed. The value of the MR can be expressed by the following equation:

$$MR = \frac{R_H - R_0}{R_0} \times 100\% \tag{1.3}$$

While R_H and R_0 refer to the electric resistance measured with and without the external magnetic field. The MR effect was firstly discovered by William Thomson in 1856,[33] and ever since then, more sub-groups of MR effects have been studied in detail, including giant magnetoresistance (GMR), tunneling magnetoresistance (TMR), anisotropic magnetoresistance (AMR), colossal magnetoresistance (CMR) and low-field magnetoresistance (LFMR).

1.2.4.2 Categories of magnetoresistance

The GMR effect is observed in the thin films with alternating ferromagnetic and non-magnetic metal multilayered structures. In the neighboring ferromagnetic metal layers, the spins can have either parallel or antiparallel alignment due to the local magnetization states. The parallel spin alignment generates low resistance while the antiparallel alignment generates high resistance. The GMR can be calculated by the following equation:

$$GMR = \frac{R_{\uparrow\downarrow} - R_{\uparrow\uparrow}}{R_{\uparrow\uparrow}} \times 100\% \tag{1.4}$$

While $R_{\uparrow\downarrow}$ and $R_{\uparrow\uparrow}$ indicate the resistance of antiparallel magnetization and parallel magnetization, respectively. The GMR effect was first reported by Albert Fert in 1988 with the study of an Fr/Cr multilayered structure.[34] Interestingly, Peter Grünberg also discovered the similar phenomenon in the Fe/Cr/Fe trilayered structure almost at the same time.[35] Both of them were awarded the Nobel Prize in Physics in 2007 for the discovery of GMR effect. Figure 1.14 shows the GMR result reported by Albert Fert in 1988.[34]
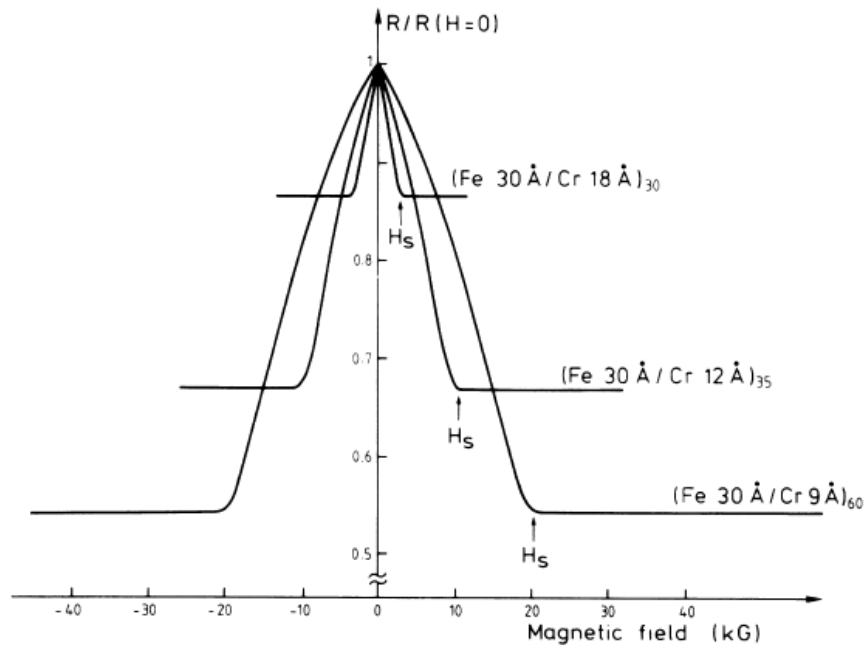
Figure 1.14 GMR effect of the Fe/Cr superlattices at 4.2 K. Reported by Albert Fert in 1988.[34]

TMR is also observed in the multilayered thin film, but with the alternating alignment of ferromagnetic layers and ultra-thin insulating layers. Such structure is called magnetic tunneling

junction (MTJ), in which the electrons can tunnel through the thin insulating barrier under an applied bias voltage. The external magnetic field can change the spin alignment (parallel and antiparallel) in adjacent ferromagnetic layers, which affects the tunneling current and the overall resistance of the structure. The TMR can be calculated by the following equation, while the terms R_{ap} and R_p represent the resistance measured at the antiparallel and parallel states, respectively.

$$TMR = \frac{R_{ap} - R_p}{R_p} \times 100\% \tag{1.5}$$

CMR is a property that is strongly related to the ferromagnetic to paramagnetic (PM) phase transition. Large MR effect is observed at a temperature close to the phase transition temperature of the perovskite ferromagnetic materials. The CMR effect is a result of the interplay among the spin, charge, orbital and lattice degrees of freedoms. In doped $LaMnO_3$ (LSMO, LCMO etc.), the CMR occurs at the Curie temperature (T_c) and metal-to-insulator transition temperature (T_{MI}) of the material, which is associated with DE model. The hopping of the e_g electrons along the Mn^{3+}-O-Mn^{4+} interactions is affected by the spin angle between the adjacent Mn cations (more hoping at lower angle). The external magnetic field can change the alignment of the Mn-spins, which subsequently change the conductivity of the material. Figure 1.15 shows the schematic illustration of the DE in CMR materials.[36]
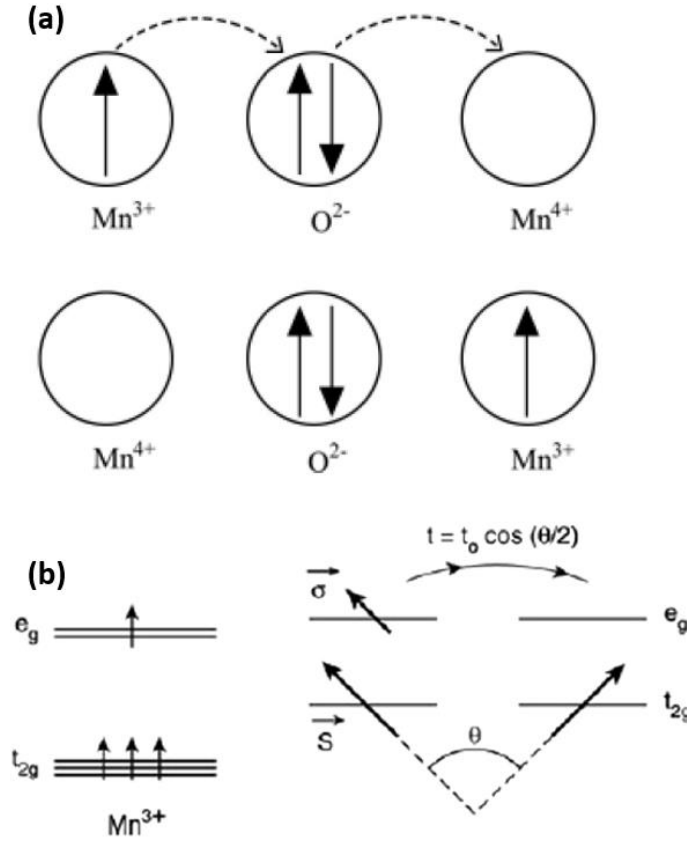
Figure 1.15 (a) Schematic representation of the double exchange mechanism proposed by Zener. (b) Sketch of de Gennes spin-canted states.[36]

In the above mentioned MR effects, large external magnetic field of several tesla is required, which hinders their potential applications. LFMR is a MR property that exhibits at the magnetic field lower than one tesla. LFMR arises from the CMR materials by introducing in structural disorders like grain boundaries or phase boundaries. The spin-polarized tunneling through such electronic barriers is responsible for the LFMR. Similar to the general equation of MR, LFMR is given by:

$$LFMR = \frac{R_H - R_0}{R_0} \times 100\% \qquad (1.6)$$

1.2.5 Transmittance

When a light beam shots at a transparent material, part of the light can transmit through the material while the other part is absorbed or reflected. Transmittance indicates the proportion of the

radiant energy passes through the material versus the total incident beam energy. From the ultraviolet to infrared region, the material usually exhibits different abilities of absorbing or transmitting the light. The transmittance spectrum represents the transmittance of the material as a function of the wavelength of incident beam. In semiconductor, the light absorption is strongly related to the electronic structure of the material: photons with energy higher than the band gap can be absorbed to excite the electrons from the valence band to conduction band. As a result, the transmittance spectra include the information of the band gaps of the materials. The theoretical foundation of characterizing the optical band gap using the transmittance was reported by Jan Tauc in 1968.[37] The band gap of the material can be derived from a $(\alpha h\upsilon)^{1/r}$ vs $h\upsilon$ plot, where α and r indicate the absorption coefficient of the material and the nature of the transition, respectively. The abscissa and ordinate values can be calculated from the wavelength of the incident beam and the corresponding transmittance of the material. The plot was named as "Tauc plot" in recognition of his contribution. Figure 1.16 shows the Tauc plot and the transmittance spectrum of the ZnO:B films.[38]
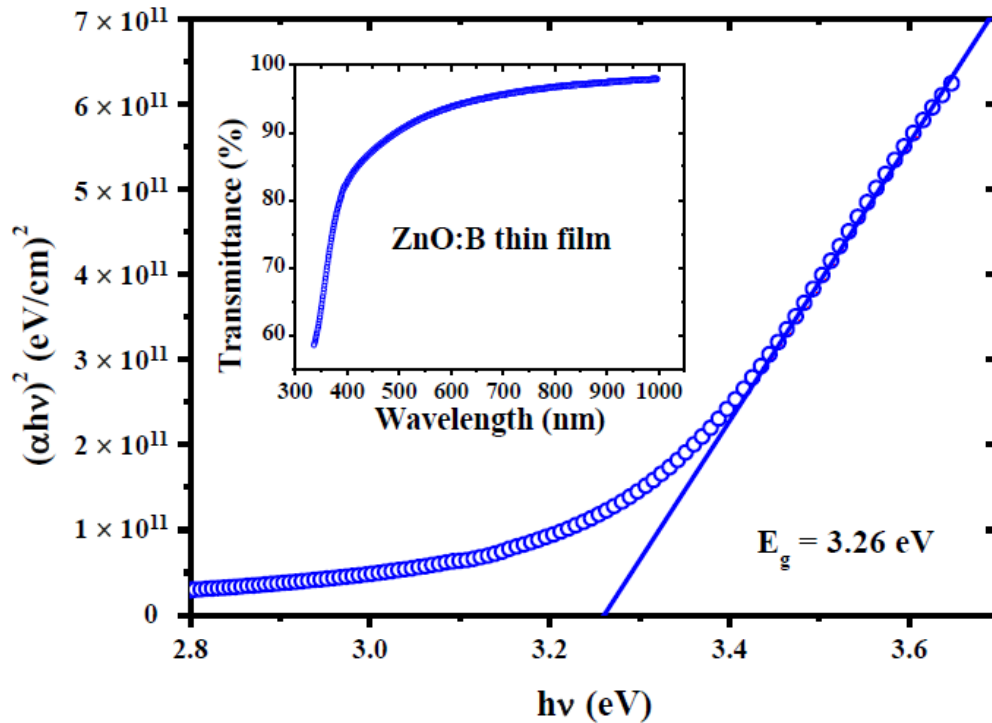
Figure 1.16 Tauc plot of boron-doped ZnO films with the inset showing the corresponding transmittance spectrum.[38]

1.3 Strain engineering in oxide thin films

Strain engineering refers to a strategy of tuning or enhancing the performance of the materials by manipulating the strain within the materials. In oxide thin films, the physical properties including ferroelectricity, ferromagnetism, multiferroism, superconductivity and magnetoresistance are strongly associated with the strain state of the films, which can be enhanced by strain engineering. Strain occurs as a result of the lattice matching between the adjacent lattices with different lattice parameters. In thin films, strain can be classified into three categories according to its origin: substrate induced strain, multilayer induced strain and vertically aligned nanocomposite (VAN) induced strain. Introduction of each strain category and its impact on the properties of functional oxides will be given below.

1.3.1 Substrate induced strain

When the lattice parameter of the thin film is different from that of the substrate, stress will be generated to force the in-plane lattice parameter of the film to match with the substrate. As a result, strain will be generated in the film, and it is called the substrate induced strain. Substrate induced strain is usually caused by a relaxed heteroepitaxial film growth mechanism with a lattice mismatch lower than 7%. However, substrate induced strain also occurs at some special cases when the lattice mismatch is larger than 7%. One phenomenon is called domain matching epitaxy (DME), which was proposed by Narayan in 2003.[39] In DME, instead of the 1 to 1 matching between the film and substrate lattices, a domain matching of m film planes with n substrate planes can largely decrease lattice mismatch, which prevents the instant strain relaxation at the substrate-film interface. In DME, the residual lattice mismatch f_r is given by:

$$f_r = \frac{ma_f - na_s}{na_f}; n = m + 1 \tag{1.7}$$

Where m and n are integral numbers and a_f and a_s indicate the lattice parameters of the film and substrate, respectively. For instance, in the TiN on Si (001) system, the substrate induced strain is decreased from 24.6% to 4.4% by the DME growth with 3/4 matching.[39] Beside of the DME, the substrate induced strain can also be maintained below 7% by the rotation of the film lattices. One typical example is the growth of CeO_2 on $SrTiO_3$ (STO) (001) substrate. CeO_2 has a cubic structure with a lattice parameter of 5.41 Å, while the lattice parameter of the cubic STO is only 3.91 Å. Instead of the cube-on-cube growth with a large lattice mismatch, the CeO_2 lattice has a 45°

rotation along the substrate surface, which results in the matching between half CeO_2 diagonal to the STO edge. The strain can be reduced from -38.3% to 2.0%. The XRD phi scan can be used to demonstrate the rotation of CeO_2 lattices.[40]

Substrate induced strain provides an easy approach for strain engineering: the degree of the strain can be simply tuned by the material selections. Figure 1.17 shows the lattice parameters of some commonly studied film and substrate materials with the pseudotetragonal or pseudocubic structures.[41] The commercialization of these substrates can provide high epitaxy quality of the thin films and decrease the cost of the fabrications. However, the biggest constraint of the substrate induced strain is the strain relaxation above the critical thickness, which usually reduces with the increasing lattice mismatch. This relaxation phenomenon limits the application of substrate induced strain engineering in thick films.
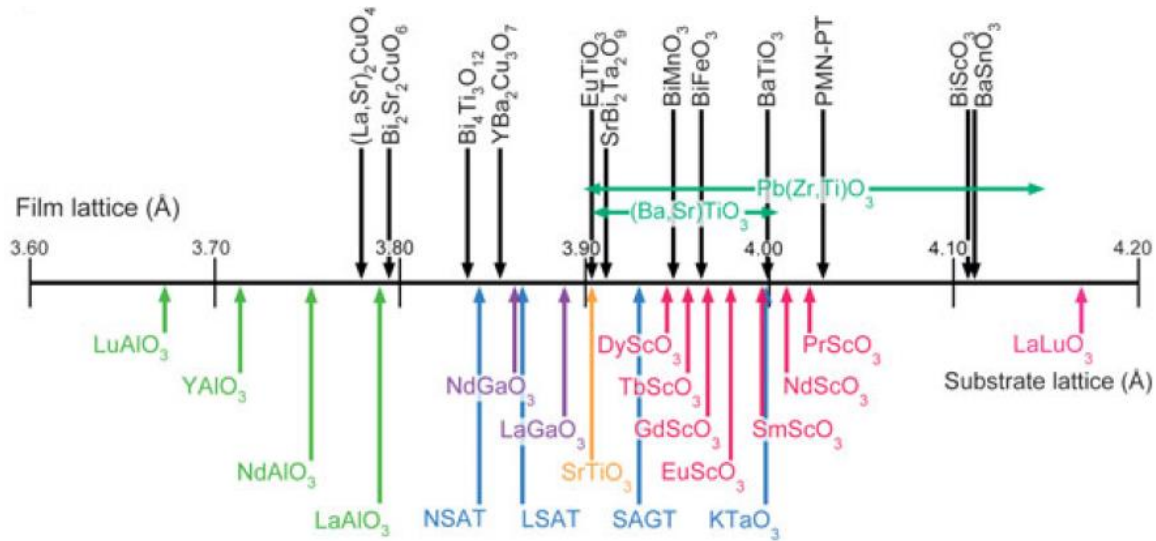
Figure 1.17 The a-axis lattice parameters of some common pseudotetragonal or pseudocubic materials for film or substrate applications.[41]

1.3.2   Multilayer induced strain

Multilayer structured thin films, or superlattice, can be obtained by alternatively growing different layers of materials. Figure 1.18 (a) shows a schematic drawing of a multilayered nanocomposite.[42] Similar to the substrate induced strain, multilayer induced strain can be generated as a result of the lattice mismatch between different layers, which is also a biaxial strain in the *ab* plane. In multilayered thin film, strain can still generates from the lattice mismatch

40

between the film and substrate. However, the multilayer induced strain becomes dominating since each lamellar layer can serve as the source of the multilayer induced strain. In other words, for the adjacent two layers, the bottom layer acts like the substrate of the upper layer. Domain matching and the rotation of the lattices can also be found in superlattices to decrease the lattice mismatch. Figure 1.18 (b) shows the strain maps of a $LaMnO_3$:$SrMnO_3$ superlattice along c-axis (upper section) and b-axis (lower section), respectively.[43] Clear alternating negative contrast can be observed in ε_{cc}, which is originated from the lattice mismatch between the $LaMnO_3$ and $SrMnO_3$. The uniform and nearly zero strain in ε_{bb} indicate the high epitaxial growth quality of the superlattice. Comparing with substrate induced strain, which only has one strain source, multilayer induced strain is sustainable at thicker regions. For a perfectly grown superlattice, the strain can be maintained all the way through the film thickness theoretically. However, in practice, the multilayer induced strain can still be relaxed as a result of the decreasing surface quality of the layers as the film continues to grow. Besides, in multilayer structure, due to the combination of different materials, properties of different phases might also be combined. As a result, some properties which are difficult to obtained for a single phase system (i.e. multiferroism) can be obtained and tuned in such structure.
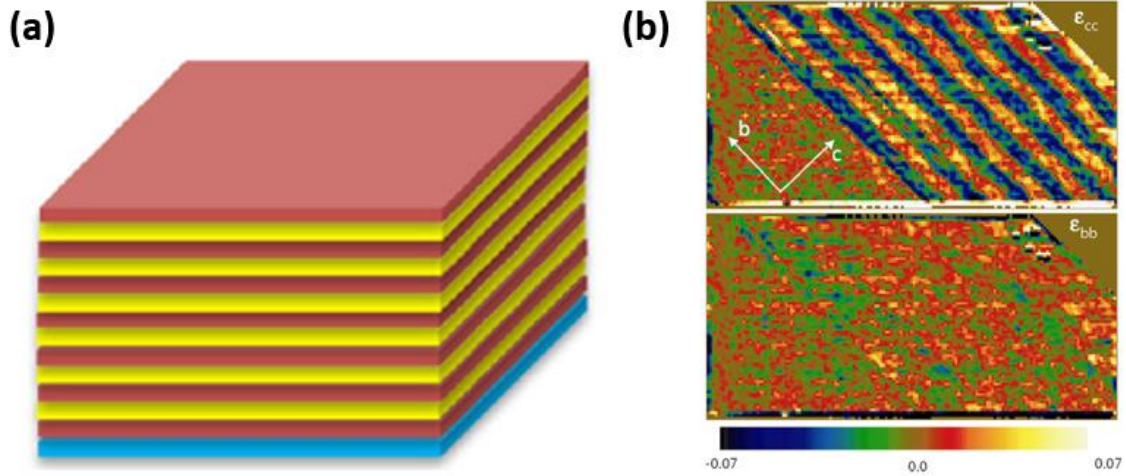
Figure 1.18 (a) Schematic illustration of a lamellar multilayered thin film.[42] (b) Calculated strain maps of a $LaMnO_3$:$SrMnO_3$ superlattice.[43]

1.3.3 Vertically aligned nanocomposite induced strain

1.3.3.1 Overview of vertically aligned nanocomposite thin films

Nanocomposite thin films that are consist of two of more materials have attracted extensive research interests owing to the interplay between structural, electronic and magnetic degrees of freedom and the combination of the unique functionality of each material. In nanocomposite thin films, different materials are grown separately on the same substrate, which forms two phases. According to the microstructure of the phases, nanocomposite thin films can be categorized into three groups: nanoparticle in matrix structure, multilayered structure and VAN structure. VAN thin films have a 2-2 type architecture with either nanocheckerboard or nanopillars in matrix structure. Figure 1.19 shows the plan-view TEM and STEM images of the VAN thin films with these two structures.[44,45] Benefitting from their simple self-assembled growth, vertically aligned structure and resulting heterointerface, strong strain tunability and coupling effect, VAN thin films have been widely investigated in the last two decades.
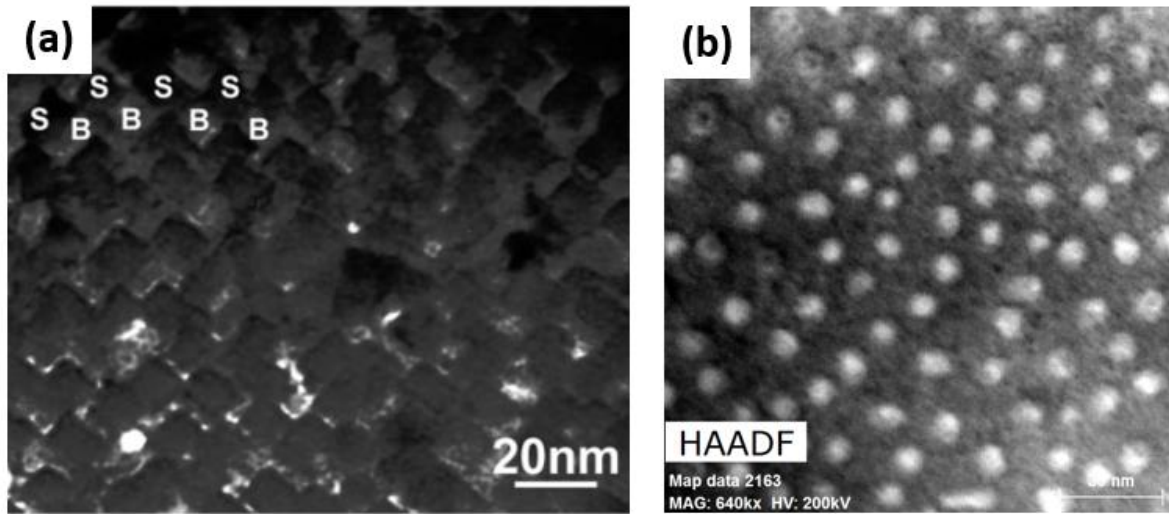
Figure 1.19 (a) Plan-view TEM image of $(BiFeO_3)_{0.5}$:$(Sm_2O_3)_{0.5}$ (BFO:SmO)VAN thin film with checkerboard structure (Reproduced from Ref. 44).[44] (b) Plan-view STEM image of $(La_{0.7}Ca_{0.3}MnO_3)_{0.8}$:$(CeO_2)_{0.2}$ VAN thin film with pillar in matrix structure.[45]

In 2002, the VAN structure was first introduced in LCMO:MgO thin films prepared by a solution based technique.[46] The strain has been changed through the phase transition in the films with varies MgO concentration (from 0 to 80%), leading to the drastic change in the resistivity and

magnetotransport properties. Later in 2004, a $BaTiO_3$:$CoFe_2O_4$ (BTO:CFO) with magnetostrictive CFO pillars embedded in electrostrictive BTO matrix.[47] The ME coupling is demonstrated in the system, which is generated from the strong elastic interactions between the two phases. The strain tuning effect of the VAN thin films was first demonstrated in the BFO:SmO and LSMO:ZnO nanocomposites.[48] After that, extensive effort has been spent and many new VAN systems have been studied. Table 1.3 summarizes some demonstrated VAN systems and their functionalities.

Table 1.3 Summary of representative VAN thin film systems with functionalities

Functionality	VAN system	Crystal structure
Ferroelectricity	BTO:SmO	Perovskite–Rock salt
	BTO:CeO$_2$	Perovskite-Fluorite
	BFO:SmO	Perovskite–Rock salt
Magnetism and magnetotransport	LSMO:ZnO	Perovskite-Wurtzite
	LSMO: CeO$_2$	Perovskite-Fluorite
	LSMO:Mn$_3$O$_4$	Perovskite-Spinel
	LSMO:NiO	Perovskite-Rock salt
	LCMO:MgO	Perovskite-Rock salt
	LCMO: CeO$_2$	Perovskite-Fluorite
Multiferroism	BFO:CFO	Perovskite-Spinel
	BTO:CFO	Perovskite-Spinel
	BTO:YMO	Perovskite- Perovskite
	BTO:LSMO	Perovskite- Perovskite
	BFO:NiFe$_2$O$_4$	Perovskite-Spinel
Dielectric and optical properties	BFO:SmO	Perovskite-Rock salt
	SrRuO$_3$:SmO	Perovskite-Rock salt
	SrRuO$_3$:ZnO	Perovskite-Wurtzite
Exchange bias	LSMO:BFO	Perovskite- Perovskite
	LSMO:LaFeO$_3$	Perovskite- Perovskite
	LSMO:NiO	Perovskite-Rock salt
Superconductivity	BaZrO$_3$:YBCO	Perovskite-Layered Perovskite
	BaSnO$_3$:YBCO	Perovskite-Layered Perovskite
	BaHfO$_3$:YBCO	Perovskite-Layered Perovskite

1.3.3.2 Growth and microstructure of VAN thin films

The fundamental understanding of the growth mechanism of the VAN thin films is necessary for the microstructure design and multifunctionality tuning. In this section, the fabrication of VAN

thin films by pulsed laser deposition (PLD) is taken for example. The growth process of a VAN thin film is shown in the schematic drawings in Figure 1.20, which can be divided into three steps: surface diffusion of the adatoms (clusters), nucleation and islands growth and finally the columnar thin film growth.[42] During the target preparation, the materials of the two immiscible phases were mixed based on the desired atomic ratios. As the deposition starts, the adatoms of both species simultaneously arrive and diffuse at the substrate surface. Some of the atoms are trapped by the defects, and the others of the same species are gathered due to the same surface energy. The islands of different phases are formed as more adatoms diffuse together and the columns are grown from the islands. The pillar in matrix structure in some VAN systems can be explained by the different interfacial energies in the phases, while the adatoms with large interfacial energy tend to diffuse and form a planar matrix.

Adatoms diffusion
(a)

Nucleation and islands growth
(b)

Columnar growth
(c)

Two - phase VAN model
(d)
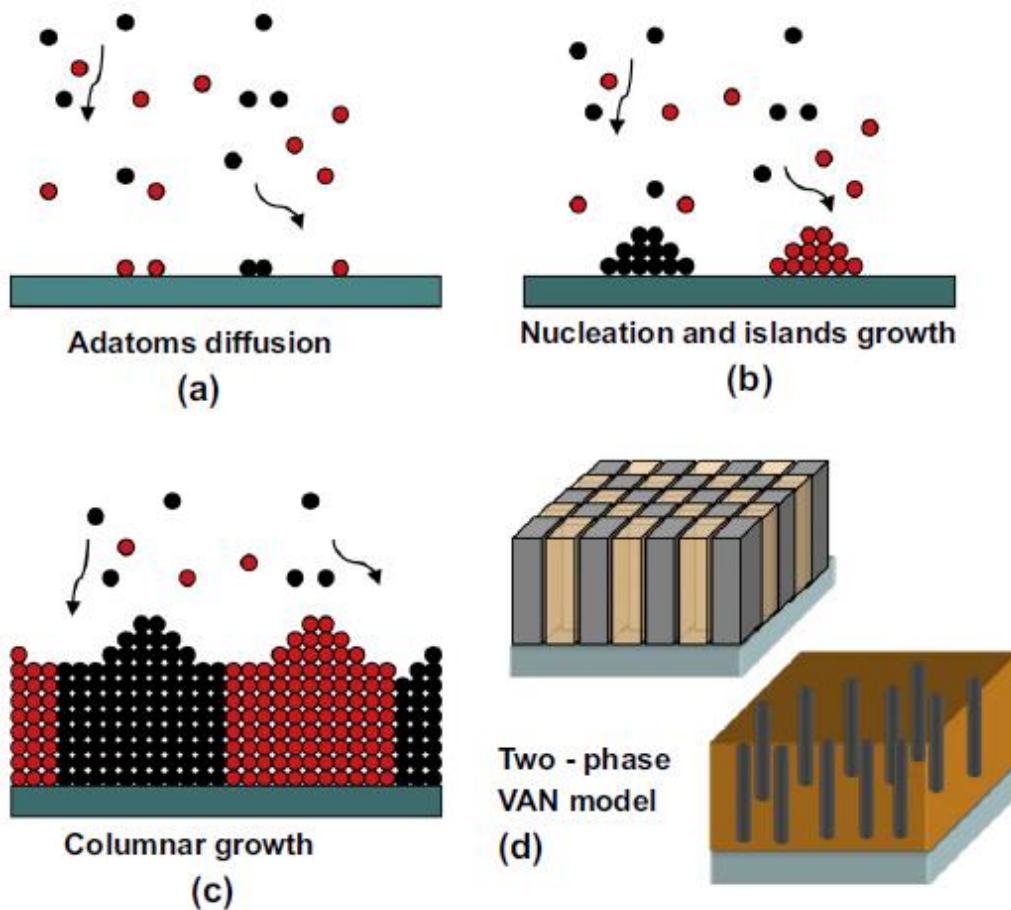
Figure 1.20 (a-c) Schematic drawings showing the growth mechanism of the VAN thin films. (d) Two VAN morphology models.

Over the past decades, it has been demonstrated that several aspects are responsible for the microstructure of the VAN thin films. The substrate selection of varies structures, lattice parameters and orientations; the materials selection of varies composition ratios and lattice matching relationships; the deposition conditions of varies substrate temperatures, oxygen pressures, deposition frequencies and laser energies are all effective factors for the microstructure tuning. H. Zheng et al. have demonstrated the microstructure tuning through the substrate orientation in a BFO:CFO VAN system.[49] In this work, the BFO:CFO thin films were grown on (001) (111) and (110) oriented STO substrates using the pulsed laser deposition. The perovskite BFO has the lowest surface energy of {001} planes while the spinel CFO has the lowest surface energy of {111} planes. When growing on the (001) STO, a rectangular CFO pillar in BFO matrix structure is obtained as the BFO is completely wetting the substrate with layer-by-layer growth and CFO has the island growth (Figure 1.21 (a-b)). On the other hand, a triangular BFO pillar in CFO matrix structure can be observed on (111) STO since the CFO follows a layer-by-layer growth (Figure 1.21 (c-d)). On the (110) oriented substrate, since both phases have comparable surface energy, a maze pillar-pillar structure is formed (Figure 1.21 (e-f)). The plan-view TEM images have illustrated the different microstructure of the thin films.
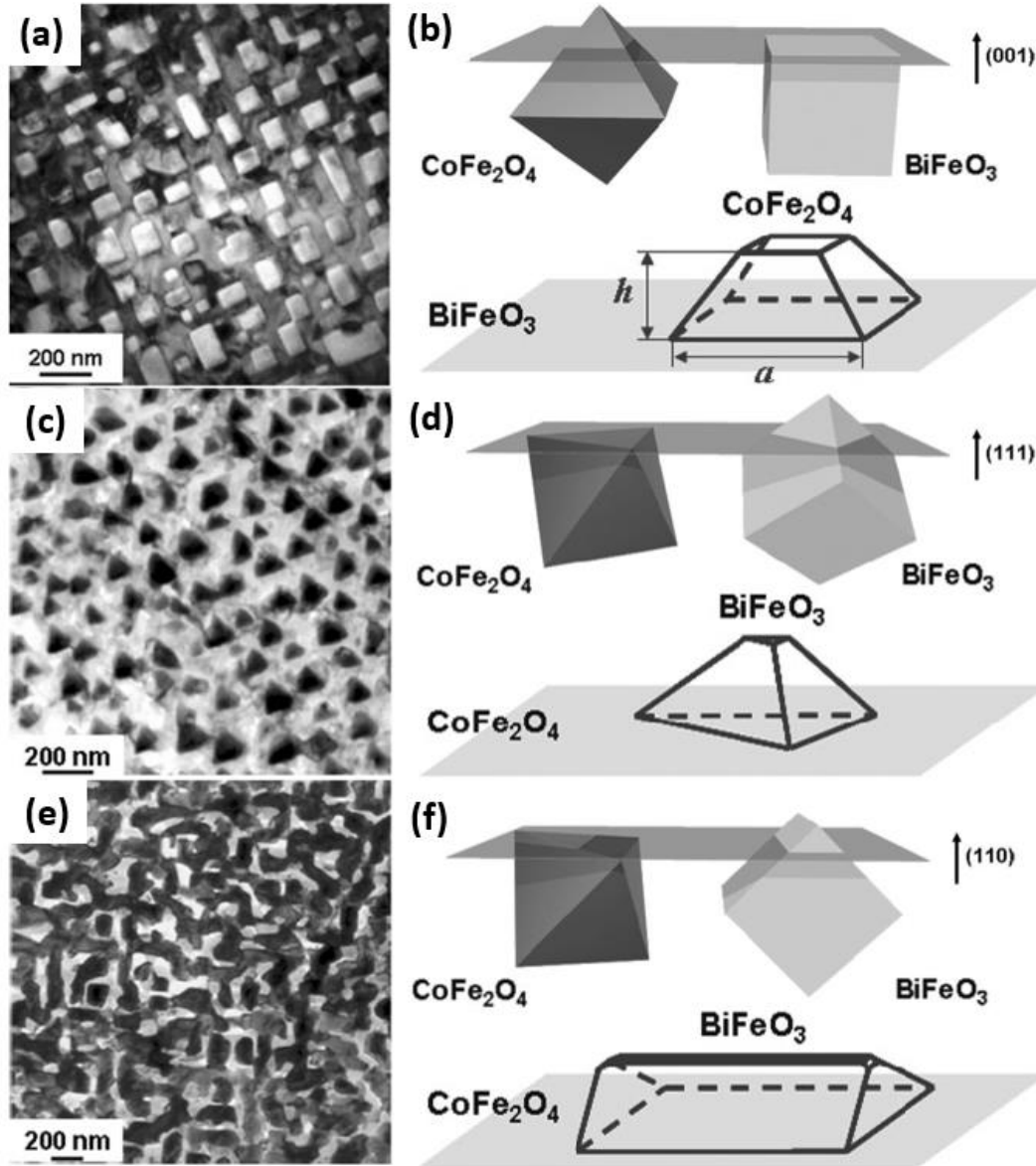
Figure 1.21 The plan view images and the schematic illustration of the nucleation and island growth of the BFO:CFO VAN thin films grown on (a-b) (001), (c-d) (111) and (e-f) (110) orientated STO substrates (Reproduced from Ref. 49).[49]

1.3.3.3 Vertically aligned nanocomposite induced strain

Beside of the substrate induced strain, which can be found in all heteroepitaxial thin films, the VAN structure has brought a new category of strain called VAN induced strain. Such strain is originated from the lattice mismatch between two phases. Different from the biaxial substrate induced strain and multilayer induced strain, VAN induced strain provides an additional strain tuning orientation along the out-of-plane (OP) direction. Besides, the high density of the vertical

grain boundaries in VAN structures can maintain the strain through the film thickness up to several micrometers, while as a comparison, the substrate induced strain and multilayer induced strain can only be kept in very thin films (tens of nanometers for substrate induced strain and less than one micrometer for multilayer induced strain). Figure 1.22 shows the comparison of the substrate induced strain at ultra thin regions and the VAN induced strain throughout the film.[50]
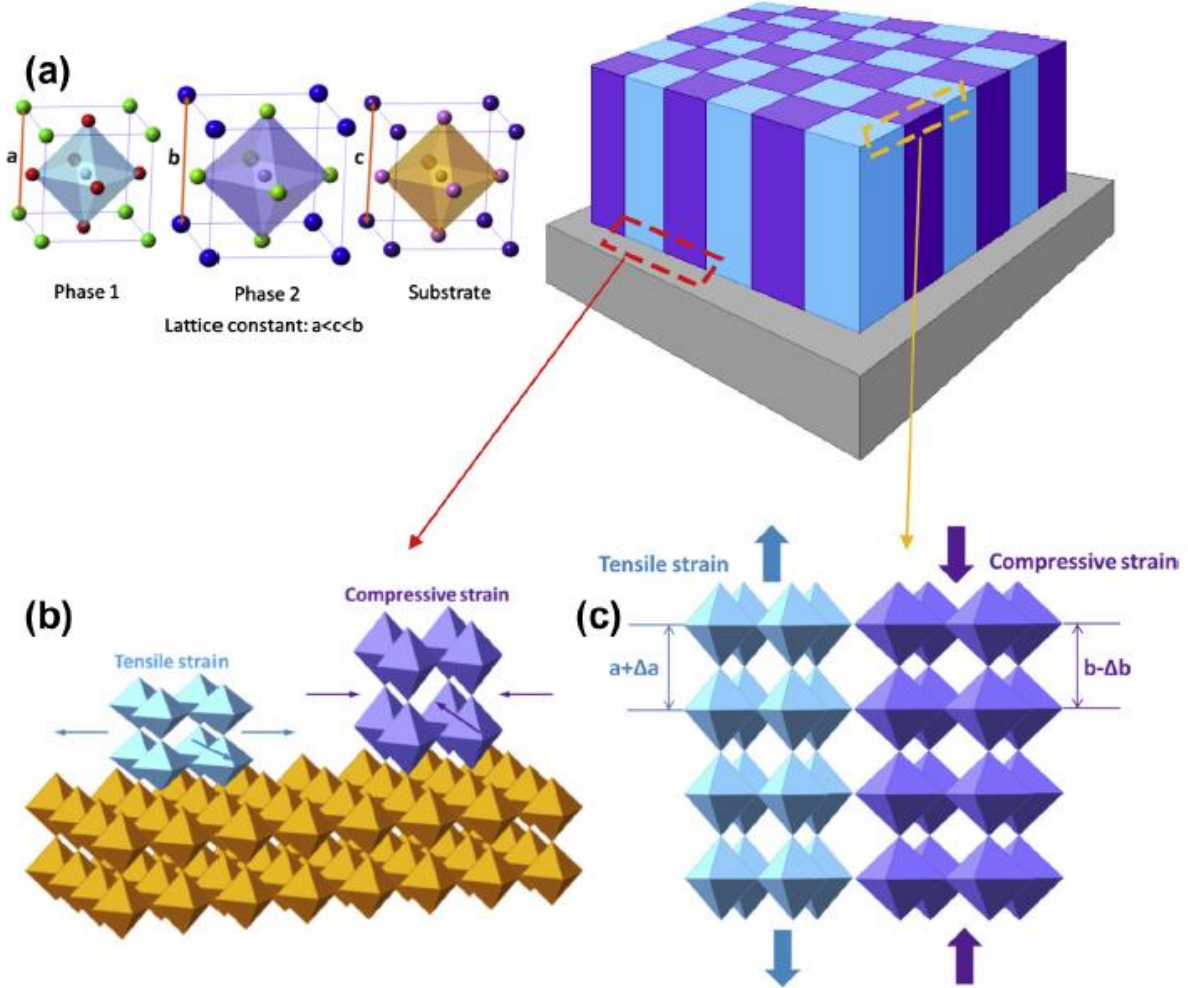
Figure 1.22 Schematic drawings of: (a) The unit cells showing the lattice parameters of the phases and substrate. (b) Substrate induced strain and (c) VAN induced strain.[50]

Vertical domain matching can be found in VAN thin films to decrease the lattice mismatch between the phase materials. Figure 1.23 (a) shows the lattice parameters of the phases and substrate in a LCMO:CeO$_2$ VAN thin films (CeO$_2$ has a 45° rotation to decrease the in-plane lattice mismatch).[45] The LCMO (L) and CeO$_2$ (C) lattices can have the 3L:2C or 4L:3C domain matching

relationships, which generates the opposites strain states in the neighboring domains (Figure 1.23 (b)). The cross-sectional STEM image and corresponding fast-Fourier transform (FFT) filtered image has confirmed the perfect alternating arrangement of the 3L:2C and 4L:3C domains (Figure 1. 23 (c)).
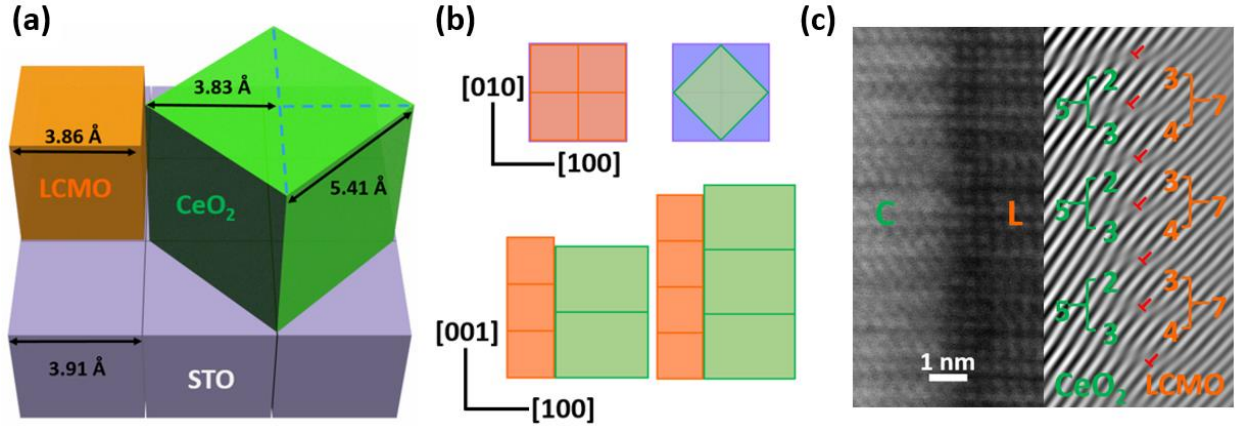
Figure 1.23 Schematic illustration of: (a) The bulk lattice parameters for LCMO, CeO_2 and STO. (b) The in-plane (top) and out-of-plane (bottom) lattice matching relationships among the phases and substrate. (c) Cross-sectional STEM image and corresponding fast-Fourier transform image of the LCMO:CeO_2 thin film (Reproduced from Ref. 45).[45]

As the VAN induced strain is strongly associated with the phase boundaries, strain tuning can be achieved by manipulating the shape, dimension and density of the pillars in the thin film. All the factors that have impact on the microstructure of VAN thin films might have the influence on the strain engineering, including the crystal structures, lattice parameters, orientations and atomic ratios of the selected phases and/or substrate; the deposition temperature, oxygen pressure laser frequency and laser energy. Taking the laser frequency as an example, the diffusion length of the adatoms can be calculated by:

$$L = 2\sqrt{Dt} \tag{1.8}$$

Where L, D and t indicate adatoms' diffusion length, diffusivity and diffusion time, respectively. Higher laser frequency can decrease the diffusion time of the adatoms, which leads to the smaller nucleation islands and thinner columns. The total area of the interfaces increases as the columns get thinner and therefore the VAN induced strain tuning effect is enhanced by an increasing

deposition frequency. Figure 1.24 shows column width and out-of-plane of the VAN thin films with respect to the deposition frequencies.[42] The columns have smaller dimensions and the vertical strain control is enhanced as the deposition frequency increases.
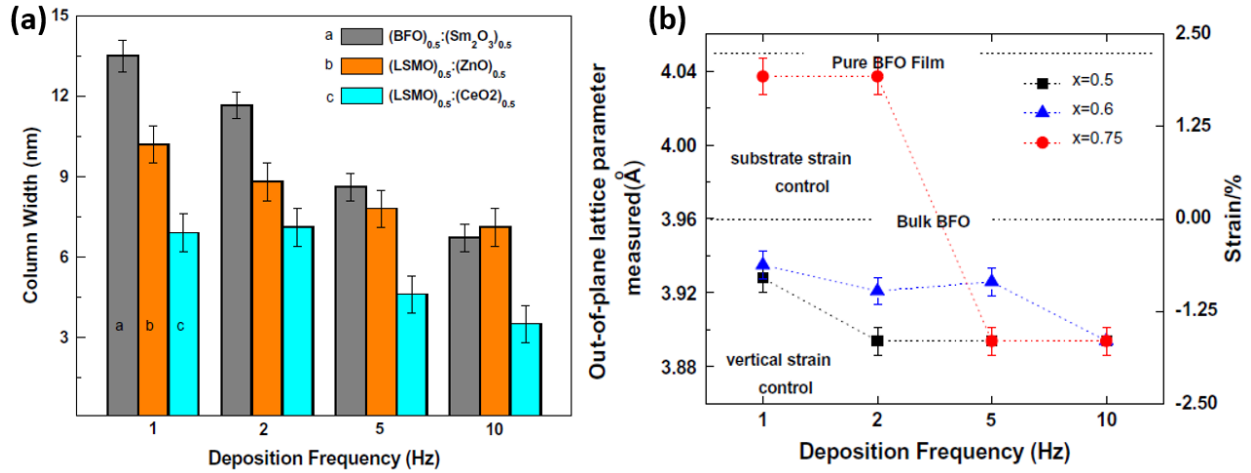
Figure 1.24 (a) Average column width of VAN thin films with different deposition frequencies. (b) Calculated out-of-plane lattice parameters and strain with different deposition frequencies in $(BFO)_x:(SmO)_{1-x}$ VAN thin films.[42]

1.3.4 Strain engineering in oxide thin films

Substrate induced strain, multilayer induced strain and VAN induced strain are all capable for the strain engineering. However, they also have their own limitations. Substrate induced strain is more effective in tuning the single phase thin films with the thickness no more than the critical thicknesses, which is usually few tens of nanometers. Multilayer induced strain can be utilized for tuning multiphase systems and the functionalities generated by the multiphase systems, such as multiferroism and LFMR. However, the multilayered thin films have the issues in maintaining the epitaxy quality and strain state in thick regions. VAN induced strain provides the tuning along the out-of-plane direction through the film thickness up to micrometers. But the formation of the VAN structure needs optimized growth conditions. In the next section, several examples will be given on the strain engineering of different functionalities in oxide thin films.

1.3.4.1 Strain engineering in ferromagnetic oxide thin films

The ferromagnetic property of the material is a result of the interplay among lattice, charge, spin and orbital degrees of freedom. Strain has a strong tuning effect on the transition temperature,

coercive field, magnetization, magnetic anisotropy and magnetotransport behaviors of the ferromagnetic thin films. Strain engineering has been applied on the perovskite structured rare earth manganese oxide thin films $RE_{1-x}A_xMnO_3$, where RE indicates the trivalent rare earth elements (La, Pr, Sm, Nd) and A indicates the divalent alkaline earth elements (Sr, Ca, Ba, Pb). In these materials, the ferromagnetic response is tunable as a result of the distorted or rotated oxygen octahedral under the strain. The ferromagnetic LSMO has been widely studied and shown tunable phase transition temperature and anisotropy under the strain.[51,52] Figure 1.25 (a) indicates the distortion of the MnO_6 octahedral under different strain states and the corresponding Jahn-Teller distortion.[53] In Adamo and his collaborators' work, the LSMO thin films were deposited onto different substrates ($LaAlO_3$, $LaSrGaO_4$, LSAT, STO, etc.) to obtain a biaxial strain range from - 2.3% to +3.2%.[54] Varies ratio between the vertical and horizontal lattice parameters and strains were obtain by the substrate selection (Figure 1.25 (b-c)). As a result, the Curie temperature as well as the electric resistivity of the LSMO thin films have been effectively tuned by the strain (Figure 1.25 (d-e)). The Curie temperatures of the LSMO thin films decrease as the tensile or compressive strain is applied. Besides, the resistivity of the films gradually increase as the strain goes up and the LSMO thin film grown on $LaAlO_3$ even becomes insulating. The anisotropic ferromagnetic response of a thin film is an intrinsic property originated from the crystal structure of the material.[55] However, the anisotropy can be created or tuned by the extrinsic approaches such as the shape, external stress/strain or interface exchange coupling.[56] In LSMO thin films, the anisotropy of the ferromagnetic response can be tuned by changing the strain states, due to the reorientation of the spin or magnetic easy axis/plane.[51]
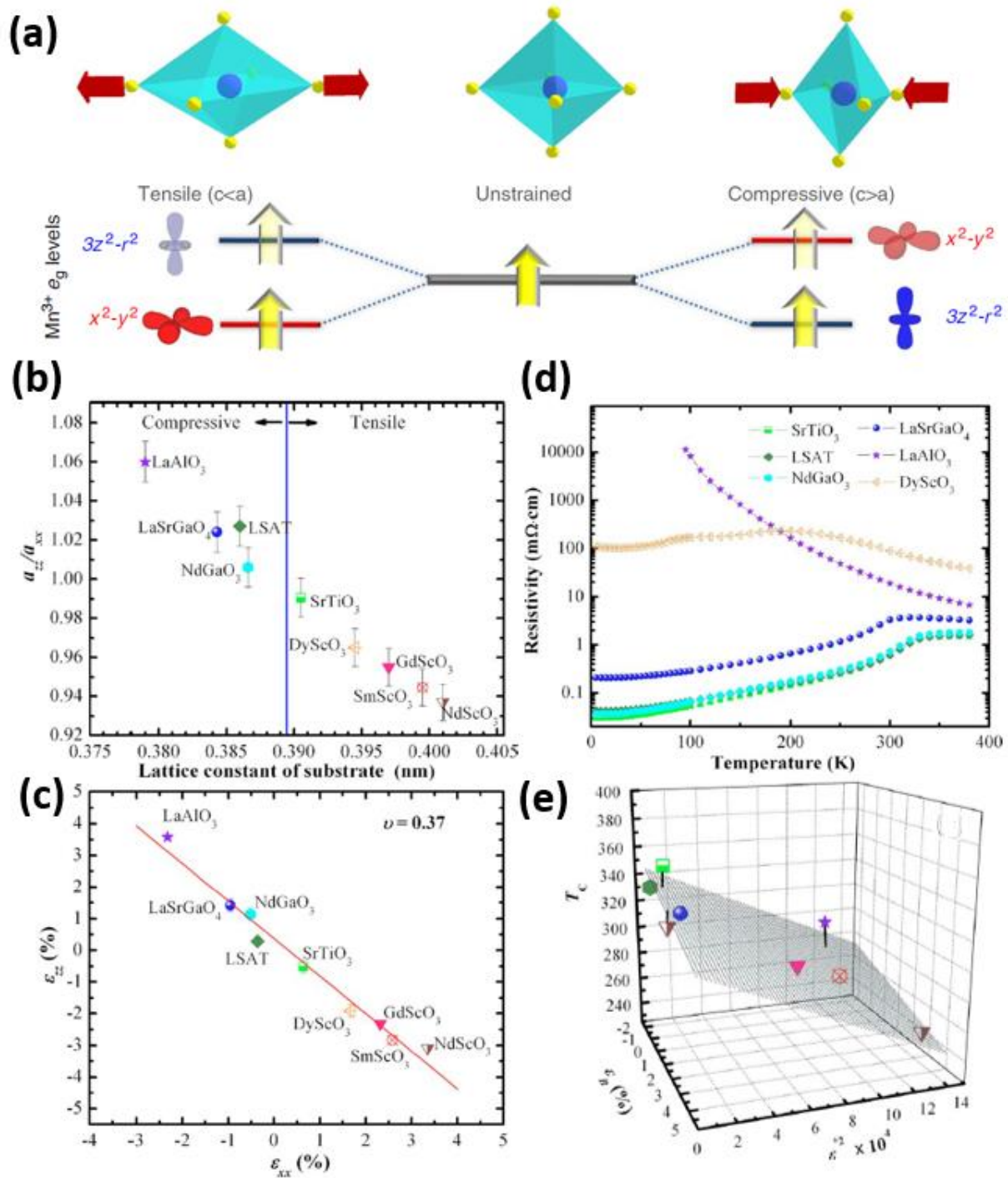
Figure 1.25 (a) Schematic illustration of the MnO_6 octahedral distortion as a function of the strain (top) and corresponding JT distortion on the e_g levels of Mn^{3+} ions.[53] (b) The ratio between the out-of-plane and in-plane lattice parameters of LSMO films as a function of substrate lattice spacings. (c) The out-of-plane strain as a function of in-plane strain. (d) The resistivity of LSMO thin films as a function of the temperature. (e) The Curie temperature as a function of the strain.[54]

1.3.4.2 Strain engineering in ferroelectric oxide thin films

Since the electric polarizations of the materials are strongly correlated to their strain states, the study of the strain engineering in oxide thin films have attracted extensive interests. The strain phase diagrams of many oxides have been establish by the theoretical calculations.[57,58] As mentioned, the ferroelectric response in the perovskite BTO thin films is originated from the displacement of the central cation, therefore the biaxial strain in the BTO lattices would have a large impact on their ferroelectricity. Figure 1.26 (a) shows the temperature-strain phase diagram of the (001) oriented BTO thin films.[59] From the phase diagram, it can be observed that the ferroelectric transition temperature T_c of the BTO thin films can be significantly tuned by the biaxial strain. In an unstrained BTO thin film, the T_c is around 120 ℃, while an in-plane strain of 2% is able to tune the Curie temperature to 800 ℃. Figure 1.26 (b) shows the temperature-strain phase diagram of the (001) STO thin films. Generally, STO is a dielectric material with no ferroelectric response. However, the room temperature ferroelectric response can be achieved in STO thin films as the strain is applied.[41] The experimental results have proved the theoretical hypothesis, as shown in Figure 1.26 (c) and (d).[18] In this work, the (001) BTO thin films were deposited onto the $DyScO_3$ and $GdScO_3$ substrates to obtained different level of compressive in-plane strain. It turns out the Curie temperature of the strained BTO thin film can have an increase of 500 ℃ and the remanent polarization can be enhanced for 250%. These experimental values are consistent with the calculation, as marked in Figure 1.26 (a). Apart from the Curie temperature, the strain engineering on the spontaneous polarization has been studied. Even though the tuning effect varies with the material systems, but the strong strain dependence can still be observed in BTO and PZT thin films.[60] The room temperature ferroelectric response of strained STO thin films has also been verified by experiments.[61,62]
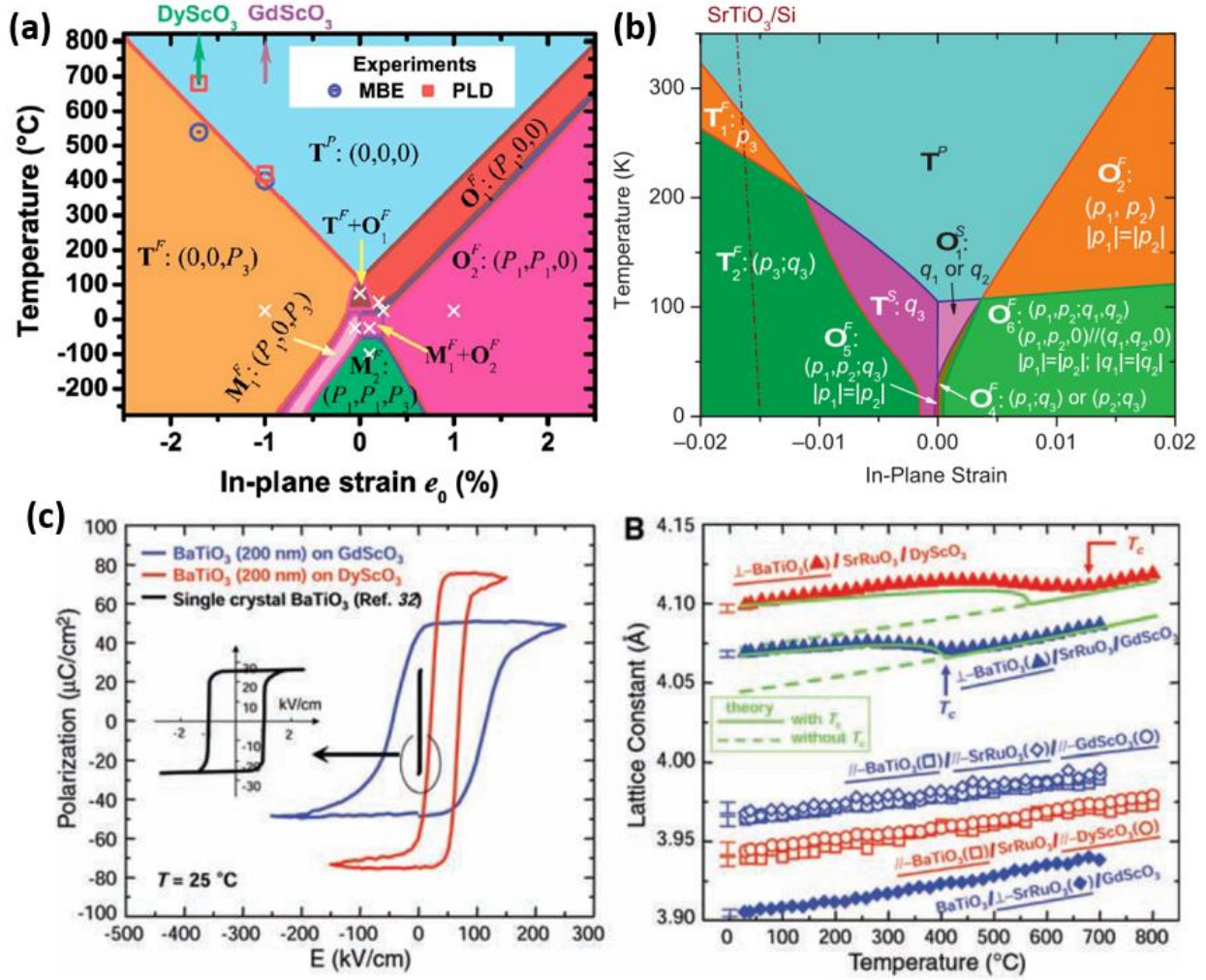
Figure 1.26 Temperature-strain phase diagrams of (001) orientated (a) BTO[59] and (b) STO[41] thin films. (c) Polarization-electric field hysteresis loops of BTO thin films. (d) Temperature dependence of lattice parameters of BTO thin films.[18]

1.3.4.3 Strain engineering in multiferroic oxide thin films

The study of multiferroics that exhibits the coexistence of ferromagnetism and ferroelectricity starts from the single phase materials. BFO is one of the widely studied single phase multiferroic material with antiferromagnetism and ferroelectricity.[63] The epitaxy BFO thin films were grown on STO (001) substrates to discover the strain effect on this multiferroic material.[12] Instead of the rhombohedral distorted perovskite structure in bulk state, the monoclinic structure was obtained. The compressive strain in generated in the BFO thin films, which was tuned by the film thickness from 50 to 500 nm. The constrained thin film has shown an enhanced spontaneous polarization of about one order of magnitude higher than the bulk and enhanced

thickness-dependent saturation magnetization. In addition to the single phase materials, the strain engineering has been studied in the two phase nanocomposite systems like the multilayered PZT:CFO and VAN structured BTO:CFO thin films.[47,64] In a BFO:CFO VAN system, the authors changed the deposition frequencies from 1 Hz to 10 Hz during the fabrication of the thin films.[65] The cone-like columns were obtained which formed the gradient interfaces. The magnetic anisotropy, coercive fields and ferroelectric switching behavior were tuned due to the strain accommodation and interface coupling. Figure 1.27 illustrated the microstructure, room temperature ferromagnetic and ferroelectric tuning results in this work.
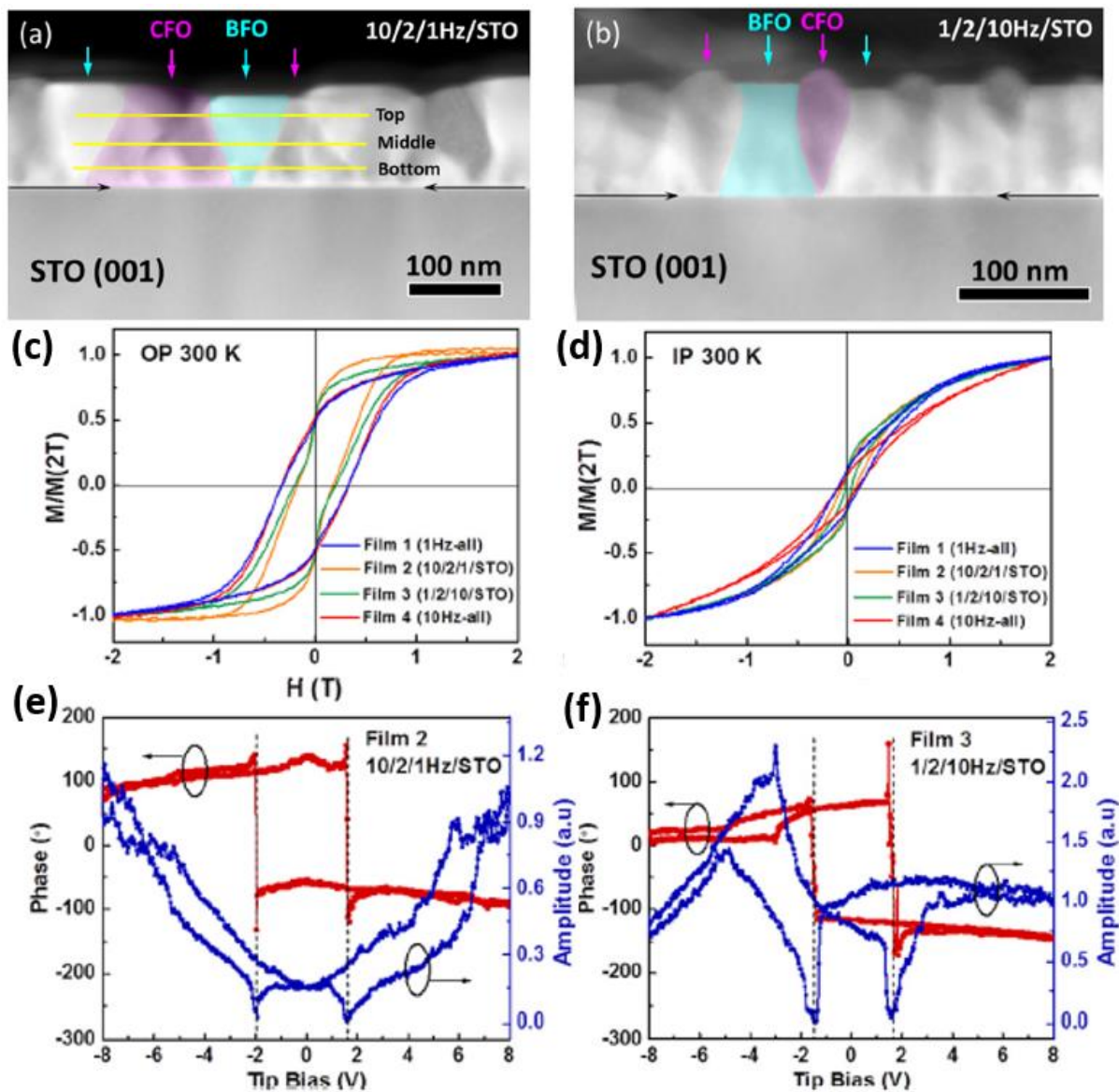
Figure 1.27 (a-b) The cross-sectional STEM images. (c-d) Room-temperature ferromagnetic hysteresis loops and (e-f) Room-temperature phase and amplitude switching curves of BFO:CFO VAN thin films with different deposition procedures.[65]

1.4   Research challenge and motivations

As discussed above, the multifunctionality tuning in oxide-based nanocomposite thin film is critical for many practical technology applications. VAN thin films have provided a novel tuning platform for enhanced or even new functionalities due to the unique structure and vertical strain engineering. By the material selection and growth condition control, many functionalities including electrical, magnetic, magnetotransport and multiferroic properties have been effectively tuned, as shown in Figure 1.28.[42] However, there are still many issues remain in this field. First, the discovery of new VAN systems still requires sustained efforts. Even though there have been so many new VAN systems demonstrated in the past decade, the total amount of the systems in this area is still limited. Besides, the formation of the VAN structure is a result of many factors from the material selection, phase composition to the deposition conditions including substrate temperature, oxygen pressure, laser energy, deposition frequency etc. All of the parameters have to be optimized before obtaining a novel epitaxial VAN thin film. This also restricts the discovery of the new systems. Second, the functionality study of the VAN thin films are still focused on the traditional physical properties like electricity and magnetism. Not much work has been done on the optical property tuning such as transmittance, band gap, dielectric constant etc., which could be used in optical devices.

With all the issues in mind, we have explored the functionality tuning of three new VAN system in this dissertation. Different tuning approaches, including the deposition frequency tuning and film composition tuning were utilized. Beside of the room temperature ferroelectricity, ferromagnetism and multiferroism properties that have been extensively reported in VAN thin films, tunable optical properties such as transmittance, band gap and dielectric constant have been studied. In addition to the study of the perovskite materials, we have also demonstrated the functionality tuning in the new discovered Aurivillius thin films with layered and compositional varied pillar-like domains embedded in matrix structure. The films have exhibited different properties as we change the transition metal element added into the system.
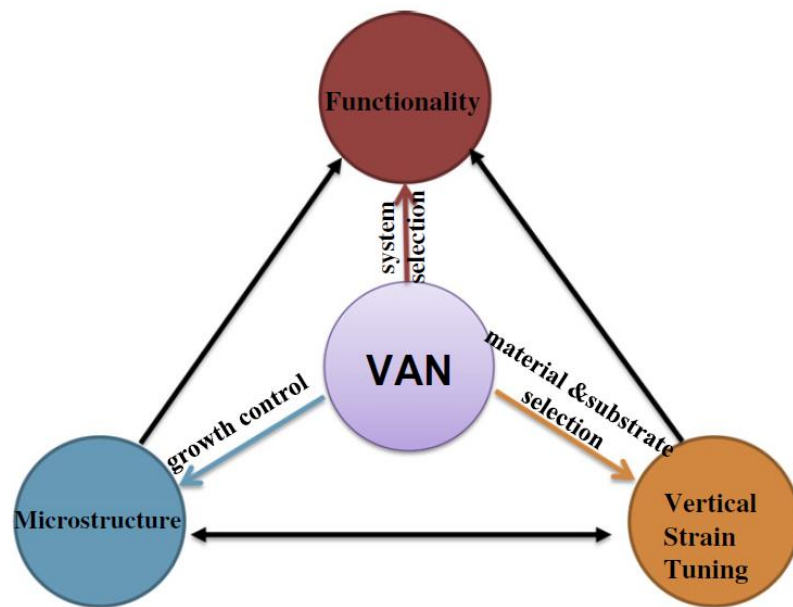
Figure 1.28 The illustration of the relationship among the microstructure, strain and functionality in VAN thin films.[42]

2. RESEARCH METHODOLOGY

2.1 Pulsed laser deposition

As briefly mentioned above, pulsed laser deposition (PLD) is a widely used physical vapor deposition (PVD) technique for high-quality thin film growth. Generally, the PLD system includes a laser source and high vacuum chamber. Figure 2.1 shows the schematic equipment set-up of a PLD chamber.[66] The PLD chamber consists of a rotatable target holder and a substrate holder with an attached heater, where the target to substrate distance is kept at 3-7 cm. Before the deposition, high vacuum of at least 1.0×10^6 mbar is required to reduce the impurities and decrease the scattering of the species in the plume. The deposition can be conducted in high vacuum or the atmosphere of high purity oxygen or nitrogen, based on the category of the thin films. During the deposition, the focused high-energy laser is hit on the surface of the rotating target in 45°. In the short pulse duration time (20-25 ns), the target undergoes a process of melting, evaporating and ionizing and a plasma plume with combined ions, atoms and molecules is formed. Thereafter, the species in the plume are transported and collected by the substrate and the thin films are fabricated on the substrate surface. The heated substrate provides a surface for adatoms to stick to and diffuse around. After the deposition, the oxide thin films are usually cooled down in an oxygen atmosphere (200 Torr) to reduce the oxygen vacancies.

Comparing with other deposition techniques, PLD has many significant advantages. First, PLD has a precise stoichiometry control, which means the chemical stoichiometry in the target can be maintained in the deposited thin films. By the different target preparation, a wide variety of the materials can be grown by PLD. Second, PLD has a simple growth condition control. Laser repetition frequency (1-10 Hz), laser energy (300-450 mJ), substrate temperature (650-750 ^{o}C) and oxygen pressure (vacuum to 200 mTorr) are the optimizable parameters for high quality oxide thin film growth. The substrate temperature affects the film crystallinity and phase separation in nanocomposite thin films and the oxygen pressure determines the growth rate, surface roughness and phase formation of the oxide thin films. All these growth parameters can be easily controlled by the equipment settings. Third, PLD is a clean process for thin film growth. In PLD depositions, the high vacuum condition reduces the impurities in the chamber and the laser beam is a clean energy source. Last, PLD is promising deposition technique for high quality multilayer films. By

putting multiple targets in the chamber and switching the targets during the deposition, the multilayer thin films can be easily grown without breaking the vacuum.
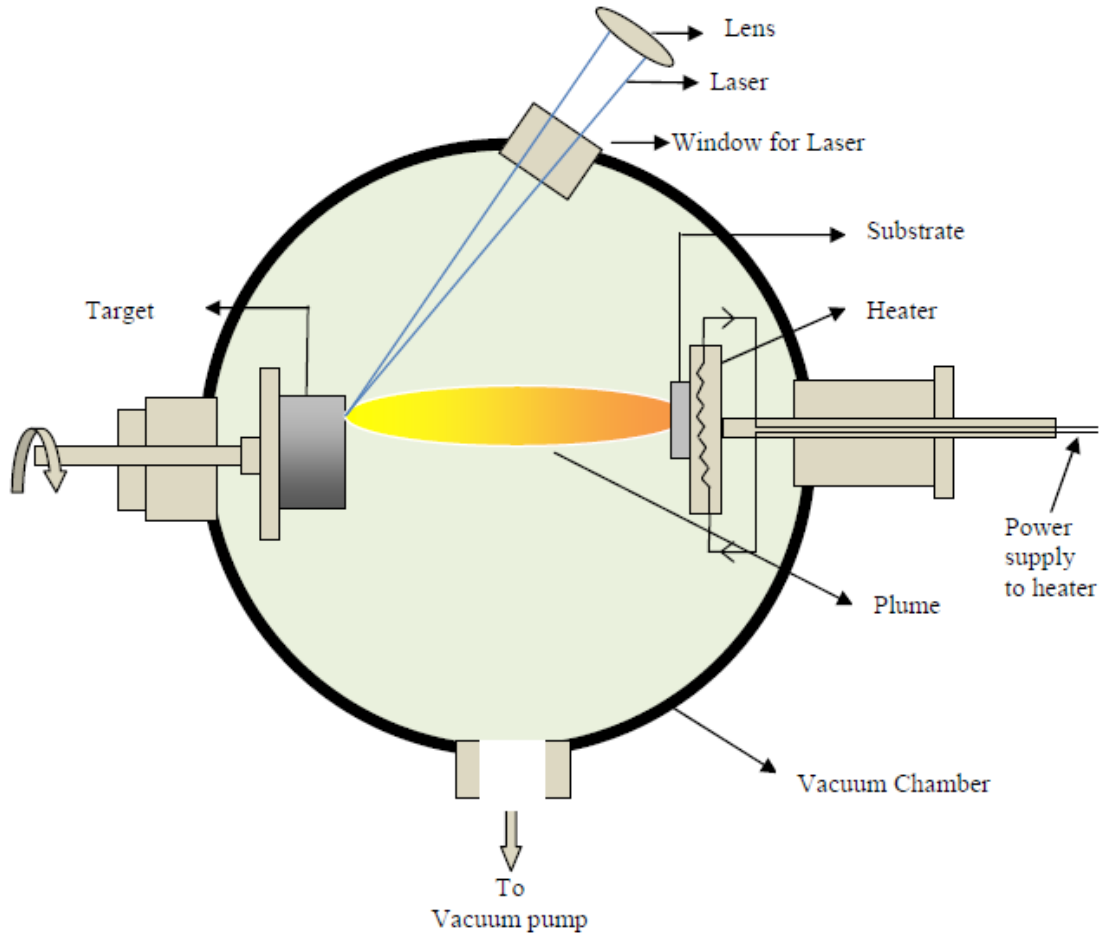
Figure 2.1 Schematic set-up of a pulsed laser deposition chamber.[66]

On the other hand, PLD still has many disadvantages that need more development. First, PLD has a limited deposition area. Due to the shape of the plasma plume, PLD deposition can only cover a substrate area of less than 1 cm^2, which is insufficient for industrial applications. Second, PLD is a relatively expensive growth method. The most costly parts in a PLD system is the laser source and pumping system (mechanical pump and turbo pump). Even though the cost for each system can be reduced by sharing the laser source with multiple PLD chambers, the cost for establishing a PLD system is still at a high level. Third, PLD might bombard the particulates from the target. The quality of the thin films could be impacted when the particulates are deposited on

the substrate. Despite of these drawbacks, the PLD is still a powerful tool for the integration of functional oxide thin films.

2.2   Microstructure characterization

2.2.1   X-ray diffraction

X-ray diffraction (XRD) is a widely used, non-destructive characterizing technique to analyze the microstructure of epitaxial thin films. Diffraction occurs when the wavelength of the incident X-ray is comparable to the atomic spacing in the material. This diffraction phenomenon was first proposed by William Henry Bragg and William Lawrence Bragg in 1913,[67] which obeys the Bragg's law:

$$n\lambda = 2d \sin \theta \tag{2.1}$$

Where n is an integer, λ is the wavelength of the incident X-ray (1.5406 Å for Cu K$_\alpha$), d is the crystal lattice spacing and θ is the diffraction angle. The schematic drawing in Figure 2.2 shows the Bragg diffraction for a set of crystal planes with the distance of d.[68]
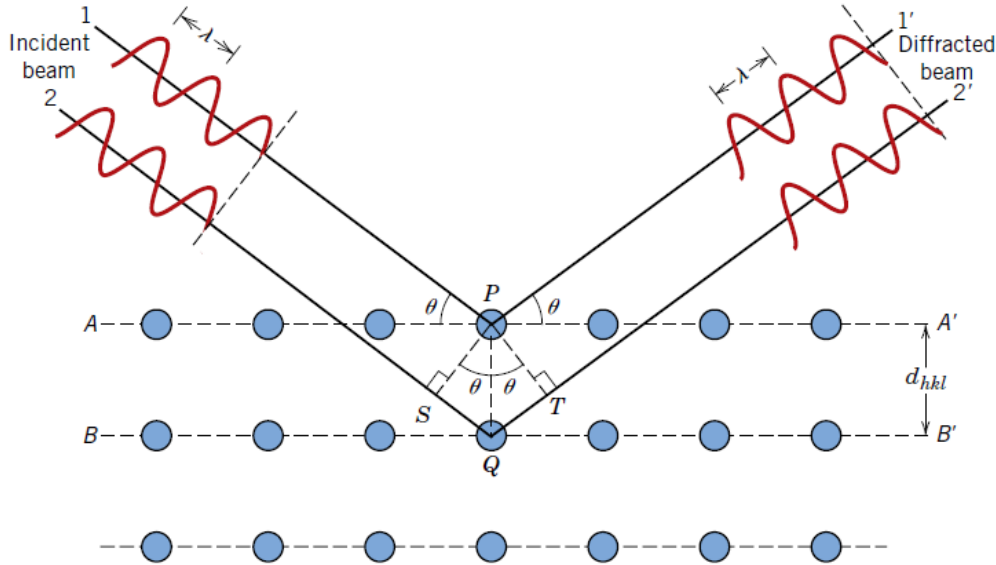
Figure 2.2 Bragg diffraction for a crystal plane with the distance of d.[68]

The θ-2θ XRD pattern is used to test the crystallinity and growth orientation of the material. The amorphous sample shows no diffraction peak and the full width at half maximum (FWHM) of the diffraction peak indicates the degree of the crystallinity. Besides, the angle of the diffraction peak can be used to calculate the lattice spacing and the shift of the diffraction peak indicates the existence of the strain inside the sample. The ω scan (rocking curve) is used to determine the lattice distortion. The φ scan is used to analyze the in-plane orientation. The reciprocal space mapping (RSM) is used to study the lattice constants, crystallinity and strain of the thin films.

2.2.2   Transmittance electron microscopy

TEM is one of the most powerful tool for the microstructure characterization of the thin films. In TEM, an electron beam is transmitted through the thin area of a special prepared sample and the microstructural image is formed due to the interaction of the electron beam and the sample. The working principle of the TEM is similar to a traditional optical microscopy, where the resolution is determined by the wavelength of the incident beam. By replacing the visible light (wavelength: hundreds of nm) with the electron beam (wavelength: 2.5 pm at 200 kV), the resolution of the TEM can be significantly enhanced.

TEM has two operation modes: the imaging mode and the diffraction mode. The equipment set-ups for these two modes are shown in Figure 2.3. The switch between these two modes can be achieved by adjusting the focal length of the intermediate lens, which is the imaging mode at the first image plane and diffraction mode at the diffraction plane. The imaging mode provides the atomic scale topographic image of the sample, while the diffraction mode provides the structural information including the crystal structure and lattice parameter. Beside of the conventional imaging, more advanced techniques have been developed in the TEM system, including the high-angle annular dark field (HAADF) scanning transmission electron microscopy (STEM), energy-dispersive X-ray spectroscopy (EDS) and electron energy loss spectroscopy (EELS). STEM provides the high-resolution atomic level images with the clear Z-contrast and EDS mapping provides the chemical composition information of the scanned area.

TEM sample preparation is a critical process to obtain high quality TEM images. A thin area with the thickness of less than 100 nm is required for the transmission of the electron beam, while the microstructure of the specimen has to be maintained. In this dissertation, we have prepared two types of the TEM samples: the cross-sectional samples to provide the information

along the substrate surface direction and the plan-view samples to provide the top-down information of the thin films. Both categories of TEM samples were prepared in the following steps. (1) Cut the sample to the appropriate size. (2) Glue two pieces of samples face-to-face and heat to dry (for cross-sectional samples). (3) Pre-thinning of the glued sample to 40-70 μm. (4) Continually thin the sample to 20-25 μm by grinding and polishing. (5) Final-thinning of the sample by ion milling to obtain a hole with attached thin areas.
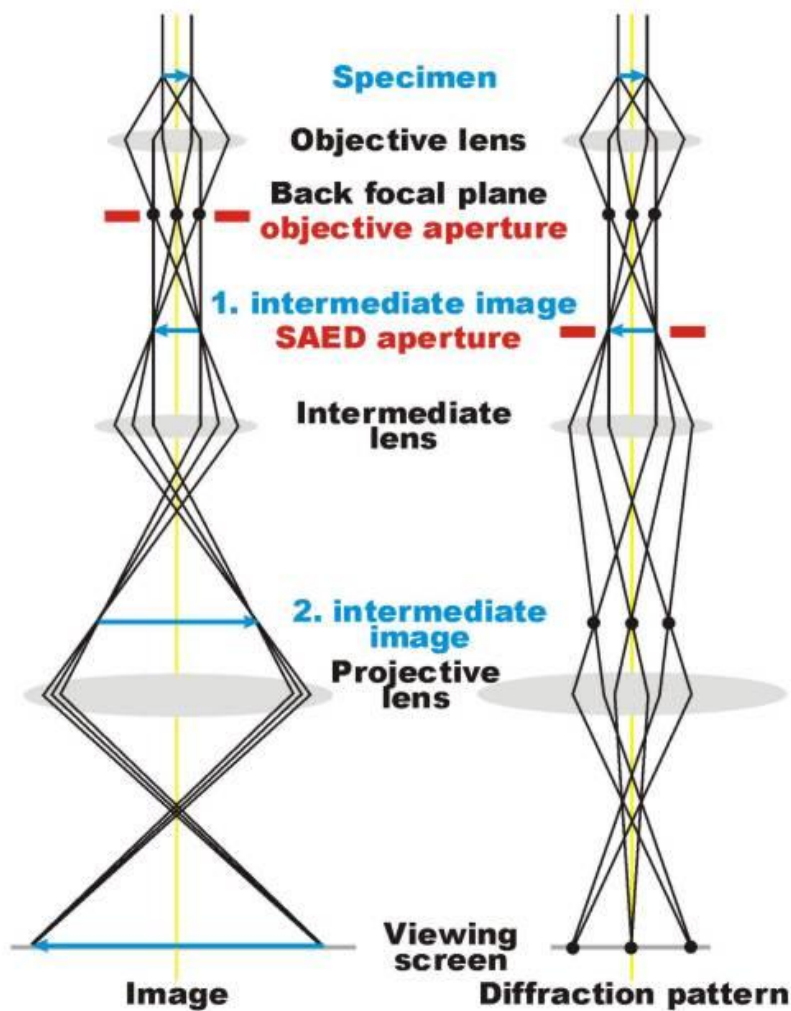
Figure 2.3 The schematic illustration of the imaging mode and diffraction mode in TEM.

2.3 Property measurement

2.3.1 Magnetic and magnetotransport property measurement

The magnetic properties of the oxide thin films was measured using a Magnetic Property Measurement System (MPMS, Quantum Design MPMS-3). MPMS is one of the most sensitive instrument for measuring the magnetic property of the thin films, bulk and powder materials, including moment vs magnetic field (M-H, magnetic hysteresis loops), moment vs temperature (M-T), magnetic susceptibility vs magnetic field (χ'-H), etc. MPMS provides a wide temperature sweep range from 1.8 to 400 K at the standard mode and 300 to 1000 K at the oven mode. The applied magnetic field can reach ±7 T with a high sensitivity of 10^{-8} emu. The frequency control for AC susceptibility measurement ranges from 0.1 to 1000 Hz. Besides, the magnetic property measurement can be conducted through the vibrating sample magnetometer (VSM) mode of the Physical Property Measurement System (PPMS, Quantum Design DynaCool).

For the M-H measurement, the magnetic field with fixed direction (vertical to the ground) is generated in the MPMS chamber. The out-of-plane or in-plane magnetic response of the thin films can be obtained by changing the mounting direction, as shown in Figure 2.4 (a). During the measurement, the sample vibrates under the control of a linear motor and generates the magnetic flux change, which is collected by the pick-up coil and transferred into the electrical signals.

The magnetotransport property of the thin films was measured using the PPMS. PPMS is a versatile platform for testing many physical properties, including electrical transport (magnetoresistance, Hall Effect and I-V curves), thermal transport (thermal conductivity and Seebeck & Nernst effect), magnetometry (DC magnetic moment) and ferromagnetic resonance. Customized probes and external electronics can be used to provide additional measurements. PPMS has a temperature control range from 1.8 to 400 K and a wider magnetic field range of ±9 T. The magnetotransport property in this dissertation was measured using the Resistivity and Electrical Transport Option (ETO) modes in the PPMS.

Before the magnetotransport measurement, gold contacts are prepared on the film surface for the wire connection. The top electrodes are connected to the sample puck under the Van der Pauw configuration (Figure 2.4 (b) and (c)). The ETO provides a resistance measurement from 1 mΩ to 3 MΩ at the four-wire mode and 1 MΩ to 5 GΩ with the two-wire mode. A magnetic field

can be applied during the cooling process to demonstrate the magnetoresistance property of the samples.
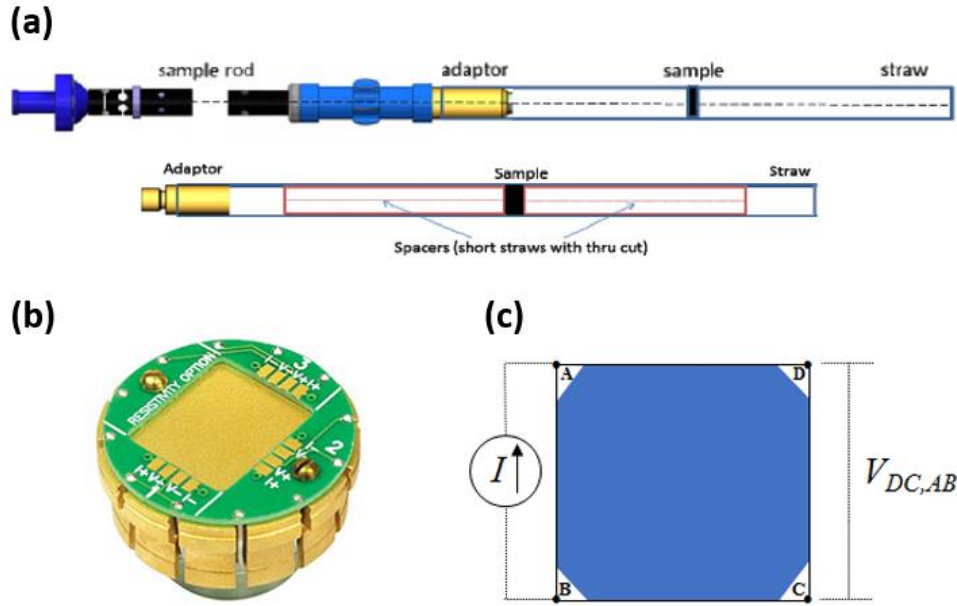
Figure 2.4 (a) Out-of-plane (top) and in-plane mounting method of the thin film sample using the straw. (b) Sample puck for Resistivity and ETO option in PPMS. (c) Van der Pauw configuration.

2.3.2 Electrical property measurement

The electrical property of the oxide thin films in this dissertation was examined by the piezoelectric force microscopy (PFM) option in an atomic force microscopy (AFM). AFM is a surface morphology and topography characterization equipment. In AFM, the cantilever tip scans over the sample surface and the vertical movement of the tip is recorded and transformed into the surface profile. Depends on the relative distance between the tip and sample surface, the AFM can be categorized into contact mode, tapping mode and non-contact mode. In the PFM option, a DC bias is applied at the conducting tip to measure the ferroelectric response of the sample (as shown in Figure 2.5 (a)). The ferroelectric measurement includes the domain writing/rewriting and phase/amplitude switching curves.

In domain writing, a voltage is first applied on the tip during the scan of a certain region, which causes the phase change of the material and this procedure is called the writing process. Thereafter, an opposite tip bias is applied during the scan of a smaller area inside the previous

65

region. The opposite tip bias causes the phase switching towards the opposite direction in the smaller area and this procedure is called the rewriting process. For the ferroelectric material, an 180° phase change can be observed when scanning the whole area after the wring and rewriting processes, as shown in Figure 2.5 (b).[69] The phase and amplitude curves are obtain by sweeping the tip bias at a fixed point on the sample, while the phase switched and butterfly like loops can be observed if the material is piezoelectric (Figure 2.5 (c-d)).[69]
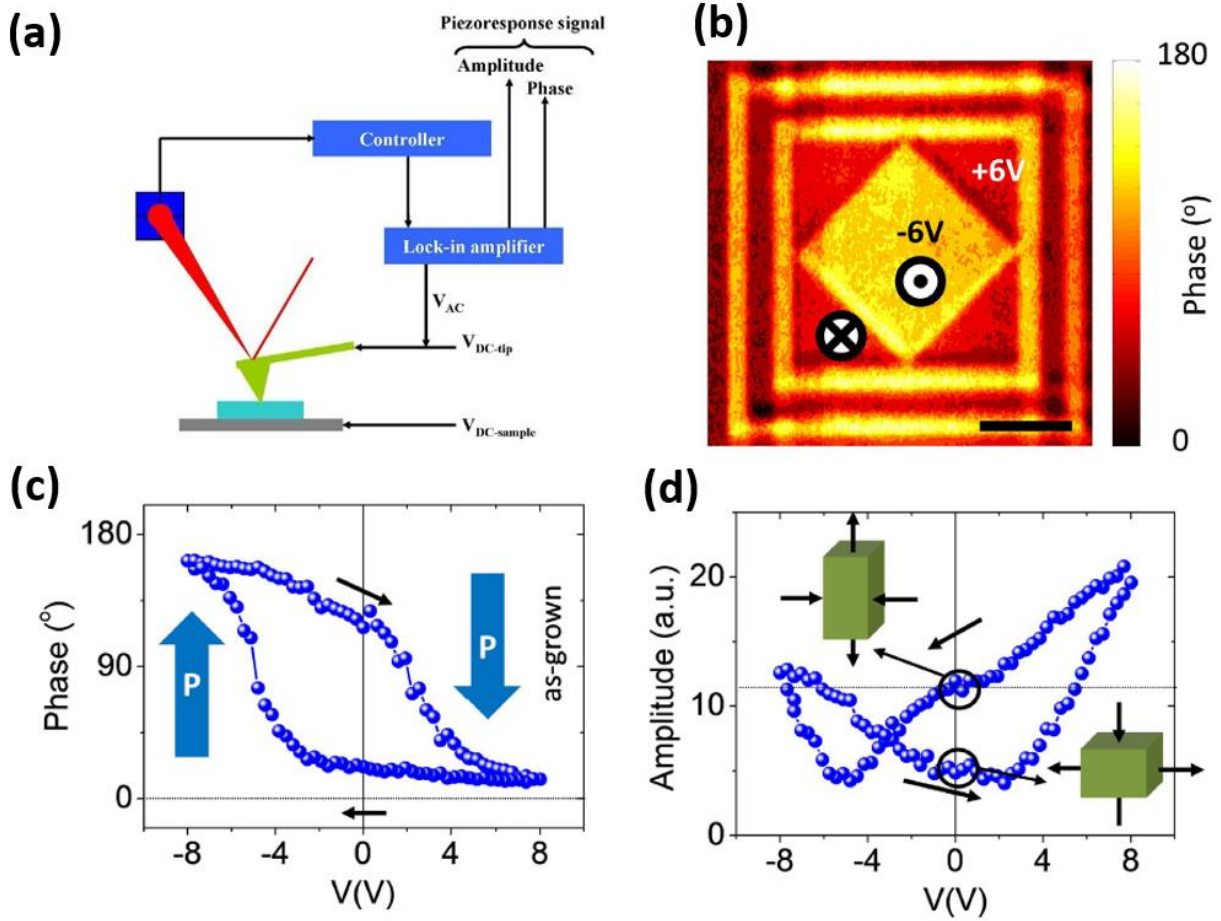
Figure 2.5 (a) Schematic set-up for PFM. (b) PFM phase image. (c) Phase switching curve. (d) Amplitude switching curve of a BTO:CFO thin film.[69]

2.3.3 Optical property measurement

The transmittance of the oxide thin films was measured using an optical spectrophotometer (Lambda 1050 UV/Vis Spectrophotometer). The light with a spectra range from 175 to 3300 nm is generated by the Tungsten-halogen and Deuterium lamps. During the measurement, a filtered

light beam with varies wavelength is illuminate on the transparent samples. The intensity of light transmitted through the sample is recorded and its ratio to the intensity measured without the sample (the reference) is defined as the transmittance of the material. A bare substrate was also measured to exclude the impact from the substrate. The incident beam is rotatable to study the angular dependence of the optical property. After the measurement, the band gap of the thin films can be calculated by using the Tauc method. The schematic set up of a UV-Vis spectroscopy is shown in Figure 2.6.
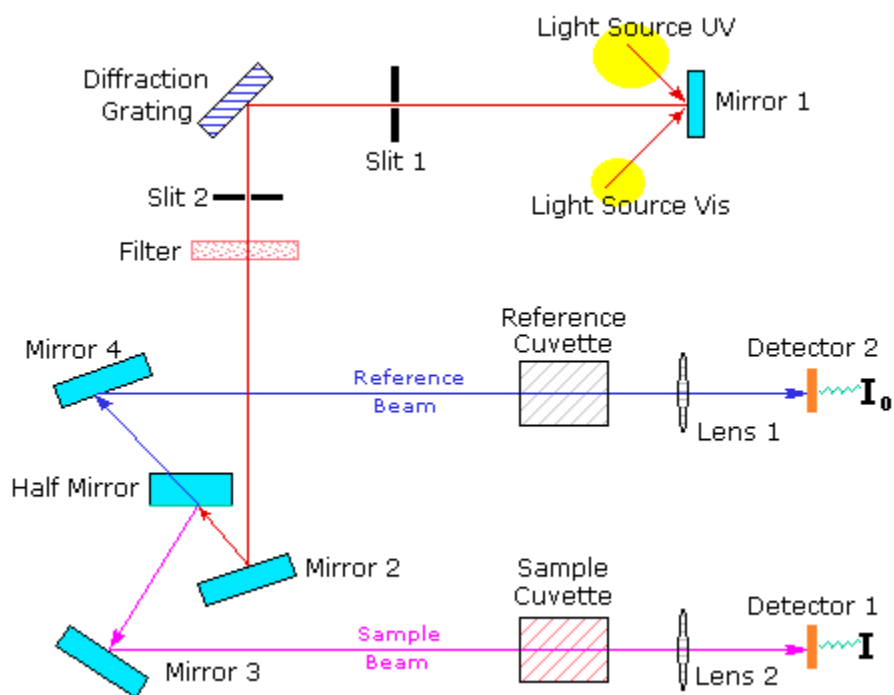
Figure 2.6 Schematic set up for a UV-Vis spectroscopy.

3. VERTICALLY ALIGNED NANOCOMPOSITE BATIO3:YMNO3 THIN FILMS WITH ROOM-TEMPERATURE MULTIFERROIC PROPERTIES TOWARDS NANOSCALE MEMORY DEVICES

3.1 Overview

Self-assembled epitaxial $BaTiO_3$:$YMnO_3$ (BTO:YMO) vertically aligned nanocomposite thin films have been fabricated on $SrTiO_3$ (001) substrates using pulsed laser deposition. Room-temperature multiferroic response has been demonstrated in the thin films. Enormous strain has been generated in both phases (e.g., 1.4% compressive strain in BTO and 6.8% tensile strain in YMO out-of-plane) due to the large lattice mismatch. By tuning the deposition frequency, the microstructure and strain of the nanocomposite films are tailored, which leads to the property tuning in the nanocomposite films. It is found that strain plays an important role on the magnetic ordering of YMO and thus results in the room temperature ferromagnetic response. Combined with the ferroelectric response in the BTO:YMO nanocomposite thin films, a new room temperature multiferroic two-phase nanocomposite has been demonstrated. The room temperature magnetoelectric (ME) coupling has been demonstrated for this new system. Overall, the BTO:YMO thin film presents promising applications in sensors, data storage and memory devices.

3.2 Introduction

Multiferroic materials, which possesses two or all of the three properties: ferroelectricity, ferromagnetism and ferroelasticity[70], have attracted a broad attention because of their potential applications in magnetic data storage, nonvolatile memory and sensors[12,71–73]. For example, $BiMnO_3$ is a well-studied multiferroic material that possesses both ferroelectricity and ferromagnetism[74,75]. However, ferromagnetic and ferroelectric properties often exclude each other due to their required electronic structure, thus single-phase multiferroic materials are very rare in nature[76,77]. As a result, the research of multiferroics have been expanded to antiferromagnetic materials. $YMnO_3$ (YMO) is a rare earth oxide and has been reported with ferroelectric and antiferromagnetic response[78], which presents potential applications in nonvolatile memory devices[79] and exchange bias systems[80]. YMO has two polymorphs in different crystal structures, i.e., hexagonal and perovskite (orthorhombic, O-YMO) structures. Hexagonal YMO is more stable

in bulk form, while orthorhombic structure can be stabilized either under low temperatures[81], using high pressure synthesis[82], or via epitaxial thin film growth[83]. The physical properties of the two structures are also different. It has been reported that the growth of orthorhombic YMO (O-YMO) can be manipulated by substrate selections[83,84] and substrate orientation[85]. For example, the stabilization of O-YMO on SrTiO₃ (STO) substrate via pulsed laser deposition (PLD) technique has been reported[83,86]. It has been reported that O-YMO is a multiferroic material that has both ferroelectric and antiferromagnetic properties under very low temperatures ($T_C \sim 30$ K, $T_N \sim 45$ K) [77,84,85,87]. Interestingly, an "unexpected" ferromagnetic response was observed close to its Neel temperature in O-YMO and was claimed to be due to the change of strain state in the film[88].

Because of the abovementioned challenges in searching for new single-phase multiferroic systems, the nanocomposite approach combining two phases with different ferroic orderings has been adopted[21-24]. Multiferroic property in many two-phase systems, such as $BaTiO_3$:$CoFe_2O_4$[89], $Pb(Zr,Ti)O_3$:$CoFe_2O_4$[90,91] and $BiFeO_3$:$CoFe_2O_4$[92], has been reported. Moreover, strong vertical interfacial strain in two-phase nanocomposite systems has been reported to be capable of manipulating the properties of the composites[91]. Among all of the two-phase systems, vertically aligned nanocomposites thin films have become a strong candidate due to their novel architecture, vertically interfacial strain control and tunable material functionalities[42,50]. Zhang *et al.* have reported the magnetic anisotropy, coercive fields and ferroelectric switching behavior in multiferroic $BiFeO_3$-$CoFe_2O_4$ nanocomposite thin films can be tuned by strain accommodation and interface coupling between phases, which could be manipulated by tuning deposition frequencies[92]. Some theoretical studies have also been performed to illustrate the effect of the strain on the magnetocapacitance[93], magnetoelectric effect[94] and dielectric response[95] of self-assembled nanocomposite thin films.

In this work, YMO is coupled with $BaTiO_3$ (BTO) in an epitaxial vertically aligned nanocomposite thin film form with the goal to tune the magnetic properties of YMO through vertical strain coupling and thus achieves a multifunctional YMO-based nanocomposite system. $BaTiO_3$ (BTO) is selected as the secondary phase as it is a well-studied ferroelectric material under room temperature. It has been reported that the ferroelectric transition temperature and remanent polarization of BTO thin films can be significantly enhanced by introducing biaxial strain from substrate[96]. As shown in the schematic drawings in Figure 3.1 (a), the BTO ($a_{BTO} = 0.399$ nm, $c_{BTO} = 0.404$ nm) lattice matches well on STO substrate ($a_{STO} = 0.391$ nm) while O-YMO presents a

large mismatch with both the BTO and STO. After an in-plane 45º rotation, the YMO in-plane matching distances are reduced to 0.393 nm, which result in the mismatch of 0.51% along a- and b-axis with STO. The YMO c-axis lattice parameter is 0.736 nm and thus it is expected that one of the YMO (002) lattice matches with two of the BTO (002) lattices in the vertical direction and results in a large tensile strain of 9.78% in YMO out-of-plane. As shown in Figure 3.1 (b), by varying the laser deposition frequency, we expect that the vertically aligned nanocomposite structures can be tuned as functions of pillar size and density. The ferroelectric and ferromagnetic properties are measured and correlated with the nanocomposite microstructures such as pillar sizes, pillar density and the resulted film strain. The ferromagnetic properties of the YMO phase under room temperature are discussed and compared with pure YMO thin films to explore the power of the strain coupling introduced by the nanocomposite structures.
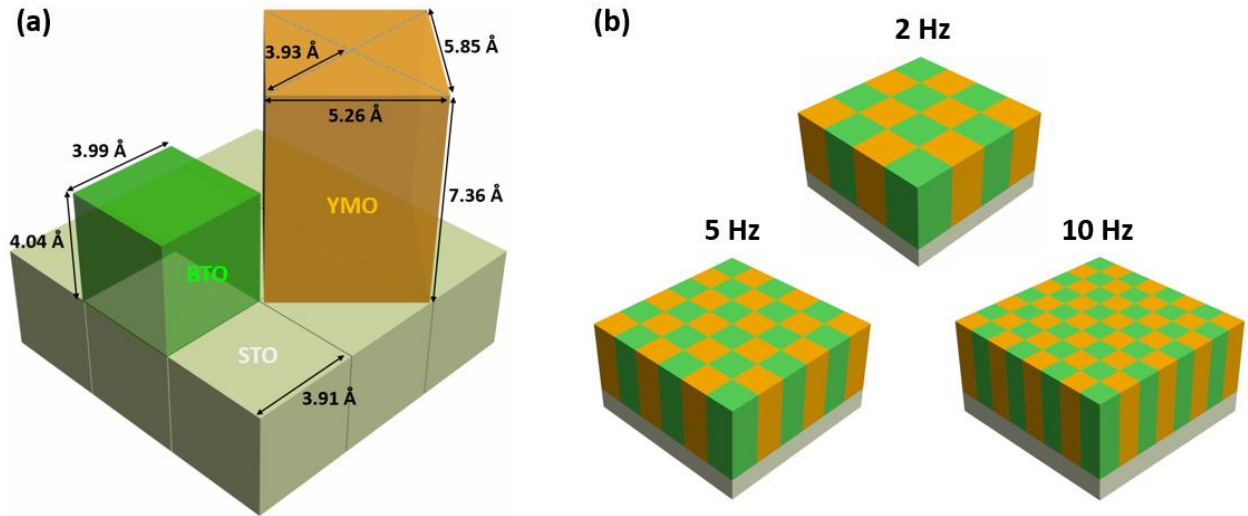
Figure 3.1 (a) Schematic drawing of lattice matching relationship of BTO, YMO and STO unit cells. (b) Schematic drawing of BTO:YMO vertically aligned nanocomposite thin films with different deposition frequencies.

3.3   Experimental

BTO:YMO thin films with the molar ratio of 1:1 were deposited on single-crystal STO (001) substrates by pulsed laser deposition (PLD). During deposition, the deposition frequency was varied from 2 Hz, 5 Hz to 10 Hz. The microstructure of the as-deposited films was characterized by X-ray diffraction (XRD) and transmission electron microscope (TEM). Magnetic properties were examined using a vibrating sample magnetometer (VSM) option in a commercial Physical

Properties Measurement System (PPMS). Ferroelectric properties were investigated using an atomic force microscope (AFM)/piezoresponse force microscope (PFM). Magnetoelectric coupling was measured using a Magneto-electric Bundle.

3.4   Results and discussion

The growth quality of BTO:YMO nanocomposite films was first characterized by XRD. Figure 3.2 (a) shows the XRD θ-2θ pattern of the films grown at 2 Hz, 5 Hz and 10 Hz, respectively. Clear peaks were observed for BTO (00l) and YMO (00l), suggesting a preferential out-of-plane orientation of (00l) for both phases. No obvious impurity peaks are observed, indicating no obvious secondary phase formation and intermixing between BTO and YMO phases. Figure 3.2 (b) shows the local XRD scans near the STO (002) peak to demonstrate the peak shift and strain tuning. Both single-phase BTO and YMO films were grown on STO (001) substrates as a baseline, where the BTO (002) and YMO (004) peaks are located at 45.54° (c = 0.398 nm) and 50.08° (c = 0.729 nm), which were labeled as thin solid lines in Figure 3.2 (b) (the plot of the calculated lattice parameters based on the peak positions), respectively. Comparing with the reference peaks, BTO (002) shifts to higher angles (lower $c_{(002)}$-spacing), which suggests an increasing compressive strain along the out-of-plane direction, as the deposition frequency increases. For the YMO phase, we expected that the YMO (004) shifts to lower angles (larger $c_{(004)}$-spacing), which results from an increasing tensile strain along the out-of-plane direction, as the frequency increases. From the XRD result, a clear left shift of YMO (004) is observed for the film deposited at 10 Hz, compared with the 2 Hz and 5 Hz samples, which is also demonstrated in the corresponding calculated c-axis d-spacing in Figure 3.2 (c). It is noted that the 2 Hz and 5 Hz samples present a very similar c-axis d-spacing value, and both are much smaller than that of the 10 Hz sample. As a result, the strain tuning by deposition frequencies has been effectively demonstrated in the BTO:YMO nanocomposites. The origin of the vertical strain is correlated to the lattice mismatch between the two phases in the out-of-plane direction discussed above. From the XRD pattern of the baseline samples (pure BTO and YMO films), the out-of-plane lattice parameters of pure BTO and YMO are 0.398 nm and 0.729 nm, respectively, which confirms the domain matching relationship between two phases, i.e., two of the BTO unit cells (0.796 nm) with one YMO unit cell (0.729 nm). As a result, a compressive (tensile) strain exists in BTO (YMO) phase, which is consistent with the stain tuning based on the XRD results.
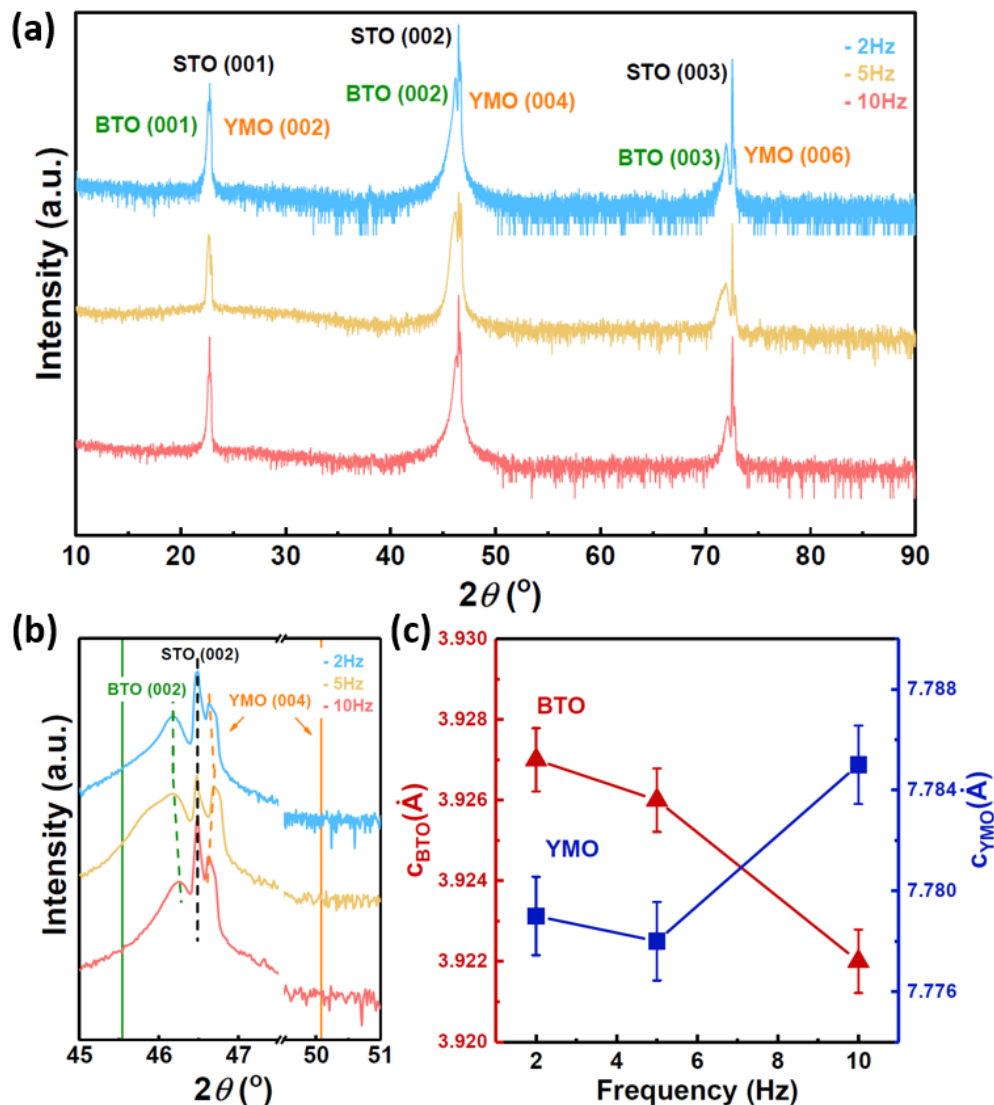
Figure 3.2 (a) θ-2θ XRD scans of BTO:YMO nanocomposite films with different deposition frequencies. (b) Local θ-2θ XRD scans near STO (002) of BTO:YMO nanocomposite films with different deposition frequencies, the dashed lines indicate the shifting trend of BTO (002) and YMO (004) peaks and the solid lines indicate the peak position of single phase BTO and YMO samples. (c) Out-of-plane lattice parameter of BTO and YMO phases with different deposition frequencies.

To understand the microstructure and strain tuning in the samples deposited under various frequencies, the microstructure of BTO:YMO films was further investigated by TEM and scanning transmission electron microscopy (STEM). Figure 3.3 (a) shows the low magnification cross-section TEM image of the BTO:YMO film deposited at 5 Hz with the inset showing the corresponding selected-area electron diffraction (SAED) pattern. The 5 Hz BTO:YMO film is

approximately 200 nm thick and has an obvious columnar structure of the two phases. The SAED pattern indicates that the orientation relationships between the two phases and the substrate are $(001)_{BTO}//(002)_{YMO}//(001)_{STO}$ and $(010)_{BTO}//(110)_{YMO}//(010)_{STO}$, which are consistent with the predictions in the schematic drawing in Figure 3.1 (a). Figure 3.3 (b) shows the cross-sectional STEM image of the 5Hz sample taken under the high angle annular dark field mode (also called Z-contrast mode). In both Figure 3.3 (a) and (b), clear vertical columns of BTO (B) and YMO (Y) are shown. Specifically, the high-resolution TEM image in Figure 3.3 (c), clearly presents the bright columns of the YMO phase (marked as Y) and the dark columns of the BTO phase (marked as B). The contrast is exactly opposite in the case of STEM image in Figure 3.3 (b), i.e., brighter columns of BTO phase (higher Z number) and darker columns of YMO phases (lower Z number). The average column width of the BTO and YMO phases for different deposition frequencies was calculated from the TEM/STEM images and summarized in Figure 3.3 (d). The overall trend is that, as the deposition frequency increases, the column sizes decrease from 25.9 nm (BTO) and 13.5 nm (YMO) at 2 Hz to about 11.9 nm (BTO) and 5.1 nm (YMO) at 10 Hz. This trend is consistent with our expectations in Figure 3.1 (b) as well as previous frequency studies of other vertically aligned nanocomposite systems[92,97,98]. For vertically aligned nanocomposite, the column width depends on the size of the nucleation islands of each phase, which is a result of the diffusion of adatoms on the substrate surface[42]. As the deposition frequency increases, the resting time (diffusion time) for the adatoms between the laser pulses reduces and thus results in smaller nucleation islands and thinner columns of each phase. As a result, the density of the vertical interfaces between the YMO and BTO phases increases and thus results in a stronger vertical strain coupling in the two phases as demonstrated in Figure 3.2 (b) and c., i.e., the increased compressive strain in BTO and the stronger tensile strain in YMO, both out-of-plane. In this work, we adopted the laser frequency of 2, 5 and 10 Hz, since each frequency is about two time apart from each other to effectively tune the deposition rate and the adatoms' nucleation process on the substrates. Specifically, a higher frequency, e.g., 10 Hz, will result in a faster growth and shorter resting time for the adatoms on the substrates. This will result in a shorter diffusion time and thus a smaller column width. Such nanopillars diameter tuning will result in effective tuning of the vertical interface density and the vertical strain coupling.
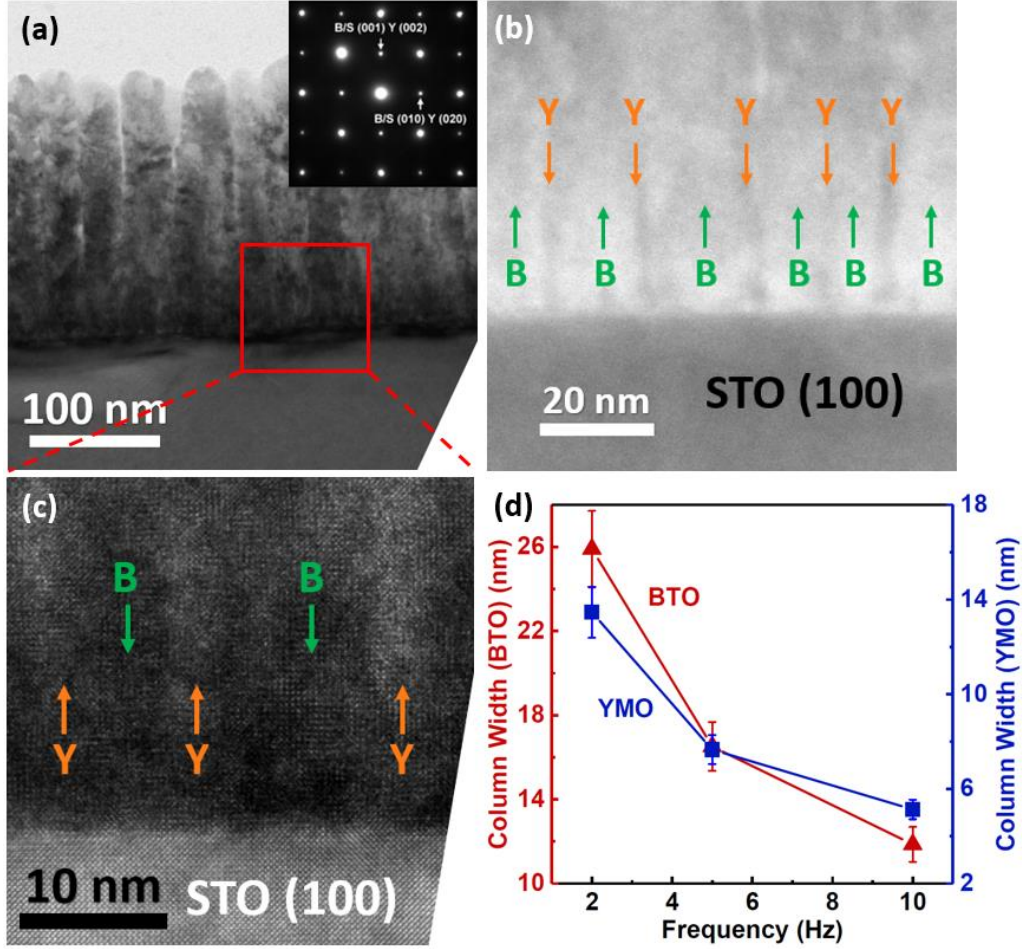
Figure 3.3 (a) Cross-sectional TEM (with inset of corresponding selected area electron diffraction). (b) STEM and (c) HRTEM image of BTO:YMO thin films deposited at 5 Hz. (d) Column width of BTO and YMO phases at different deposition frequencies.

The magnetic property of the nanocomposite thin films was examined by VSM measurements using PPMS under room temperature. Figure 3.4 (a) and b show the out-of-plane (OP) and in-plane (IP) magnetic hysteresis (M-H) loops of the films deposited at different frequencies, respectively. It is clear that the room-temperature ferromagnetic response of the BTO:YMO nanocomposite films is obtained in both IP and OP directions. Such room temperature ferromagnetic response from YMO is believed to result from the vertically aligned nanocomposite structure and the unique strout-ain coupling in YMO, e.g., the strong tensile strain in OP direction and a large c-axis lattice of 0.779 nm (for the 2 Hz sample). Based on previous studies on YMO, it was suggested that O-YMO could be antiferromagnetic under thin film form[85]. However, a ferromagnetic response close to the Neel temperature (~ 40 K) for O-YMO film grown on STO

(001) substrates was reported and the magnetization of the films increased with increasing substrate-induced strain[88]. The obvious room temperature ferromagnetic properties observed in the YMO:BTO nanocomposite could be resulted from two sources. First, the observed ferromagnetic response in antiferromagnetic materials could be resulted from the uncompensated spins at the interfaces. For example, NiO and Co_3O_4 are both antiferromagnetic in bulk form. However, it was reported that NiO[99] and Co_3O_4[100] nanoparticles show ferromagnetic property, due to uncompensated spins at the nanoparticle interface. For this case, the high density vertical interfaces of the YMO columns present uncompensated spins and thus result in the observed ferromagnetic properties. Second, the large strain exists in the YMO phase, causes the lattice distortion in the YMO and thus leads to the observed room-temperature ferromagnetic property. More interestingly, the films show enhanced ferromagnetic property in the OP direction, i.e., obviously enhanced OP anisotropy, as the deposition frequency increases. The enhanced OP anisotropy may be a result of the increased vertical strain coupling between the BTO and YMO phases as the density of the vertical interfaces increases. This frequency tuning result again confirms that the strain between the BTO and YMO phases play an important role on the ferromagnetic property and can be further tuned by the vertically aligned nanocomposite structures. Besides, the smaller pillar sizes and increased density of phase boundaries could cause more uncompensated spins in the YMO phase, and thus lead to the increased ferromagnetic response in the OP direction. On the other hand, magnetization gets weaker slightly IP as the deposition frequency increases. This can also be correlated with the reduced diameter of the YMO pillars as the deposition frequency increases. As a result, as the deposition frequency increases, the column width reduces, the vertical interface density increases, and the ferromagnetic property shows the preferred OP anisotropy with the opposite trend in the IP and OP directions. Table 3.1 summarizes the values of magnetization saturation in IP (M_{S-IP}) and OP (M_{S-OP}) directions and the ratio of the saturation (M_{S-IP}/M_{S-OP}) in IP and OP directions of the thin films deposited at different deposition frequencies. For the film deposited at 10 Hz, the ratio is less than one, which again confirms the strong OP anisotropy in the ferromagnetic property.

Table 3.1 Magnetization saturation in the in-plane (IP) and out-of-plane (OP) directions and the ratio of saturation in the IP and OP direction of BTO:YMO nanocomposite films deposited at different frequencies.

	2 Hz	5 Hz	10 Hz
M_{S-IP} (emu/cm^3)	95.1	86.0	74.1
M_{S-OP} (emu/cm^3)	47.0	56.9	85.6
M_{S-IP}/M_{S-OP}	2.02	1.51	0.87

Figure 3.4 (c) shows the PFM OP phase image of the 5 Hz sample measured at room temperature. The piezo response writing experiments were performed on a 1 x 1 μm^2 area using a +5 V bias followed by a central writing on a 0.5 x 0.5 μm^2 area using a -5 V bias applied on the PFM tip. The ferroelectric domain switching of BTO phase is clearly seen in Figure 3.4 (c), i.e., bright contrast in the -5 V region and dark contrast in the +5 V region. Figure 3.4 (d) shows the corresponding phase and amplitude switching curves of the same sample. A sharp phase switching by 180° is observed, which indicates the obvious ferroelectric nature of BTO:YMO thin films. The butterfly-like loops of the amplitude signal and the hysteresis behavior of the phase signal further demonstrate the ferroelectricity of the BTO:YMO thin films. Based on the PFM writing results in Figure 3.4 (c), it shows obvious domains with high or low contrast regions, which suggests the strong and weak ferroelectric responses from the BTO and YMO domains, respectively. These results suggest that both BTO and YMO phases in the nanocomposites are ferroelectric but with different strength.
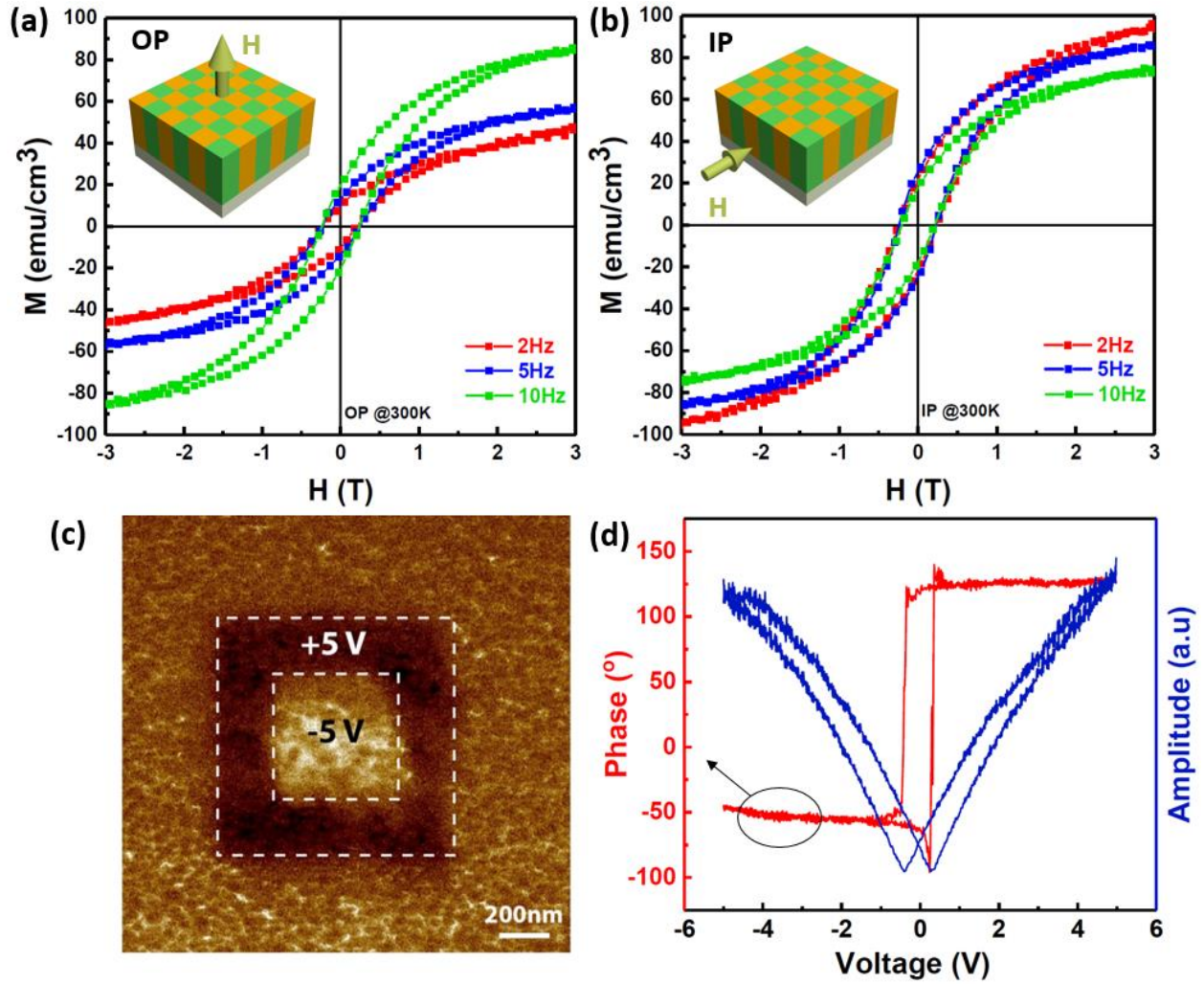
Figure 3.4 (a) Out-of-plane (OP) and (b) in-plane (IP) magnetic hysteresis loops of BTO:YMO nanocomposite films deposited at different frequencies and corresponding schematic drawing (inset). (c) PFM phase image of BTO:YMO nanocomposite film deposited at 5 Hz after +5 V writing and -5 V rewriting. (d) Phase and amplitude switching behavior as a function of tip bias.

As the range of ME materials is not a subset of the multiferroic material[72], i.e., not every multiferroic system is magnetoelectric, in this study, room temperature ME coupling of the BTO:YMO nanocomposites has been measured and demonstrated. Figure 3.5 shows the polarization of the BTO:YMO thin film deposited at 5 Hz with a varied magnetic field applied at room temperature. The black line shows the linear fitting result and the slope of the plot indicates the ME charge coefficient α, which is around 2.21×10^{-4} $\mu C/(cm^2 Oe)$. The relationship between the ME charge coefficient α and ME voltage coefficient α_{ME} is: $\alpha = \alpha_{ME} \varepsilon_0 \varepsilon_r$, where ε_0 and ε_r indicate the vacuum permittivity and relative permittivity of the film, respectively. Here, the room

temperature relative permittivity of the BTO thin film[101] is used in the calculation. The calculated ME voltage coefficient is 4.99 V/(cmOe). This value is comparable with other reported BTO-based two-phase systems[102,103].
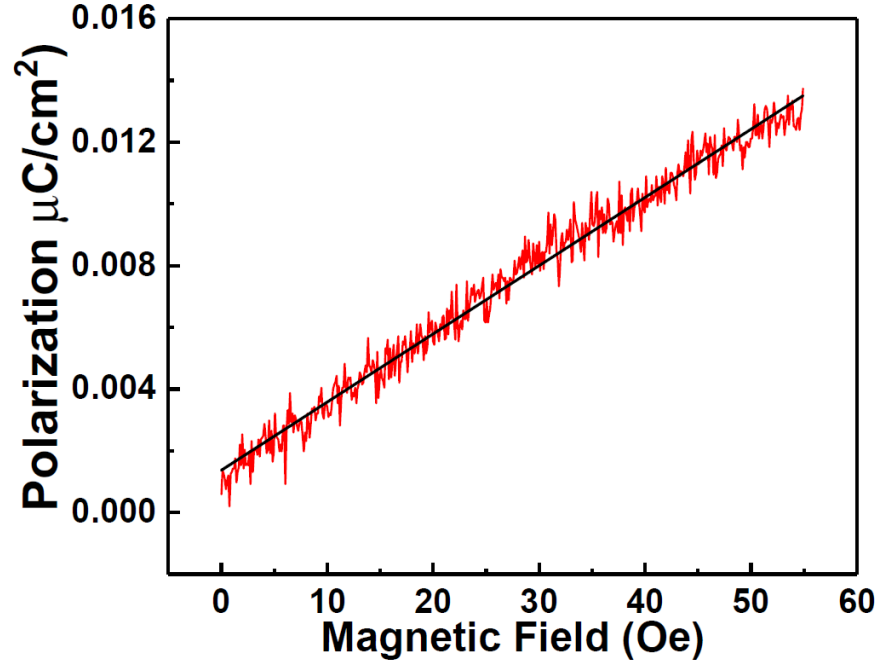
Figure 3.5 Room temperature polarization vs magnetic field of BTO:YMO nanocomposite deposited at 5 Hz. The black solid line indicates the result of linear fitting.

Overall, through the vertical strain coupling in the BTO:YMO vertically aligned nanocomposite thin films, the YMO phase shows a large tensile strain in c-axis, which could be responsible for the observed room temperature ferromagnetic and ferroelectric properties. As mentioned above, O-YMO has been reported to possess ferroelectric and antiferromagnetic properties under low temperatures ($T_C \sim 30$ K, $T_N \sim 45$ K) [77,84,85,87]. The deposition frequency effectively tunes the vertical domain dimensions and the density of the vertical interfaces, and thus leads to the enhanced vertical strain coupling as the deposition frequency increases. Such tunable vertical strain coupling (e.g., increasing OP tensile strain) also effectively alter the physical properties of the YMO phase, such as obvious ferromagnetic properties and ferroelectric response under room temperature.

3.5   Conclusion

In summary, BTO:YMO vertically aligned nanocomposite thin films have been grown on STO (001) substrates using the PLD technique. Obvious multiferroic property, i.e., ferromagnetic and ferroelectric property, has been demonstrated at room temperature. The lattice parameters and the resulted strain of both YMO and BTO are tuned effectively by the deposition frequency, i.e., as the deposition frequency increases, the column widths reduce for both phases and thus results in higher density vertical interfaces and a stronger vertical strain coupling. Such systematic strain tuning also results in enhanced ferromagnetic anisotropy out-of-plane in the 10 Hz sample. Coupled with the obvious ferroelectric response and ME coupling, BTO:YMO vertically aligned nanocomposite systems have been demonstrated as a new multiferroic vertically aligned nanocomposite system at room temperature towards future nanoscale memories, sensors, spintronics, and data storage devices.

4. TUNABLE LOW-FIELD MAGNETORESISTANCE PROPERTIES IN (LA0.3CA0.3MNO3)1-X:(CEO2)X VERTICALLY ALIGNED NANOCOMPOSITE THIN FILMS

4.1 Overview

Vertically aligned nanocomposite (VAN) $(La_{0.7}Ca_{0.3}MnO_3)_{1-x}$:$(CeO_2)_x$ thin films have been deposited on $SrTiO_3$ (001) substrates by pulsed laser deposition. Enhanced low-field magnetoresistance properties and tunable metal-insulator transition temperature (T_{MI}) have been demonstrated via modulating the composition of $(La_{0.7}Ca_{0.3}MnO_3)_{1-x}$:$(CeO_2)_x$ (x = 0, 0.05, 0.1 and 0.2). By increasing the atomic percentage of the CeO_2 phase to 20%, a maximum magnetoresistance value of 51.8% can be achieved and the T_{MI} can be tuned from 113 K to 210 K. The enhanced magnetoresistance properties are attributed to disordered grain boundary and tunneling structure generated by the insulating CeO_2 phase. The change of the T_{MI} is attributed to the strain state in the $La_{0.7}Ca_{0.3}MnO_3$ phase. Furthermore, high ferromagnetic anisotropy and enhanced magnetization have been demonstrated in the VAN system. The work demonstrates the power of multifunctionalities and property tuning in the VAN thin films.

4.2 Introduction

Recently, perovskite type manganese oxides with the formula of $RE_{1-x}A_xMnO_3$ (RE = rare earth, A = Ca, Sr, Ba, Pb) have attracted significant interests due to their strong colossal magnetoresistance (CMR) property[104,105] which exhibits a large decrease of resistance under an external magnetic field and shows great potential for spintronic device applications.[106] However, the application of such CMR phenomenon is often limited by the required high magnetic field (usually several Tesla). Thus, extensive efforts have been focused on the exploration of the low field magnetoresistance (LFMR) with the required magnetic field lower than 1 T.[107–109] It has been reported that the LFMR can be induced from the CMR materials by artificially introducing the grain or phase boundaries.[107,110–112] $La_{1-x}Ca_xMnO_3$ (LCMO) is a well-studied manganese oxide with CMR property[113] and its LFMR property has been discovered by introducing grain boundaries[111] or secondary phase.[114,115] Besides its magnetoresistance properties, LCMO also shows strong ferromagnetic property at low temperatures for potential applications in magnetic

80

recording media.[116] These properties make LCMO a strong contender within the $RE_{1-x}A_xMnO_3$ family.

As above mentioned, phase boundary plays an important role in generating the LFMR in CMR materials. Incorporating an insulating secondary phase into the CMR material is an effective approach for forming the phase boundaries. Among all the two-phase thin film systems, vertically aligned nanocomposites (VAN) present a unique alternating pillar-like structure with high density vertical phase boundaries. Enhanced LFMR properties have been reported in many VAN systems such as: $La_{1-x}Sr_xMnO_3$ (LSMO):CeO_2,[40,117–119] LSMO:ZnO,[98,120,121] LSMO:Mn_3O_4[122] and LSMO:NiO.[123] The LFMR property in these LSMO-based films can be tuned by changing the film composition[40] and pillar dimension via varying the deposition frequency.[117] For example, the metal-insulator transition from low temperature to high temperature can be found in many manganese oxides. By incorporating a secondary phase, it has been reported that the metal-insulator transition temperature (T_{MI}) of the films can be tuned by varying the concentration of the secondary phase, which is resulted from the phase boundary density variation within the films.[124,125] Despite the fact that tremendous LSMO-based VAN systems have been reported, it is still rare to systematically explore other $RE_{1-x}A_xMnO_3$ manganese oxide nanocomposite systems.

In this work, we conducted the study on a LCMO based VAN system. $La_{0.7}Ca_{0.3}MnO_3$ (LCMO) has been selected as the matrix material for the study. CeO_2 has been chosen as the secondary phase due to the following reasons: (1) CeO_2 is an insulating material as the electron transport barrier and has been reported in other VAN systems;[40,117] (2) CeO_2 has a good lattice matching with LCMO and the $SrTiO_3$ (STO) substrate (after 45º in-plane rotation). The schematic drawings in Figure 4.1 (a) and b show the lattice matching relationships of the LCMO, CeO_2 and STO. LCMO (a_{LCMO} = 3.86 Å) lattices with a cube-on-cube growth mechanism on STO (a_{STO} = 3.905 Å) because of the small lattice mismatch (-1.2%) while CeO_2 (a_{CeO2} = 5.411 Å) lattices have a 45º in-plane (IP) rotation ($a_{CeO2}/\sqrt{2}$ = 3.83 Å) to decrease the lattice mismatch (38.6% to -1.9%), as shown in Figure 4.1 (a) and the top section of Figure 4.1 (b). In VAN thin films, domain matching of the two phases is highly possible as it can significantly decrease the lattice mismatch along the vertical direction. In this work, the matching of 3 LCMO unit cells (11.58 Å) with 2 CeO_2 unit cells (10.822 Å) or 4 LCMO unit cells (15.44 Å) with 3 CeO_2 unit cells (16.233 Å) is predicted as it can significantly decrease the lattice mismatch (40.2% to -6.5% and 5.1% in LCMO, respectively). The drawing of the domain matching relationship is plotted at the bottom of Figure

4.1 (b) and has been further confirmed by the experimental results to be discussed later. Figure 4.1 (c) shows the predicted pillar in matrix structure of the LCMO:CeO$_2$ VAN thin films. By varying the phase composition, we explored the tuning of the maximum MR, T$_{MI}$ and magnetic properties in the VAN thin films.
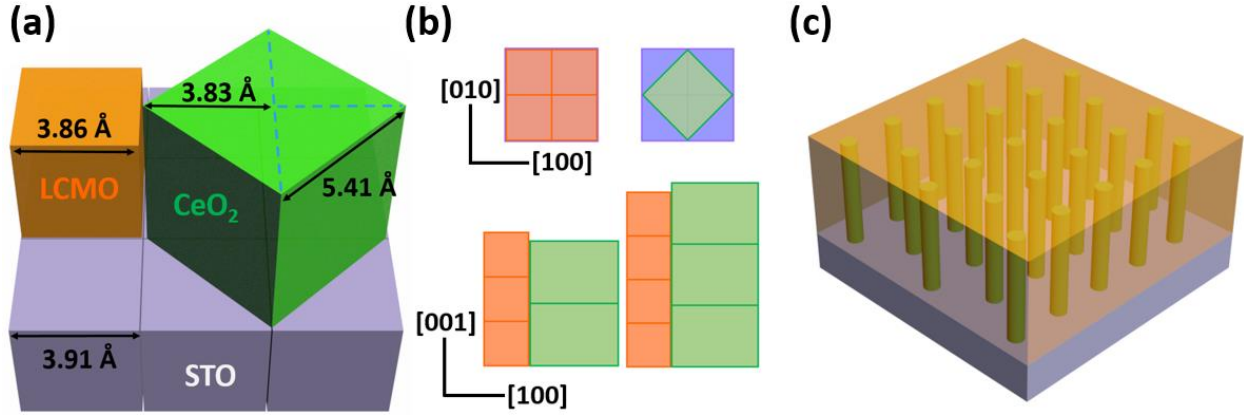
Figure 4.1 (a) 3D schematic drawing of lattice matching relationship of LCMO, CeO$_2$ and STO unit cells. (b) 2D schematic drawing of lattice matching relationship of LCMO and STO (top left); CeO$_2$ and STO (top right); LCMO and CeO$_2$ (bottom). (c) Schematic drawing of LCMO:CeO$_2$ thin films with VAN structure.

4.3   Experimental

LCMO:CeO$_2$ thin films with different molar ratios of 9.5:0.5, 9:1 and 8:2 were deposited onto single-crystal STO (001) substrates via pulsed laser deposition (PLD). The composite targets with different LCMO: CeO$_2$ ratios were prepared by the conventional ceramic sintering process. A KrF excimer laser (λ = 248 nm) with a deposition frequency of 2 Hz was used and the target-substrate distance was kept at 5 cm. During the deposition, the substrate temperature was kept at 750 ^{o}C and an oxygen pressure of 200 mTorr was maintained. After the deposition, the films were cooled down to room temperature in 200 Torr oxygen with a cooling rate of 10 ^{o}C/min. The microstructure of as-deposited films were examined by X-ray diffraction (XRD, PANalytical Empyrean) and transmission electron microscope (TEM, FEI TALOS, F200X). Magnetotransport properties were obtained along the IP direction using the four point probe configuration in the electrical transport option (ETO) of a commercial Physical Properties Measurement System (PPMS, Quantum Design DynaCool) with a magnetic field applied out-of-plane (OP). A 100 nm thick Au thin film was deposited as the electrical contact. The magnetic property was examined

using a Magnetic Property Measurement System (MPMS, Quantum Design MPMS-3) with the magnetic field applied along both IP and OP directions.

4.4   Results and discussion

The microstructure and growth quality of the as-deposited LCMO:CeO$_2$ thin films were first characterized using XRD. Figure 4.2 (a) shows the XRD θ-2θ pattern of the pure LCMO thin film and LCMO:CeO$_2$ films with the composition of 9.5:0.5, 9:1 and 8:2, respectively. It can be seen that both LCMO and CeO$_2$ phases have grown along the (00l) directions without any detectable impurity peaks, suggesting the highly (00l) textured growth. More localized XRD scans near CeO$_2$ (002) and LCMO (002) peaks were shown in Figure 4.2 (b), where the green and orange solid lines indicate the (002) peak shift of the bulk CeO$_2$ and LCMO, respectively. It is obvious that, in the nanocomposite thin films, the CeO$_2$ (002) peaks have been shifted to the left comparing with the bulk counterpart, indicating the increase of the lattice parameter (c_{CeO2}) and the existence of tensile strain in the CeO$_2$ phase OP. On the contrary, the right shift of the LCMO (002) peaks demonstrates the decrease of the OP lattice parameter (c_{LCMO}) and the OP compressive strain in the LCMO phase. The compressive strain in the pure LCMO film is caused by the lattice mismatch between the film and substrate that generates the IP tensile strain and OP compressive strain. From the previous discussion, the different domain matching modes of LCMO and CeO$_2$ in the nanocomposites result in two opposite strain states (-6.5% and 5.1% in LCMO and opposite sign for CeO$_2$). Therefore, the overall compressive (tensile) strain in LCMO (CeO$_2$) phase might be a result of the competition between these two domain matching modes along the OP direction and the substrate induced strain in the IP direction. As the CeO$_2$ composition increases, the left shift of LCMO and CeO$_2$ (002) peaks in LCMO:CeO$_2$ thin films indicates there is less compressive strain inside the LCMO phase (calculated and shown in Figure 4.2 (d)) and more tensile strain inside the CeO$_2$ phase. The peak shift of the CeO$_2$ is less than LCMO, which might be a result of the compensation of the phase induced strain (tensile OP) and substrate induced strain (compressive OP). The localized XRD θ-2θ patterns of other peaks are shown in Figure 4.3. In order to verify the IP lattice matching relationship of the LCMO and CeO$_2$ lattices with the substrate, a ϕ scan of the LCMO:CeO$_2$ film with 8:2 composition was conducted and shown in Figure 4.2 (c). From this result, it can be seen that the LCMO has a cube-on-cube growth on STO substrate while the CeO$_2$ has a 45° IP rotation.

This result is consistent with the predicted epitaxy matching relationship illustrated in Figure 4.1 (a).
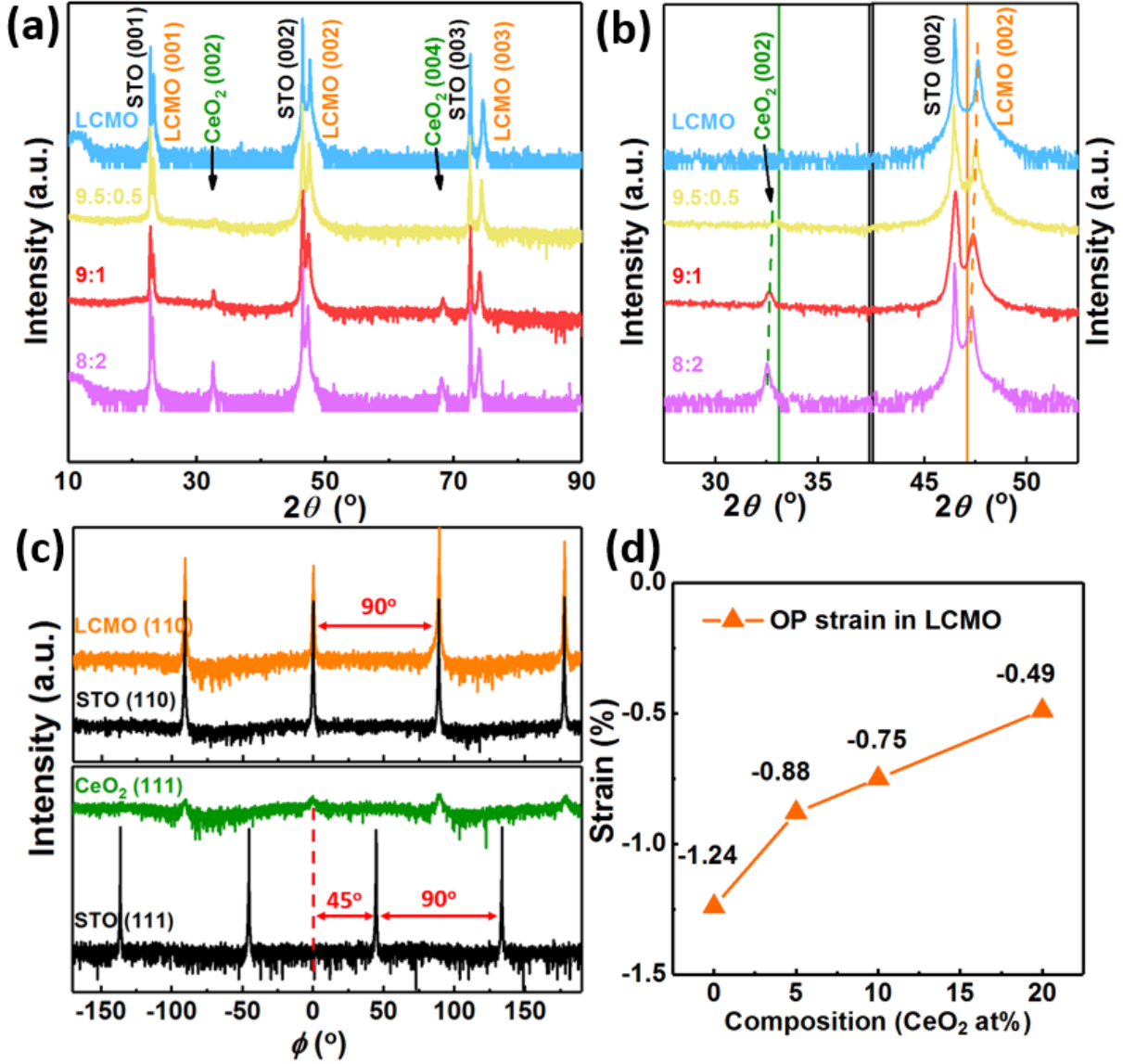
Figure 4.2 (a) θ-2θ XRD scans and (b) local scans of LCMO (002) and CeO$_2$ (002) of LCMO:CeO$_2$ VAN films with different film compositions. The green and orange solid lines indicate the relative peak positions of the bulk material. (c) ϕ XRD scan of LCMO:CeO$_2$ film with 8:2 composition. (d) Calculated out-of-plane strain in LCMO phases of LCMO:CeO$_2$ films with various compositions.
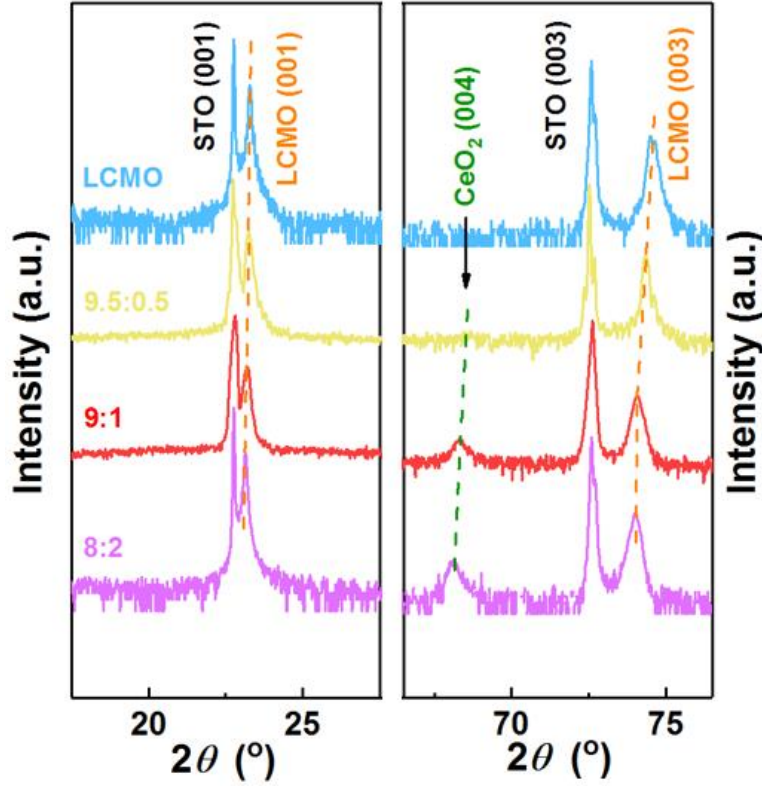
Figure 4.3 Local θ-2θ XRD scans of LCMO:CeO$_2$ VAN films with different film compositions.

In order to characterize the microstructure of LCMO:CeO$_2$ thin films in detail, TEM and scanning transmission electron microscopy (STEM) studies have been conducted on the samples. Figure 4.4 (a) shows the low magnification cross-sectional TEM image of the sample with the composition of 8:2, which shows the perfect pillar structure and high epitaxial quality of the LCMO:CeO$_2$ thin films. The inset of Figure 4.4 (a) shows the selected area electron diffraction (SAED) pattern of the same sample. The orientation relationship of the phases and the substrate can be determined as: $(002)_{LCMO}//(002)_{CeO2}//(002)_{STO}$ and $[020]_{LCMO}//[220]_{CeO2}//[020]_{STO}$. This is consistent with the result shown in Figure 4.2 (c) and again confirms the 45° IP rotation of CeO$_2$ phase. Figure 4.4 (b) shows the cross-sectional STEM image of the sample taken under the high-angle annular dark-field mode, where clear vertical columns of the LCMO and CeO$_2$ phases can be seen. An enlarged STEM image of a selected area is shown on the left side of Figure 4.4 (c) where the LCMO and CeO$_2$ phases are marked as L and C, respectively. The LCMO columns show dark contrast because LCMO has a lower average Z number than that of CeO$_2$, which shows much brighter contrast. From the image, a clear phase boundary along the vertical direction can be

seen. The right section of Figure 4.4 (b) shows the fast-Fourier transform (FFT) filtered image of the same area that demonstrate the domain matching relationship between the LCMO and CeO_2 phases. The alternating 3L-2C and 4L-3C domain matching relationships result in an overall 7L-5C match along the vertical direction, which significantly reduces the residual strain in the columns, as predicted in the earlier part of this paper. Figure 4.4 (d) and Figure 4.4 (e) show the energy-dispersive X-ray spectra (EDS) mapping where the obvious separation of Mn (marked as orange) and Ce (marked as green) elements can be seen, indicating the clear separation of LCMO and CeO_2 phases. Plan-view EDS mappings in Figure 4.4 (f-i) show an obvious pillar (CeO_2, marked as green) in matrix (LCMO, marked as orange) structure. It is noted that comparing with the cross-sectional EDS mapping, clear phase boundaries can be observed in the plan-view images and thus a better phase ratio can be resolved based on these images. This difference might be due to the overlapping of thin (around 5 nm) CeO_2 pillars along the cross-sectional direction. The plan-view EDS mappings of the LCMO-CeO_2 thin films with different compositions have been compared in Figure 4.5, where it can be seen that all the thin films have distinct pillars in matrix structures. As the ratio of CeO_2 increases, an obvious increase of the pillar dimension and density can be noticed, which proves the effectiveness of the microstructure tuning of the LCMO-CeO_2 thin films via film composition control.
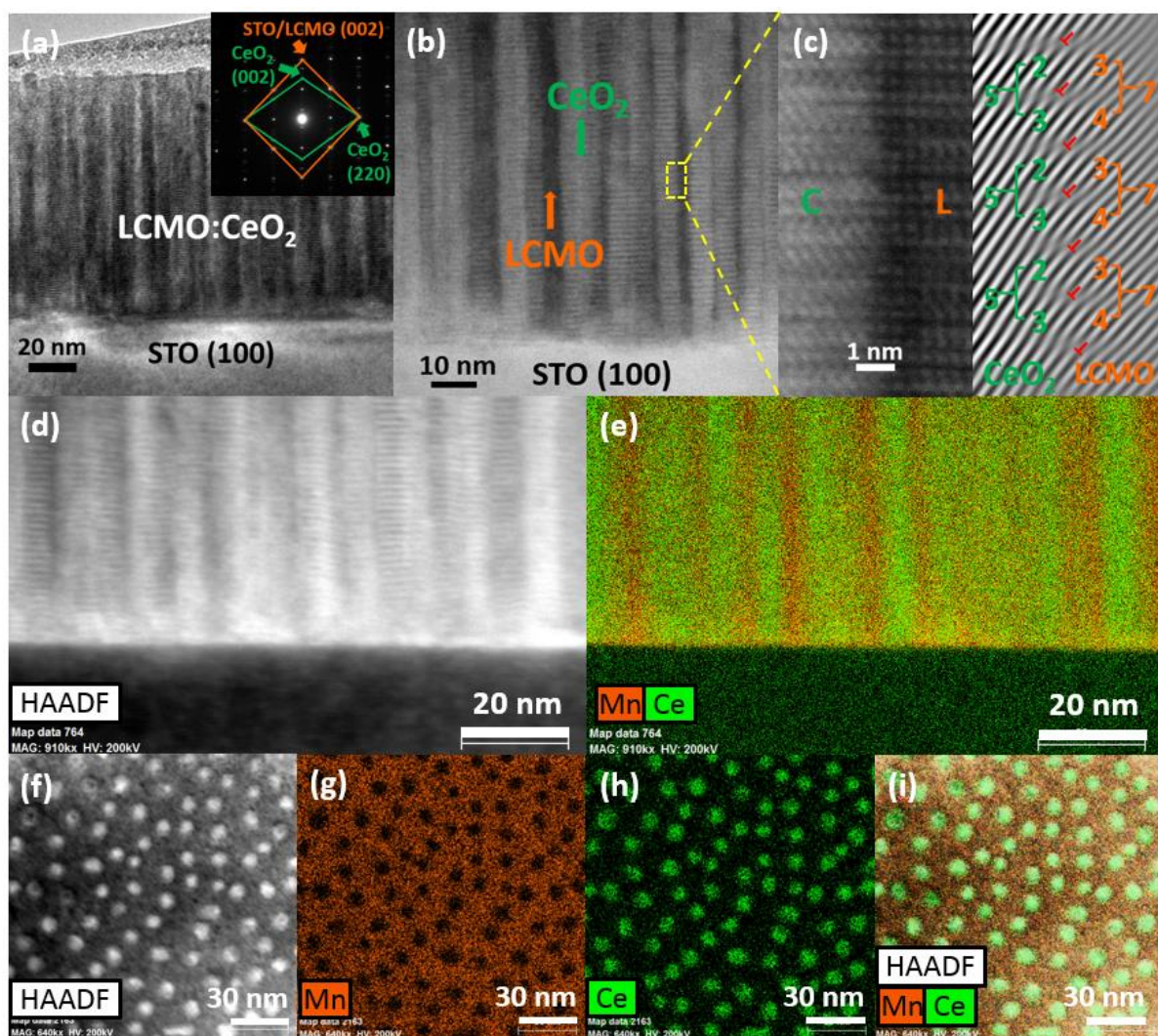
Figure 4.4 (a) Cross-sectional TEM images of LCMO:CeO$_2$ film with 8:2 composition. The inset shows the corresponding selected area electron diffraction (SAED) pattern. (b) STEM image of LCMO:CeO$_2$ film with 8:2 composition. (c) HRTEM image and fast-Fourier transform (FFT) filtered image of LCMO:CeO$_2$ film with 8:2 composition. (d-e) Cross-sectional energy-dispersive X-ray spectra (EDS) mapping of Mn (orange) and Ce (green) of LCMO:CeO$_2$ film with 8:2 composition. (f-i) Plan-view EDS mapping of Mn (orange) and Ce (green) of LCMO:CeO$_2$ film with 8:2 composition.
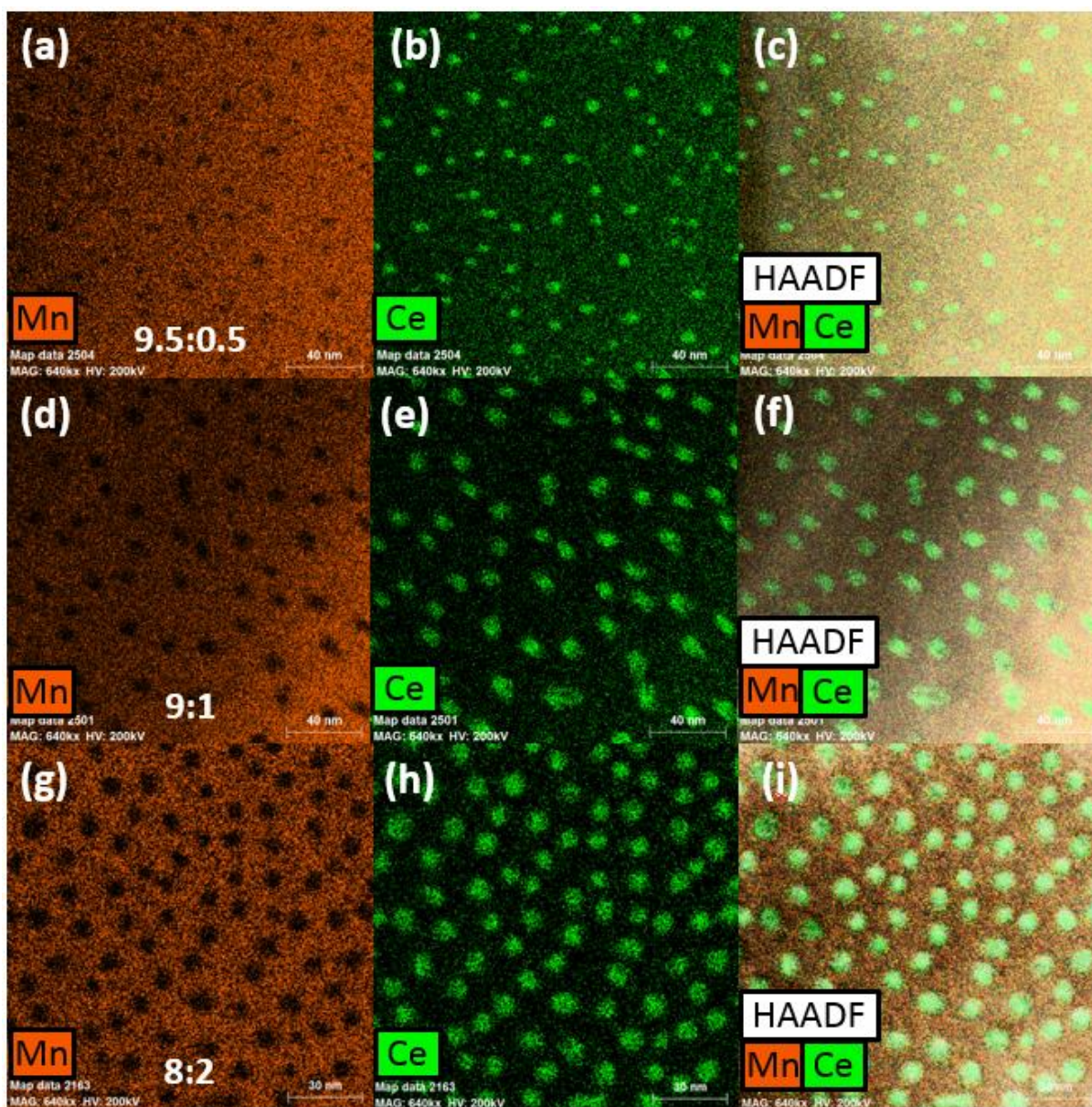
Figure 4.5 Comparison of the plan-view EDS mappings of LCMO:CeO$_2$ films with 9.5:0.5 (a-c), 9:1 (d-f) and 8:2 (g-i) compositions. Mn and Ce atoms are marked in orange and green, respectively. The electron beam of 9:1 sample was slightly tilted, thus the actual size of the pillars should be smaller than the size shown in the figure.

The magnetotransport properties of the films with different compositions were investigated by the PPMS. Figure 4.6 (a-d) show the normalized resistivity vs. temperature curves of different compositional (pure LCMO, 9.5:0.5, 9:1 and 8:2) LCMO:CeO$_2$ thin films with and without a 1 T magnetic field applied OP during the cooling process. Overall, all the RT curves with and without magnetic field show a typical metal-insulator transition, i.e., first an increase in resistivity (metallic behavior) and then a drop in resistivity (insulator behavior), with the T$_{MI}$ ranging from 100K to 240K for different samples. It is obvious that the film resistivity decreases when the magnetic field of 1 T is applied, indicating the existence of LFMR property in all the LCMO:CeO$_2$ VAN thin films. The MR value is calculated from the following equation: MR (%) = [(ρ_0-ρ_H)/ρ_0] x 100%, where ρ_0 and ρ_H are the resistivity of the films without and with the applied magnetic field. Figure 4.6 (e) shows the calculated maximum MR% (Max MR) of the films with different CeO$_2$ atomic percentages. It can be seen that the Max MR of LCMO:CeO$_2$ thin films is enhanced comparing with the pure LCMO (31%) and increases from 38.8% to 51.8% when the CeO$_2$ atomic ratio increases from 5% to 20%. This enhancement of the Max MR can be explained by two mechanisms. First, the insulating CeO$_2$ phases generate the magnetic disordered phase boundary and serve as the energy barrier, which enhance the spin-fluctuation suppression effect and cause the enhanced LFMR in the LCMO phase. Denser and wider CeO$_2$ pillars found in the LCMO-CeO$_2$ thin films with higher CeO$_2$ ratios generate higher amount of phase boundaries and higher energy barrier, thus enhances the spin-fluctuation suppression effect and leading to better LFMR properties in the films.[40] Second, the insulating CeO$_2$ phase can decrease the magnetic inhomogeneity close to grain boundary and has an effect on the tunneling process of the electrons, which can enhance the LFMR in thin films.[115] This tunneling effect is enhanced as the composition of CeO$_2$ increases. The result demonstrates that the LFMR property of LCMO can be enhanced by the introduction of an insulating second phase and can be tuned by controlling the amount of the secondary phase. More interestingly, obvious tuning of the T$_{MI}$ as a function of the CeO$_2$ composition has been observed in this work. Figure 4.6 (f) shows the plot of T$_{MI}$ vs. the CeO$_2$ composition. Similar to the trend of Max MR, the T$_{MI}$ of the two-phase systems are higher than the single-phase LCMO (113 K and 110 K) and increase from 123 K and 113 K in the 9.5:0.5 film to 210 K and 223 K in the 8:2 film, under zero field and applied field, respectively. It has been reported in the LSMO films that the T$_{MI}$ decreases as the strain in the film increases.[126] Therefore, the increasing transition temperature in the LCMO:CeO$_2$ films along with the increasing CeO$_2$ percentage might be a result of the

decreased compressive strain in LCMO phase, as discussed previously in the XRD results. It is interesting to note that the major tuning in the magnetotransport properties of the LCMO:CeO$_2$ films was based on a very small amount of CeO$_2$ secondary phase introduced, suggesting the effectiveness of VAN approach in transport property tuning.
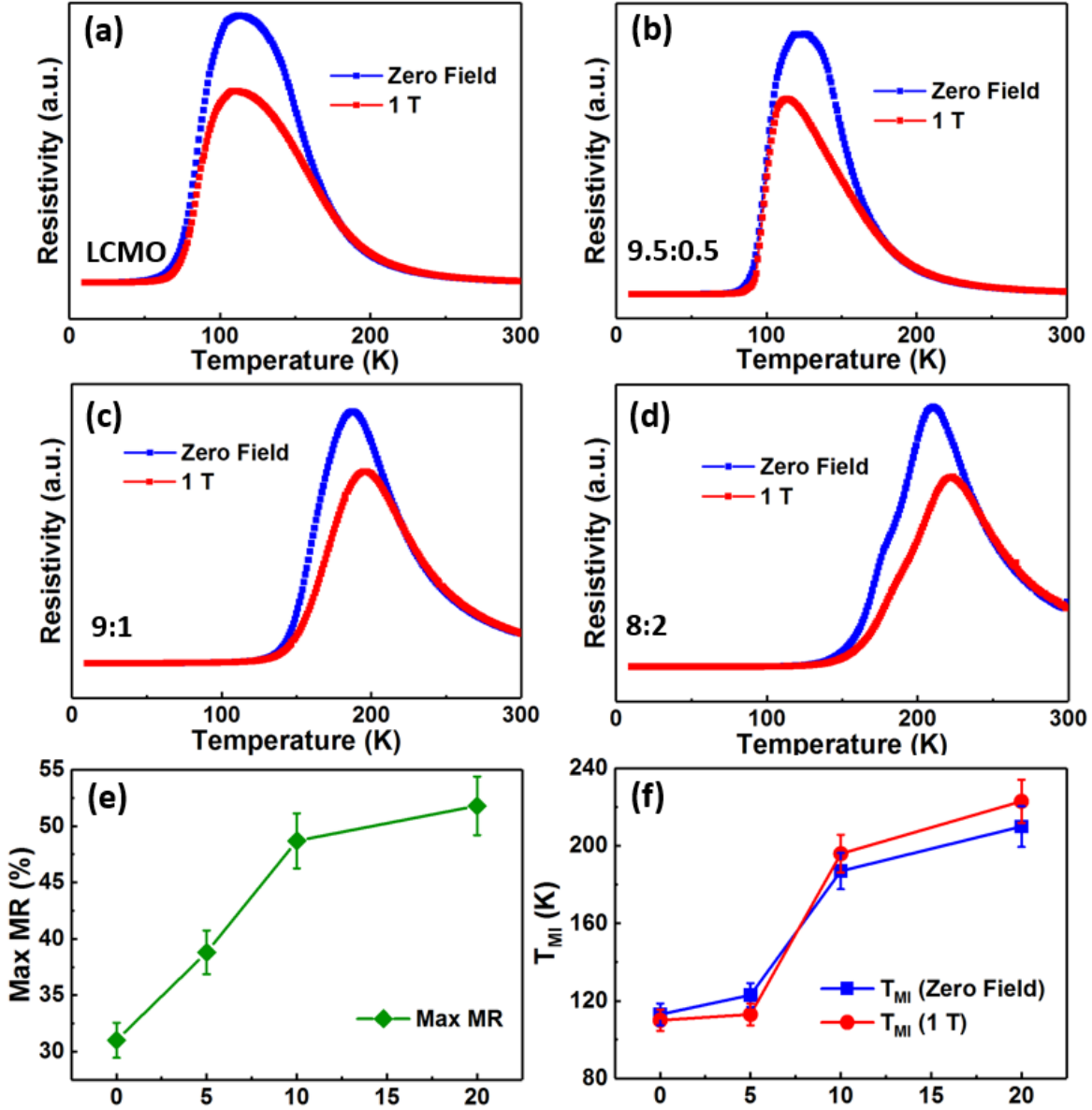
Figure 4.6 (a-d) Normalized resistivity versus temperature curves of pure LCMO films and LCMO:CeO$_2$ films with 9.5:0.5, 9:1 and 8:2 compositions, respectively. (e) Maximum MR of LCMO:CeO$_2$ films with various compositions. (f) Metal-insulator transition temperature (T$_{MI}$) of LCMO:CeO$_2$ films with various compositions.

The magnetic property of the LCMO:CeO$_2$ thin films was investigated by the MPMS measurements. Figure 4.7 (a) shows the magnetization vs. magnetic field hysteresis (M-H) loops of the 8:2 film measured at 10 K, while the magnetic field was applied in both IP and OP directions. The inserted schematic drawing in Figure 4.7 (a) illustrates the direction of the applied magnetic field. The result demonstrates an obvious ferromagnetic response of the LCMO:CeO$_2$ (8:2) film along both IP and OP directions. Besides, the large difference of the magnetic moment intensity in the IP and OP directions indicates the strong anisotropic magnetic property of the film. In LCMO lattices, ferromagnetic Mn-O and non-magnetic La-O layers in a-b plane are aligned alternatively, which leads to the overall ferromagnetic property in IP direction while the c-plane shows anti-ferromagnetic response.[127,128] Ferromagnetism in both directions and the IP anisotropy has been discovered in strained LCMO thin films on STO substrates, previously.[129,130] Such highly anisotropic magnetic properties can be explained by the anisotropic strain state in VAN thin films. Other VAN systems with anisotropic property along the IP and OP directions have been reported previously.[131] Similar anisotropic magnetic property in the LCMO:CeO$_2$ VAN films at room temperature has been obtained and shown in Figure 4.8. Figure 4.7 (b) shows the comparison of the IP MH hysteresis loops of the films with different compositions at 10 K and the inset shows enlarged loops to better show the difference. An obvious enhancement of the saturation magnetization (M$_s$) and remanent magnetization (M$_r$) can be observed in the LCMO:CeO$_2$ VAN thin films comparing to the pure LCMO thin film. It has been reported that the magnetic easy axis in LCMO thin films can be tuned by the direction of the tensile strain.[130] The enhanced IP ferromagnetic property in the LCMO:CeO$_2$ thin films might be attributed to the IP tensile strain generated in 3L-2C domains. The magnetic properties in different LCMO:CeO$_2$ thin films are close to each other, which proves that the variation of the CeO$_2$ composition have less effect on the overall magnetic properties comparing to its strong impacts on the electrical transport properties. This phenomenon might be a result of the compensation between the increasing IP tensile strain generated by 3L-2C domains, which enhances the IP magnetic property, and the increasing non-magnetic CeO$_2$ percentage, which degrades the magnetic property of the thin films.
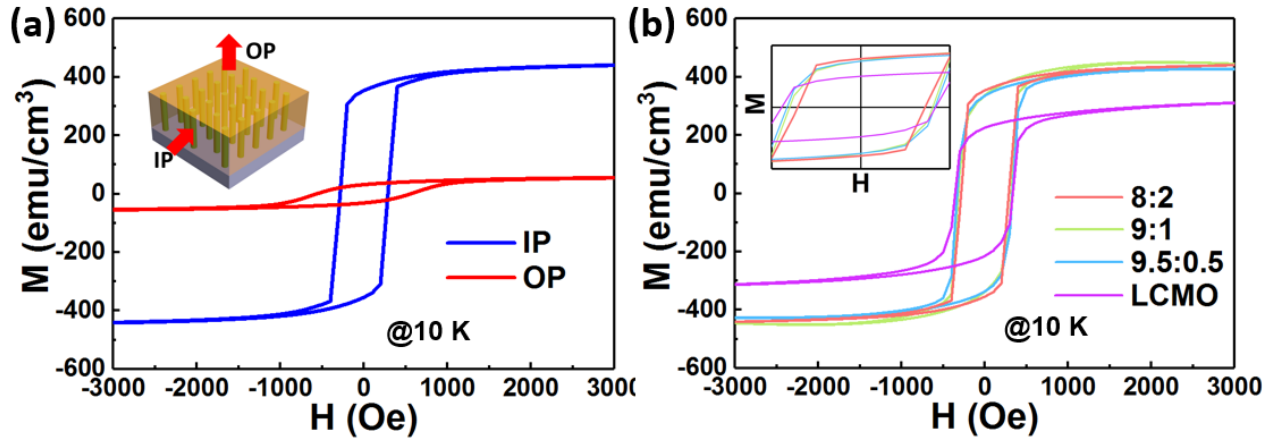
Figure 4.7 (a) Magnetic hysteresis loops with magnetic field applied in ip-plane and out-of-plane directions of LCMO:CeO$_2$ film with 8:2 composition, measured at 10 K. The insets shows the corresponding magnetic field direction. (b) In-plane magnetic hysteresis loops of LCMO:CeO$_2$ films with various compositions measured at 10 K. The inset shows an enlarged plot close to the original point.
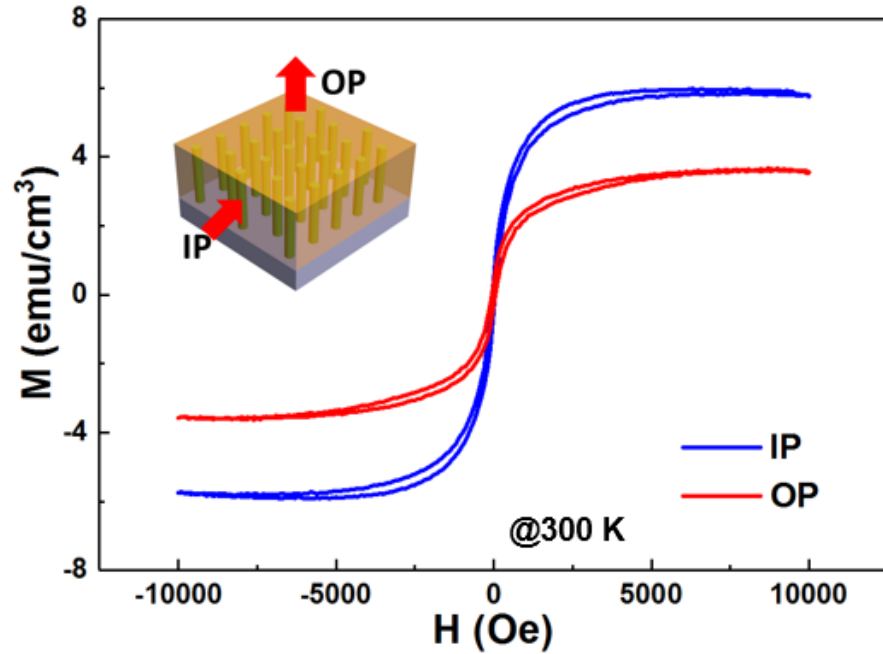
Figure 4.8 Magnetic hysteresis loops with magnetic field applied in ip-plane and out-of-plane directions of LCMO:CeO$_2$ film with 8:2 composition, measured at room temperature. The insets shows the corresponding magnetic field direction.

Overall, by incorporating the CeO_2 phase into the LCMO, disordered phase boundaries and the strain along the OP direction are introduced. The introduction of the phase boundaries enhances the spin-fluctuation suppression effect and the insulating CeO_2 phase generates effective tunneling to the electrical transport properties, which subsequently enhance the LFMR properties in the films. By increasing the percentage of the CeO_2 within in the VAN films, the Max MR can be enhanced and the T_{MI} temperature can be effectively tuned. The strain generated by the lattice mismatch between the two phases could be responsible for the tuning of the T_{MI} and the enhancement of the ferromagnetic property. A comparable tuning effect of the MR and T_{MI} with less change of the secondary phase percentage ($x_{max} = 0.55$ vs. $x_{max} = 0.2$ in this work) can be achieved in this study, comparing with the previous work on $LSMO:CeO_2$ VAN system,[40] which demonstrates the effectiveness of composition tuning in $LCMO:CeO_2$ system. Further investigation by higher composition of the CeO_2 phase and varying other growth parameters (deposition frequency, oxygen pressure and substrate) could be important for this VAN system. This work demonstrates the capability of exploring LFMR in the LCMO-based VAN systems, which could broaden the VAN family for tuning magnetotransport properties.

4.5 Conclusions

As a conclusion, heteroepitaxial $LCMO:CeO_2$ thin films with VAN structure have been grown on STO (001) substrates by PLD. The enhanced LFMR property of the thin films is achieved by introducing the insulating CeO_2 phase, which acts as the source of the disordered grain boundaries and the tunneling effect. The LFMR property can be enhanced and the T_{MI} is effectively tuned when increasing the amount of the CeO_2 phase in the films. Anisotropic ferromagnetic property is achieved and the M_r and M_s are enhanced due to the strain in the LCMO phase. This work suggests the VAN structure is a promising approach in tuning magnetotransport and magnetic properties of manganite oxides.

5. NOVEL LAYERED BI3MOMTO9 (MT = MN, FE, CO AND NI) THIN FILMS WITH TUNABLE MULTIFUNCTIONALITIES

5.1 Overview

$Bi_3MoM_TO_9$ (BMoM$_T$O; M$_T$, transition metals of Mn, Fe, Co and Ni) thin films with a layered supercell structure have been deposited on LaAlO$_3$ (001) substrates by pulsed laser deposition. Microstructural analysis suggests that the pillar-like domains with higher transition metal concentration (e.g., Mn, Fe, Co and Ni) are embedded in the Mo-rich matrix with layered supercell structures. The layered supercell structure of the BMoM$_T$O thin films is accounted for the anisotropic multifunctionalities such as the magnetic easy axis along the in-plane direction, and the anisotropic optical properties. Ferroelectricity and ferromagnetism have been demonstrated in the thin films under room temperature, which confirms the multiferroic nature of the system. By varying the transition metal M$_T$ in the film, the band gaps of the BMoM$_T$O films can be effectively tuned from 2.44 eV to 2.82 eV, while the out-of-plane dielectric constant of the thin films also varies. The newly discovered layered nanocomposite systems presents their potentials in ferroelectrics, multiferroics and non-linear optics.

5.2 Introduction

Aurivillius phases, in perovskite-related structures with the formula of $Bi_2A_{n-1}B_nO_{3n+3}$ (A = Ca, Sr, Ba, Pb, Bi, Na, K, B = Ti, Nb, Ta, Mo, W, Fe),[132,133] have sparked significant research interests due to their potential applications in piezoelectric devices,[134–136] superconductors,[137–139] thermoelectric generators,[140,141] photocatalysts,[142,143] etc. In an Aurivillius lattice, n perovskite-like $(Bi_2A_{n-1}B_{3n+1})^{2-}$ layers and one bismuth-oxygen $(Bi_2O_2)^{2+}$ layer are stacked alternatively,[144] which generates an unique layered structure and promising properties. Due to the structural differences along the crystallographical orientations that are either parallel or perpendicular to the $(Bi_2O_2)^{2+}$ layers, anisotropic properties have been reported in many Aurivillius systems. For example, anisotropic optical property has been reported in the Bi_2AlMnO_6 supercell (SC) thin film;[145] anisotropic ionic conductivity has been demonstrated in $Bi_4V_{2-x}Co_xO_{11-\delta}$ single crystal;[146] and anisotropic dielectric constant has been observed in $BaBi_2Nb_2O_9$ system.[147] Besides, the Aurivillius phase has shown low leakage[148,149] and fatigue free[150,151] ferroelectric proFperties at

the room temperature, which brings it potential applications in ferroelectric random access memories (FRAMs).[152]

Over the past few decades, considerable attention has been attracted on exploring multiferroic materials. Multiferroics are materials that simultaneously possess more than one ferroic characteristics (i.e. ferroelectricity, ferromagnetism and ferroelasticity),[72,153] which can be used in sensors, data storage, high-temperature electronics and memory devices.[71,154,155] The perovskite-type oxides with the formula of AM_TO_3 (A = Bi, P_b; M_T = transition metal ion) have been demonstrated as the candidates for the single phase multiferroic materials.[156] For example, $BiMnO_3$ has been reported as a multiferroic material which has the coexisting ferromagnetic and ferroelectric responses.[157,158] Beside of the single phase multiferroic materials, multiphase materials which combine different ferroic orders into one system have been well studied to artificially generate multiferroic property.[131,159,160] Despite the tremendous efforts that have been spent on exploring new systems, single phase multiferroic materials are still rare in nature.

In this work, the layered Aurivillius phase Bi_2MoO_6 (BMoO) has been incorporated with the perovskite-type transition metal oxides BiM_TO_3 (BM_TO, M_T = Mn, Fe, Co and Ni) to form a new multiferroic nanocomposite system. BMoO is a ferroelectric material with a high Curie temperature (570 ^oC),[161] while BM_TO is a multiferroic system as mentioned above. Interestingly, by combining BMoO and BM_TO, a new nanocomposite material system ($Bi_3MoM_TO_9$, or $BMoM_TO$ as the abbreviation) has been created. Layered SC structure, which is similar to the Aurivillius phase, has been observed in this new material system. Meanwhile, pillar-like domains have been generated inside the thin films. Figure 5.1 (a) shows the 3D schematic drawing of the $BMoM_TO$ thin films, illustrating the pillar like domains embedded in layered matrix structure. Besides, the $BMoM_TO$ thin films have exhibited tunable multifunctionalities, including room-temperature multiferroic properties (i.e. ferroelectricity and ferromagnetism) and optical properties (band gap and dielectric constant). These functionalities are anisotropic due to the layered structure and can be effectively tuned by changing the category of transition metal in the system.

5.3   Experimental

The $BMoM_TO$ targets as well as a pure BMoO target were prepared by conventional solid-state sintering methods. The thin films were deposited onto single crystal $LaAlO_3$ (LAO) (001)

substrates using pulsed laser deposition (PLD, KrF, λ = 248 nm) with an optimized substrate temperature of 600 $^{\circ}$C and oxygen pressure of 200 mTorr during the thin film growth. After the deposition, the as-deposited samples were cooled down to 400 $^{\circ}$C with a rate of 5 $^{\circ}$C/min at a 500 Torr oxygen atmosphere and subsequently annealed for one hour to reduce the oxygen vacancies. $SrRuO_3$ (SRO) buffer layers were firstly deposited onto the substrates as bottom electrodes for ferroelectric measurements. The microstructure of fabricated thin films were investigated by X-ray diffraction (XRD, PANalytical Empyrean) and transmittance electron microscopy (TEM, Thermo Scientific TALOS F200X and Thermo Scientific TEAM 1). The piezoelectric properties were measured by the atomic force microscopy (AFM, Bruker Dimension Icon) and piezoresponse force microscopy (PFM) with a conductive Pt-Ir coated Si tip (SCM-PIT). The magnetic properties were investigated using a magnetic property measurement system (MPMS, Quantum Design MPMS-3) with the magnetic field applied in both in-plane (IP) and out-of-plane (OP) directions. The normal incident depolarized transmittance (T%) of the films were carried using an optical spectrophotometer (Lambda 1050 UV/Vis Spectrophotometer) with a spectrum range of 250-800 nm and incident angle of 15°, 30°, 45°, 60° and 75°, respectively. The direct band gaps were estimated by the Tauc method from the transmittance result obtained at 15°. The ellipsometry experiments were examined on a RC2 spectroscopic ellipsometer (J.A. Woollam Company) with a spectrum range of 1000-2000 nm and three angles of 50°, 60° and 70°. The real dielectric constants of the thin films were then retrieved from the software (CompleteEase, J.A. Woollam Company) using the Spline or Gen-Osc model.

5.4   Results and discussion

XRD analysis was first conducted to characterize the microstructure and growth quality of the thin films. Figure 5.1 (b) shows the normalized θ-2θ XRD pattern of the BMoM$_T$O thin films and pure BMoO thin film. From the XRD patterns, periodic (00l)-type diffraction peaks can be observed, indicating the high quality SC structure of the thin films with the preferential growth along OP direction. Corresponding OP d-spacing of the thin films can be calculated by Bragg's law, while all the films have the similar lattice parameters of around 8.1 Å. This result is predictable from the XRD patterns, where there is no obvious film peak shift for different films, indicating the similar SC structures in BMoM$_T$O and BMoO thin films. The pure BMoO thin film has sharper peaks with a smaller full width at half maximum (FWHM), indicating higher

96

crystallinity of the pure film comparing to the thin films. This result might be related to the formation of the domains in the film, which is to be discussed further below.
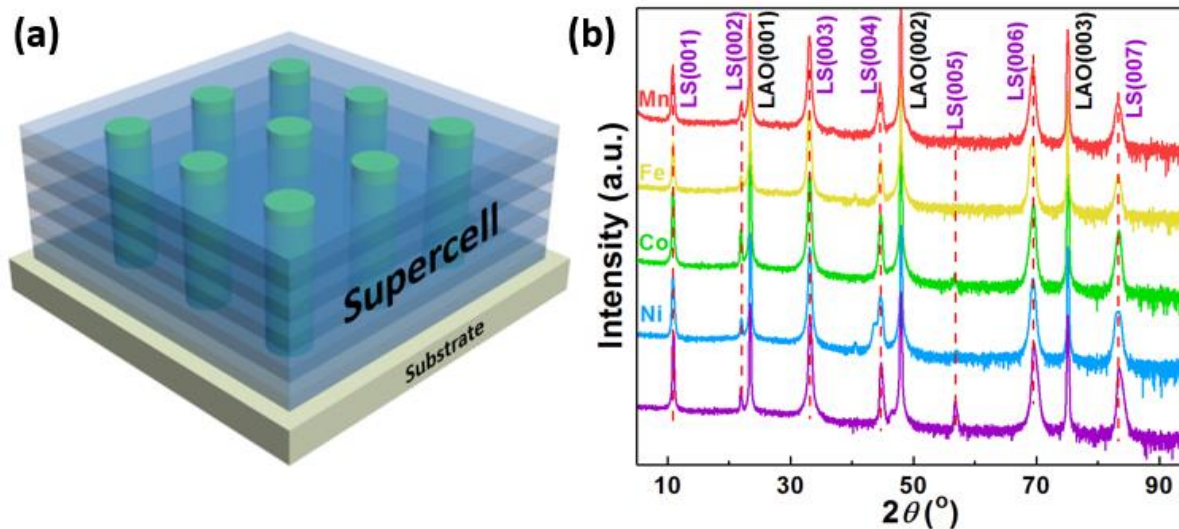
Figure 5.1 (a) 3D schematic drawing of the BMoM$_T$O thin films. (b) θ-2θ XRD scans of BMoM$_T$O and BMoO thin films. The red dashed lines indicate the positions of the (00l) peaks.

To better understand the microstructure of the BMoM$_T$O thin films, cross-sectional TEM was conducted. Figure 5.2 (a) shows the cross-sectional TEM image of the Bi$_3$MoFeO$_9$ (BMoFeO) thin film grown on LAO (001) substrate. Overall, the film shows a layered SC structure with the lattice planes parallel to the substrate, as discussed in the XRD pattern analysis. Besides, it is noted that some bright pillar-like domains are formed in the film. These domains might be formed as a result of the atomic composition variation within the film, i.e., Fe-rich in these "pillars" than the rest part of the film, thus form the nanopillar-like Fe-rich domains. At the meantime, the "matrix" is Mn-rich. As Fe has smaller atomic number than Mo, the Fe-rich regions show brighter contrast in the TEM mode. Figure 5.2 (b) shows the corresponding SAED pattern taken along the [100] zone axis. Distinguished diffraction dots in the SAED pattern indicate the highly epitaxial growth of the BMoFeO SC structure and confirm the (00l) growth direction of the layered thin films. Figure 5.2 (c) shows the STEM image of the BMoFeO film taken under the high angle annular dark field (HAADF) mode of the same area which shows clear SC structure with the same domain structure but with inverted contrast. STEM under HAADF mode is also called Z-contrast and the image contrast is proportional to Z^2. The Fe-rich and Mo-rich domains are marked by the yellow

and purple arrows, respectively. Figure 5.2 (d) shows the HRSTEM image of the sample taken at the domain boundary area, where the black dash line represents the boundary between the Fe-rich domain (dark contrast due to lower atomic number) and Mo-rich domain (brighter contrast due to higher atomic number). It is interesting to note that the horizontal SC layers are continuous throughout the domain boundaries, which proves the domains in the BMoFeO thin film are caused by the compositional differences, instead of crystal structure difference. Figure 5.3 shows the fast-Fourier transform (FFT) filtered image obtained from the selected area in HRSTEM image, where there is no dislocation observed at the grain boundary, which again demonstrates the continuity of the SC structure across the domain boundaries. This observed phenomenon explains why there is no secondary phase peak in the XRD pattern shown in Figure 5.1 (b). Similar results have been observed in the films with other compositions, such as Bi_3MoMnO_9 (BMoMnO), Bi_3MoCoO_9 (BMoCoO) and Bi_3MoNiO_9 (BMoNiO), as shown in Figure 5.4. Figure 5.2 (e) shows the corresponding cross-sectional EDS mapping of the BMoFeO thin film, where the Fe and Mo elements are marked in yellow and purple, respectively. This image shows clear Fe-rich pillar-like domains embedded in the Mo rich matrix. An EDS line scan at the green arrow marked region in Figure 5.2 (f) shows the Fe and Mo distribution, marked in yellow and purple, respectively. Both elements exist in the entire scanned region, while the Fe shows an obvious composition jump in the pillar area, which confirms the Fe-rich pillar area. The atomic fraction of Mo is higher in the Mo-rich matrix area than that in the pillars. This result confirms that the domains in the BMoFeO thin film are formed by the distribution of Fe and Mo atoms. Besides, the dark and bright contrast areas observed in the TEM and STEM images might be due to the local non-uniform elemental distribution and the non-uniformity is minor, which is originated from the TEM sample preparation.
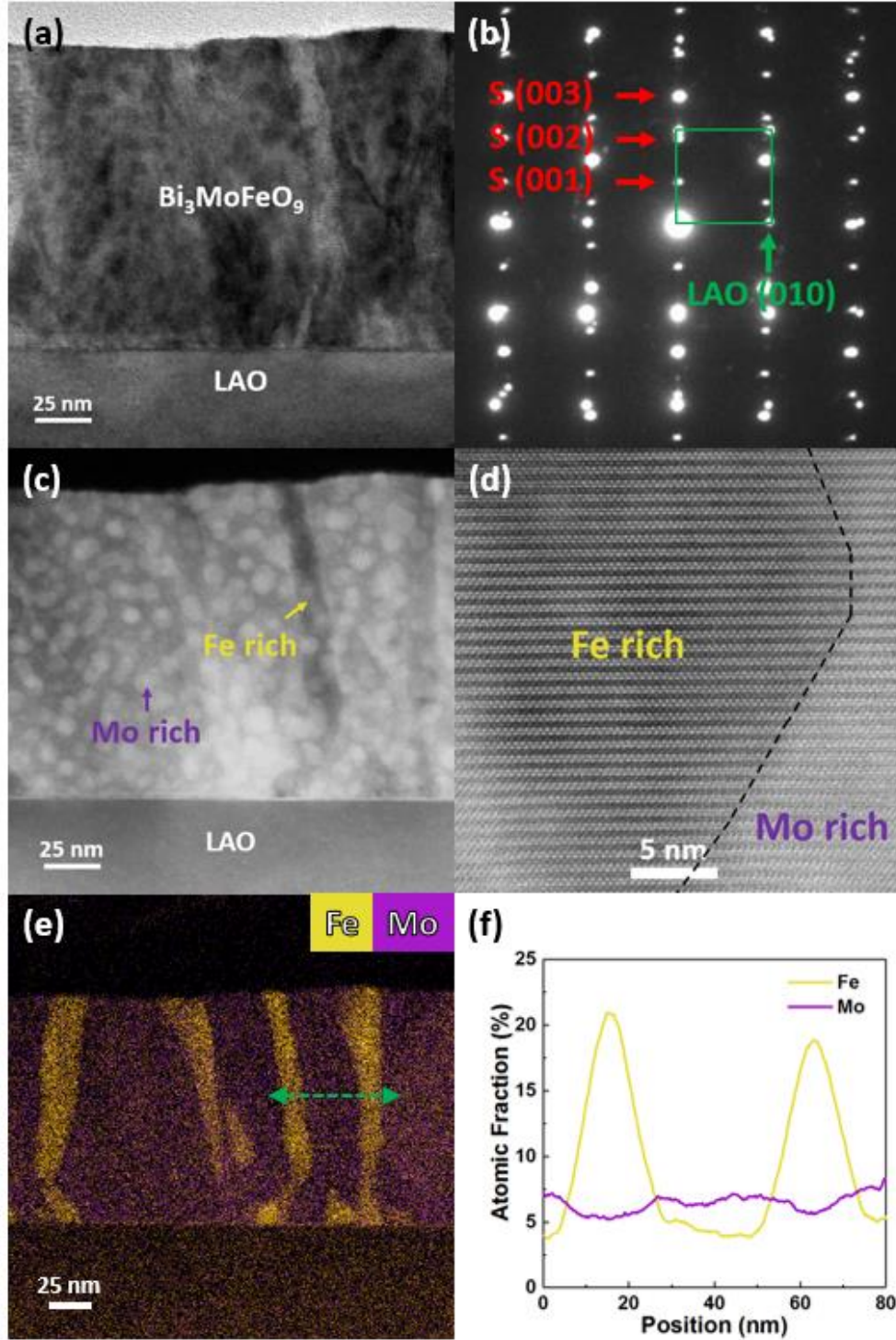
Figure 5.2 (a) Cross-sectional TEM image and (b) Selected area electron diffraction (SAED) pattern and (c) STEM image of the BMoFeO thin film. (d) HRTEM image of the BMoFeO thin film, while the black dashed line indicates the domain boundary. (e) Cross-sectional energy-dispersive X-ray spectra (EDS) mapping of Fe (yellow) and Mo (purple) atoms in the BMoFeO film. The green arrow indicates the selected area for: (f) Smoothed linear EDS analysis of the Fe and Mo atoms.
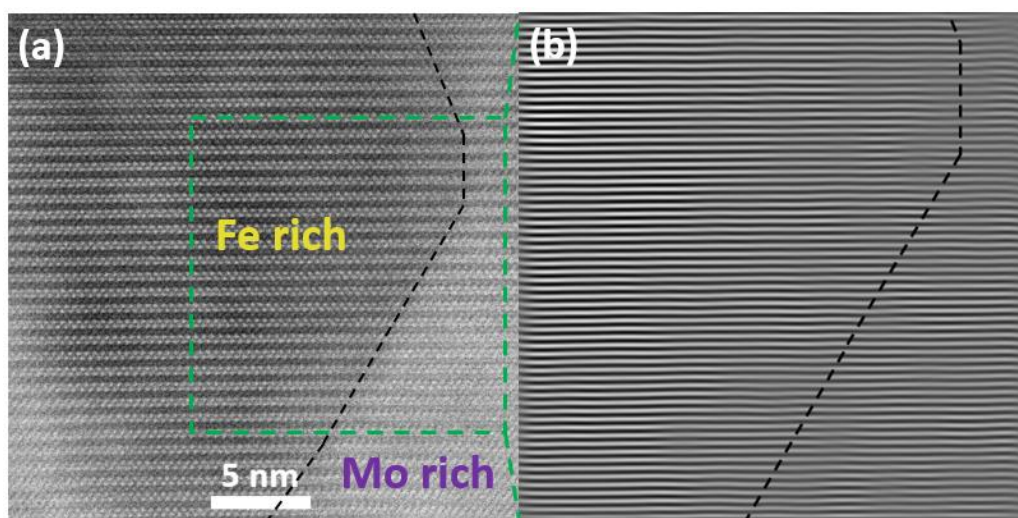
Figure 5.3 (a) HRTEM image of the BMoFeO thin film, while the black dashed line indicates the domain boundary. (b) Fast-Fourier transform (FFT) filtered image of the BMoFeO thin film.
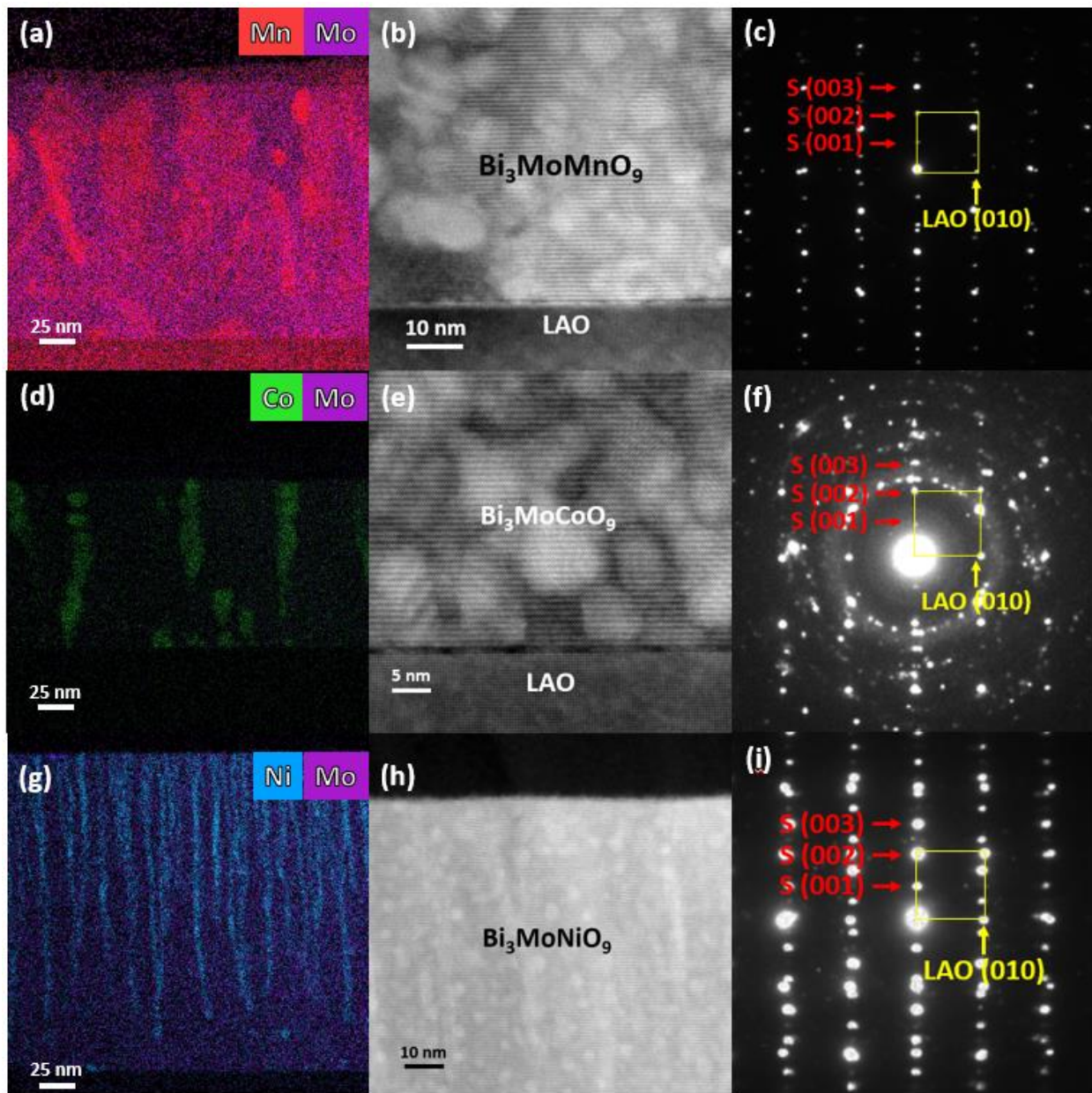
Figure 5.4 Cross-sectional energy-dispersive X-ray spectra (EDS) mappings (left); STEM images (middle); and selected area electron diffraction (SAED) patterns (right) of: (a-c) BiMoMnO (d-f) BiMoCoO and (g-i) BiMoNiO thin films.

PFM measurements were performed to explore the electric properties of the $BMoM_TO$ thin films, as shown in Figure 5.5. SRO buffer layers were grown first as the bottom electrodes. The left panel of each figure show the phase (plotted in blue) and amplitude (plotted in red) switching curves of the $BMoM_TO$ with different M_T elements (Mn, Fe, Co and Ni, respectively). For all four films, the phase curves show obvious hysteresis loops with 180° phase switching when the bias

directions are switched and the amplitude curves show the butterfly-like shape. These curves indicate the ferroelectric nature of the BMoM$_T$O thin films. The right panels of the figures show the OP phase switching images after a writing and re-writing process, where the positive tip biases were first applied on 0.5 x 0.5 μm^2 areas followed by the negative tip biases applied on 0.2 x 0.2 μm^2 areas. After the writing and re-writing processes, distinct phase switching can be observed, which furtherly confirms the ferroelectric properties in all the BMoM$_T$O thin films. All above measurements were conducted at 300 K, demonstrating the room temperature ferroelectric nature of the BMoM$_T$O thin films.
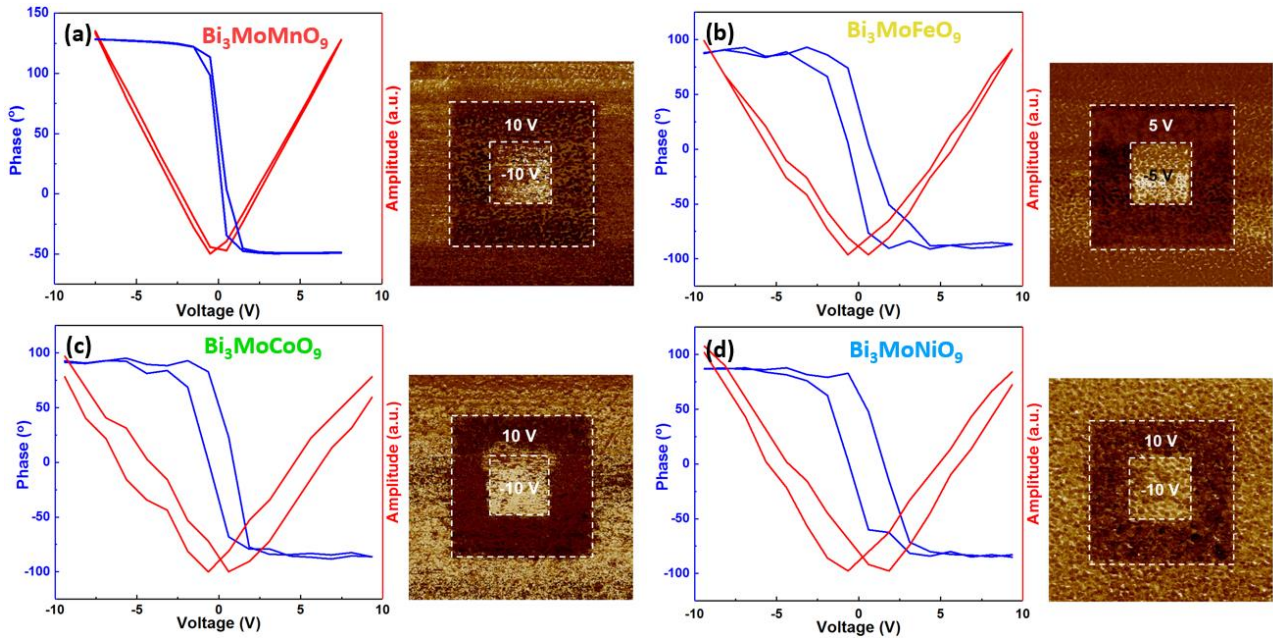
Figure 5.5 (a-d) Left panels: the phase (blue) and amplitude (red) switching curves of the BMoM$_T$O thin films; Right panels: PFM phase image of the BMoM$_T$O films with different elements (Mn, Fe, Co and Ni, respectively).

To explore the magnetic properties of the BMoM$_T$O thin films, ferromagnetic hysteresis loops were obtained using MPMS. Figure 5.6 (a) and (b) show the room temperature M-H curves of the BMoM$_T$O thin films with the magnetic fields applied IP and OP, respectively. The insets of the figures illustrate the directions of the applied fields. As shown in the figures, the BMoM$_T$O thin films show strong ferromagnetic properties at room temperature, in both IP and OP directions. As a comparison, pure BMoO film only shows very weak magnetic response, as plotted in Figure 5.7. The huge enhancement of the magnetic response in the BMoM$_T$O thin films is attributed to

the incorporation of the magnetic elements M_T (e.g., Mn, Fe, Co and Ni). Interestingly, the IP anisotropic magnetic property, i.e., stronger magnetic response in the IP direction, has been observed in most of the BMoM$_T$O thin films, including BMoFeO, BMoMnO and BMoNiO, which is possibly due to the easy IP magnetocrystalline axis for the layered structure, similar to the pure BMoO case. Differently, the BMoCoO sample shows better ferromagnetic response along the OP direction. This might be related to the stronger magnetic response in the Co-rich pillar regions which results in the OP anisotropy. Overall, the coexistence of ferroelectricity and ferromagnesium under room temperature demonstrates the room temperature multiferroic properties of all the BMoM$_T$O thin films.
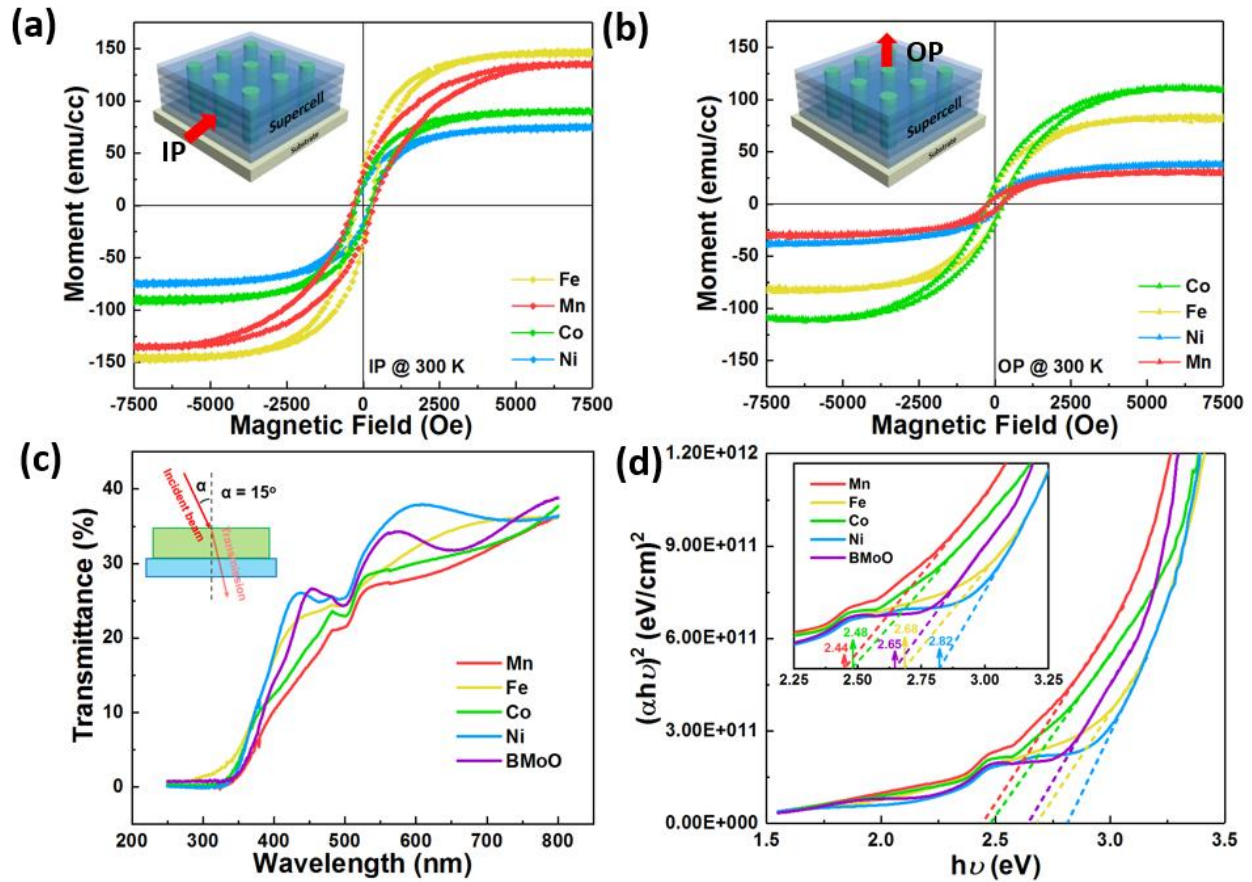
Figure 5.6 (a) In-plane and (b) Out-of-plane magnetic hysteresis loops of BMoM$_T$O films measured at 300 K. The insets show the corresponding magnetic field directions. (c) The optical transmittance spectra of the BMoM$_T$O thin films as a function of the wavelength, with an incident beam angle of 15°. (d) Direct band gaps of the BMoM$_T$O and BMoO thin films with the inset showing the enlarged figure and the values of the band gaps.
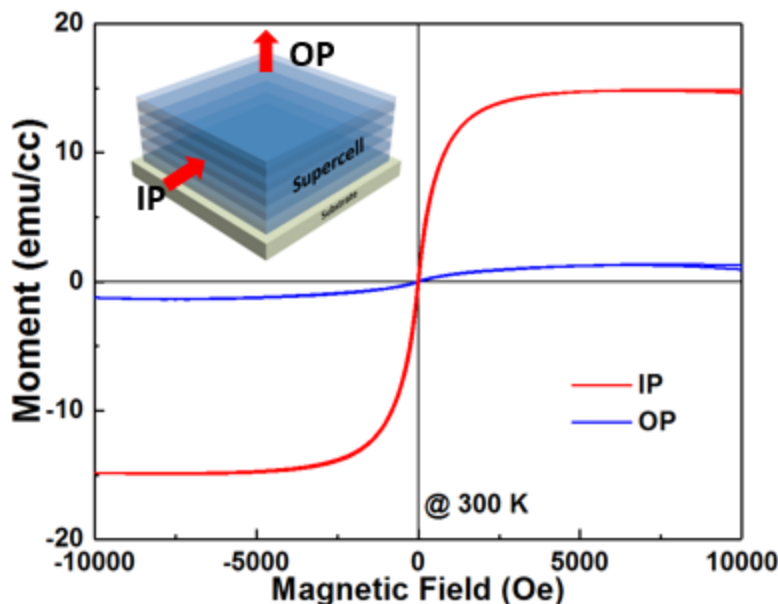
Figure 5.7 Room temperature magnetic hysteresis loops with magnetic field applied in ip-plane and out-of-plane directions of BMoO film. The inset shows the corresponding magnetic field direction.

Tunable optical responses in $BMoM_TO$ thin films are also expected because of the various M_T dopants and the unique nanopillar-in-matrix structures. First, transmittance measurements were conducted. Figure 5.6 (c) shows the optical transmittance spectra of the $BMoM_TO$ thin films as a function of the wavelength. The corresponding direct band gaps of each film were calculated using the Tauc method, and shown in Figure 5.6 (d) with an inset showing the enlarged plot labelling the band gaps of each film. The band gap of the BMoO thin films is estimated to be 2.65 eV, which is comparable to previous reported values.[162–164] By changing magnetic elements M_T in the system, tunable direct band gaps of the $BMoM_TO$ thin films arranging from 2.44 eV to 2.82 eV were obtained for Mn, Co, pure, Fe, and Ni. This tuning result might be attributed to the minor structural change based on the ionic size reduction of M_T ions in the lattice, as well as the shape, size and density of the pillar domains. The angular dependence of the transmittance spectra has been studied and is shown in Figure 5.8. It can be observed that the on-set points (marked by the arrows) shift to the left as the incident beam angle increases. The shift of the on-set points versus the incident beam angles suggest the anisotropic nature of the optical properties in the $BMoM_TO$ thin films.
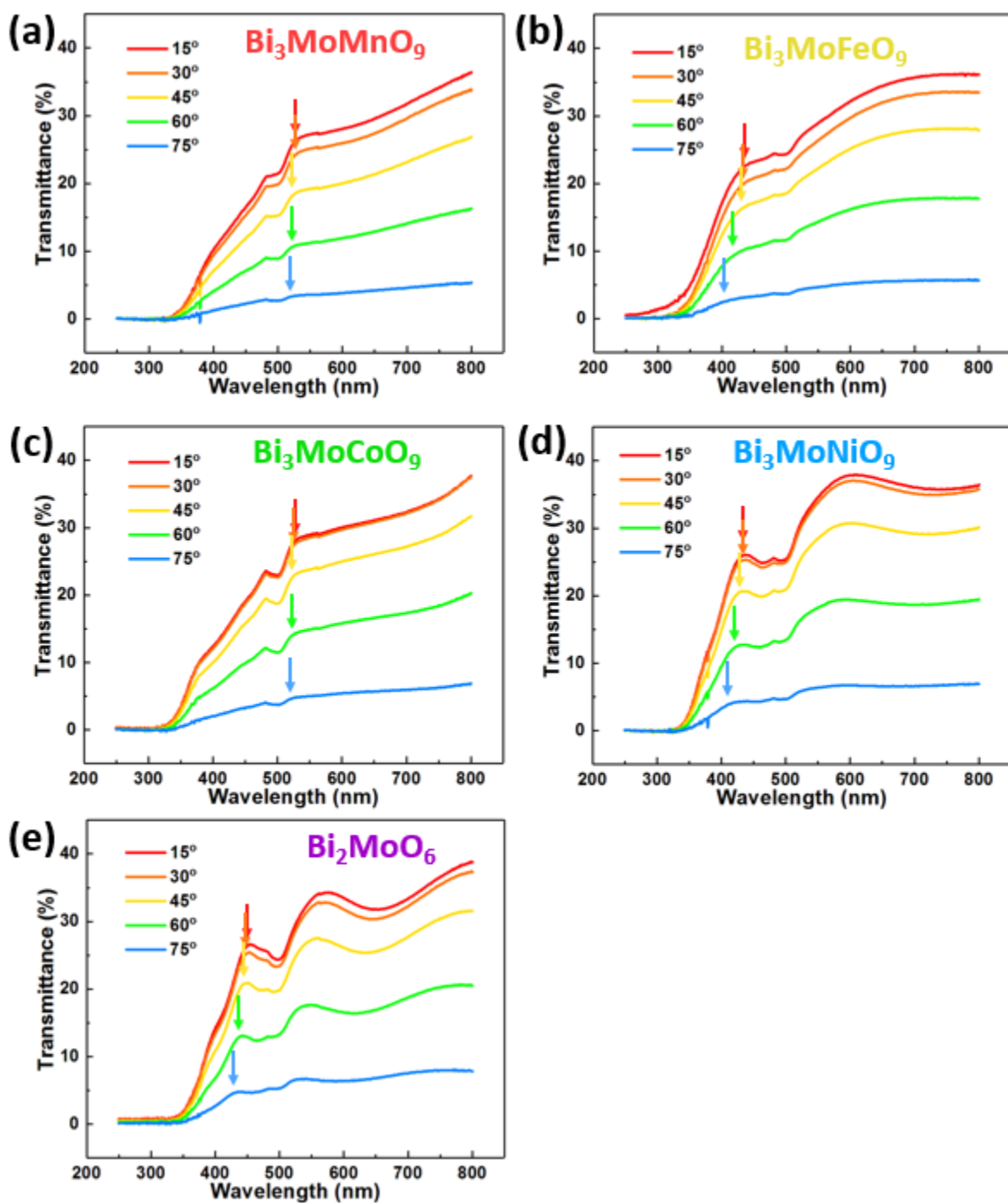
Figure 5.8 (a-d) Angular dependence of the transmittance spectra of the BMoM$_T$O films with different elements (Mn, Fe, Co and Ni, respectively). (e) Angular dependence of the transmittance spectra of the BMoO film.

The ellipsometry experiments were conducted to further explore the anisotropic optical properties of the BMoM$_T$O thin films. Figure 5.9 (a-e) shows the fitted real dielectric constants of the thin films in both IP ($\varepsilon_{//}$ marked with dashed lines) and OP ($\varepsilon_{\perp}$ marked with solid lines) directions. It can be seen that the IP dielectric constants of the BMoM$_T$O thin films have the similar values and trend comparing to the pure BMoO thin film, while the OP dielectric constants vary drastically with the film compositions. All the OP dielectric constants were plotted in Figure 5.9 (f) for better comparison. More specifically, the OP dielectric constant ($\varepsilon_{\perp}$) decreases from Co, Mn, Fe, pure BMoO, to Ni. This leads to OP anisotropy in Co and Mn cases and IP anisotropy in pure BMoO, Fe and Ni cases. This tunable optical dielectric properties are resulted from the structures. For IP, the layered structure dominates the electronic density of states and the light-matter interactions IP and thus results in the very similar IP ($\varepsilon_{//}$) constant. For OP, depending on the secondary dopants and the structural variation, the density of states in the samples varies and thus results in the largely different OP dielectric constant ($\varepsilon_{\perp}$). The results of the ellipsometry experiments have demonstrated the tunable optical properties such as OP dielectric constant and overall optical dielectric anisotropy properties.
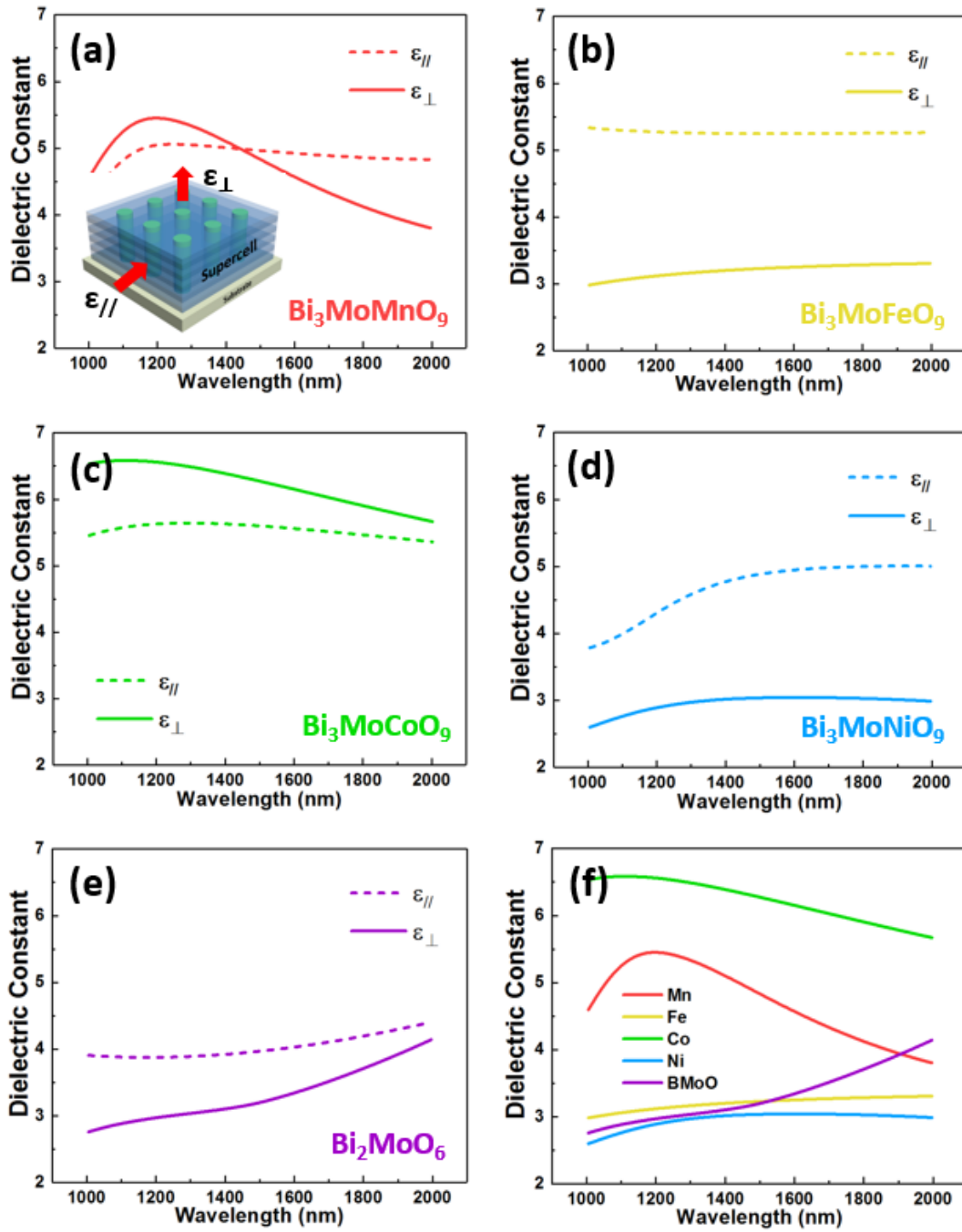
Figure 5.9 (a-e) Fitted real dielectric constants of the BMoM$_T$O and BMoO thin films in both in-plane (marked with dashed lines) and out-of-plane (marked with solid lines) directions. (f) Comparison of the out-of-plane dielectric constants of the BMoM$_T$O and BMoO thin films.

In this work, the design and fabrication of new nanocomposites by combing an Aurivillius phase material with a perovskite-type transition metal oxide in a unique nanopillar-in-matrix form provide an effective approach of exploring new material systems using layered SC structures. The advantages of the compositional varied domains, instead of the completely different secondary phases, include that (1) high quality layered nanocomposite structures were maintained without much film quality deterioration due to secondary phase growth, (2) novel layered oxide properties remain dominant in IP , such as ferroelectric properties and nonlinearity, while the OP properties are tunable depending on secondary dopant in the systems; (3) highly anisotropic physical properties can be achieved easily in these layered nanocomposite systems by proper selection of the secondary phases, which provides large flexibility in nanocomposite designs and property tuning.

5.5   Conclusion

$Bi_3MoM_TO_9$ (BMoM$_T$O, M$_T$ = Mn, Fe, Co and Ni), a new oxide nanocomposite system with SC layered structure as the matrix has been grown on the LAO (001) substrates by the PLD technique. The thin films have the pillar-like domains (M$_T$-rich) embedded in the matrix (Mo-rich). Instead of forming dislocations and other interfacial defects, the atomic lattices are continuous across the domain boundaries. Room temperature multiferroic properties (i.e. ferroelectricity and ferromagnetism) have been demonstrated in the new systems. Anisotropic multifunctionalities, including ferromagnetism, optical transmittance and dielectric anisotropy, have been demonstrated as a function of the secondary phase composition M$_T$. As the film composition (i.e. M$_T$) varies, the magnetic anisotropy, optical bandgap, dielectric function can be effectively tuned. These tunable multifunctionalities in these layered oxide nanocomposite systems present the promising applications toward sensors, data storage, high-temperature electronics, memory devices and non-linear optical devices.

6. VERTICALLY ALIGNED NANOCOMPOSITE (BATIO3)0.8:(LA0.7SR0.3MNO3)0.2 THIN FILMS WITH ANISOTROPIC MULTIFUNCTIONALITES

6.1   Overview

A new two-phase system $BaTiO_3$:$La_{0.7}Sr_{0.3}MnO_3$ with the molar ratio of 8:2 has been grown onto the single phase $SrTiO_3$ (001) substrates using a one-step pulsed laser deposition technique. The vertically aligned nanocomposite thin films with ultra-thin $La_{0.7}Sr_{0.3}MnO_3$ pillars embedded in $BaTiO_3$ matrix have been obtained and the geometry of the pillars varies with the deposition frequencies. The room temperature multiferroic property, including ferromagnetism and ferroelectricity has been demonstrated. Anisotropic ferromagnetism and dielectric constants have been observed, which can been tuned by deposition frequencies. The tunable anisotropic optical properties is originated from the conducting pillars in dielectric matrix structure, which causes the different electron transport paths. In addition, tunable bandgaps have been discovered in the nanocomposites. This multiferroic and anisotropic system has shown its potential applications towards multiferroics and non-linear optics.

6.2   Introduction

As opposed to the perfect symmetrical orders, anisotropic functional oxides, which have directional dependence in the electric, magnetic, or optical properties, have attracted intensive research interests.[165–168] Anisotropic oxides are the ideal candidates in many applications. For example, anisotropic optical thin films can be used in the optical devices that operate with polarized light.[169] Among all the anisotropic photonic materials, hyperbolic metamaterials have become an active research topic due to their applications in imaging[170–172] and engineering.[173–175] In hyperbolic metamaterials, metals and dielectrics are artificially arranged to form multilayered[176] or nanowire arrays (metal) in matrix (dielectric)[177] structure. In both structures, the materials perform metallic behavior in one direction and dielectric behavior in the other. The big difference between the electric structures of metals and dielectrics is the origin of the hyperbolic dispersion and extreme anisotropic optical properties. For instance, in hyperbolic metamaterials, the dielectric constants in different orientations will have the opposite signs, i.e. $\varepsilon_{//} \cdot \varepsilon_{\perp} < 0$. It has also been

proved that the hyperbolic dispersion can be observed in the multilayered structure by using a highly doped semiconductor as metallic layers.[178]

Vertically aligned nanocomposite (VAN) is a unique structure for introducing anisotropy into the thin films. In VAN nanocomposites, two nonmiscible materials can form a two-phase system with either pillar-pillar or pillar in matrix structures. The vertically aligned pillars can result in a large amount of phase boundaries, which can generate the strong strain coupling perpendicular to the film surface. This vertical strain tuning is unique from the layered thin films, which only generates horizontal strain, and can bring in the anisotropic properties that are tunable with the dimension, density or shape of the pillars.[45,50,179] Metal pillar in oxide matrix VAN structure has been reported and the hyperbolic response has been found in such systems.[180,181]

Inspired by the research of hyperbolic metamaterials, we have designed a VAN system composed of $BaTiO_3$ (BTO) and $La_{0.7}Sr_{0.3}MnO_3$ (LSMO) to achieve the anisotropic optical properties. These two materials were selected for the following reasons: First, both BTO and LSMO are the commonly studied materials that could be grown on $SrTiO_3$ (STO) substrates (due to the small lattice mismatch with STO) for VAN integration. Second, BTO is a dielectric material while LSMO is conducting that can be used as bottom electrodes. By forming a conducting LSMO pillar in dielectric BTO matrix structure, we are expecting to see more conducting response in the OP direction, which could generate the anisotropic optical properties. Third, as the BTO and LSMO are reported as the room temperature ferroelectric and ferromagnetic materials,[18,182] the room temperature multiferroism can be obtained by their combination. Similar approach has been applied for other VAN systems.[131,159,160] In this work, two deposition frequencies of 2 Hz and 10 Hz were utilized for tuning the microstructure of the films, i.e. thinner pillars can be obtained by increasing the deposition frequency. The schematic drawing of such microstructure change is shown in the top portion of Figure 6.1 (a). Detailed property measurements have been conducted to demonstrate the anisotropic properties of the BTO:LSMO thin films. This work has proved the great potential of integrating oxide-oxide VAN thin films with enhanced anisotropic optical properties for optical devices.

6.3   Experimental

The BTO:LSMO target with 8:2 ratio was prepared by a conventional solid-state sintering method. $BaTiO_3$, La_2O_3, $SrCO_3$ and MnO_2 powders were mixed according to the stoichiometry of

the composite target. The nanocomposite thin films were deposited onto the STO (001) substrates by the pulsed laser deposition (PLD) technique. During the deposition, the substrates were kept at 750 ^{o}C in an oxygen atmosphere of 200 mTorr, while the laser with an energy of 420 mJ was shot onto the targets for 3000 pulses. For all the films, the target to substrate distances were kept at 4.5 cm. After the deposition, the films were cooled down to room temperature in 200 Torr oxygen at a rate of 10 ^{o}C/min. For the samples that need the electric property test, a thin layer of $SrRuO_3$ buffer was firstly deposited onto the substrate as the bottom electrode. The microstructure of as-deposited films were firstly checked by X-ray diffraction (XRD, PANalytical Empyrean). Transmittance electron microscopy (TEM, Thermo Scientific TALOS F200X) was utilized for more detailed microstructure examination. The piezoelectric response was investigated using the piezoresponse force microscopy (PFM) embedded in an atomic force microscopy (AFM, Bruker Dimension Icon). The magnetic response was examined by a magnetic property measurement system (MPMS, Quantum Design MPMS-3). During the measurement, the magnetic fields were applied either parallel (in-plane, or IP as abbreviation) or perpendicular to the film surface (out-of-plane, or OP as abbreviation). The real dielectric constants were retrieved from the ellipsometry results obtained from the RC2 spectroscopic ellipsometer (J.A. Woollam Company). The fitting process was conducted using the Spline or Gen-Osc models in the software from the same company (CompleteEase, J.A. Woollam Company). The normal incident depolarized transmittance (T%) spectra was obtained using the spectrophotometer (Lambda 1050 UV/Vis spectrophotometer).

6.4   Results and discussion

After the deposition, the crystallinity of the as-deposited films were investigated by the XRD. Figure 6.1 (b) shows the normalized θ-2θ XRD patterns of the BTO:LSMO thin films deposited at 2 Hz and 10 Hz, respectively. From the XRD patterns, clear BTO (00l) and LSMO (00l) diffraction peaks can be observed, indicating their preferential growth along the OP direction and the separation of the BTO and LSMO peaks demonstrates these two materials have formed two different phases. Lower intensity of the LSMO peaks might be originated from the lower atomic percentage of LSMO (20%) comparing with the BTO phase (80%). The OP lattice parameters of the BTO and LSMO phases can be calculated using the Bragg's law, which are 4.09 Å for BTO and 4.02 Å for LSMO in the 2 Hz sample. These two values are larger than the OP lattice

parameters of their bulk states (4.04 Å for BTO and 3.87 Å for LSMO). The same directional change (both increase) of the OP lattice parameters can be explained by the matching between the BTO, LSMO and STO lattices, as shown in the bottom part of Figure 6.1 (a). As BTO has a larger IP lattice parameter than STO, compressive strain is generated in the BTO lattices in the IP direction, which enlarges its d-spacing in the OP direction. However, as demonstrated later in the TEM discussion, the LSMO phase has formed vertically aligned pillars with very small diameters, which significantly decreases the area attached to the substrate and thus limits the strain tuning effect from the substrate. On the contrary, the huge amount of phase boundaries generated by the thin LSMO pillars enhances the tuning effect from the BTO matrix. As a result, the coupling between the BTO and LSMO lattices has become the major tuning factor for LSMO lattices. As BTO lattice has larger OP lattice parameter (could be even larger after matching with STO), a tensile strain of 3.87% is generated in the LSMO phase, which elongates the lattice of LSMO along the OP direction to the degree close to BTO.
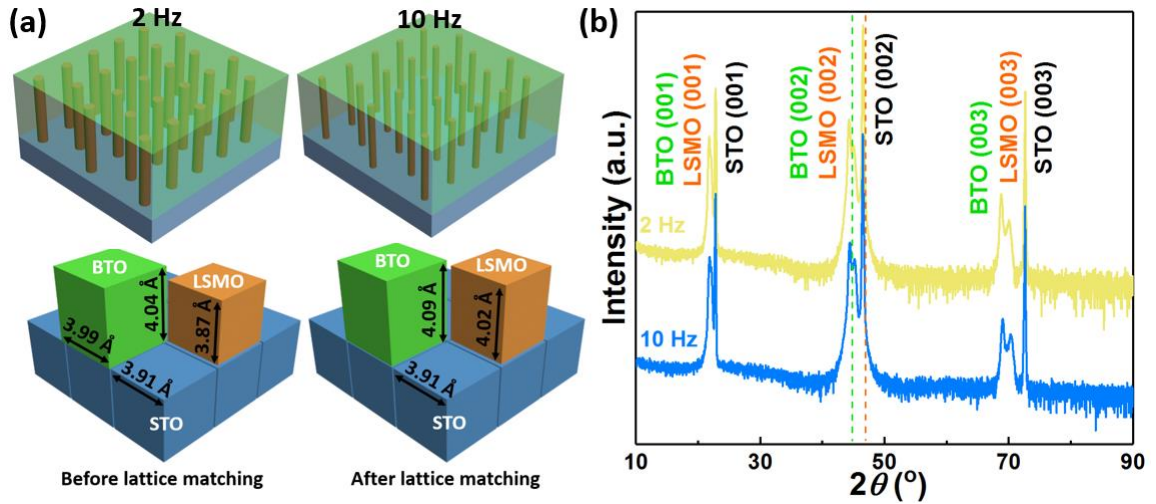
Figure 6.1 (a) 3D schematic drawing of the: BTO:LSMO VAN thin films deposited at 2 Hz and 10 Hz (top); lattice parameters of BTO, LSMO and STO before and after the matching (bottom). (b) θ-2θ XRD scans of BTO:LSMO thin films. The green and purple dashed lines indicate the (002) peak positions of the bulk BTO and LSMO, respectively.

In addition to the XRD scans, TEM was conducted to furtherly understand the microstructure of the BTO:LSMO thin films. Figure 6.2 (a) shows the low-magnification cross-sectional TEM image of the BTO:LSMO thin film deposited at 2 Hz. From the image, it can be observed that the black LSMO pillars are vertically aligned and embedded in the grey BTO matrix, which

demonstrates the VAN structure of the BTO:LSMO thin films. The dark cloud-like shadows in the image are possibly generated by the re-deposition of atoms during the TEM sample preparation process. Selected area electron diffraction (SAED) pattern was taken to demonstrate the orientation relationship of the BTO and LSMO phases as well as the STO substrate, as shown in Figure 6.2 (b). Only (00l) diffraction dots can be observed along the OP direction, which agrees with the XRD results and indicates the highly textured quality of the BTO:LSMO films. In addition, a matching relationship of $(001)_{BTO}//(001)_{LSMO}//(001)_{STO}$ and $[020]_{BTO}//[020]_{LSMO}//[020]_{STO}$ can be determined from the SAED pattern, which proves the cube on cube growth mechanism of the films. The inset of the image shows an enlarged SAED pattern of the $(03\bar{3})$ diffraction dots, where separate dots for BTO, LSMO and STO lattices can be observed, which are merged together when they are close to the original point. Figure 6.2 (c) shows the scanning transmission electron microscopy (STEM) image of the same sample, where clear LSMO pillars with bright contrast (due to higher atomic number) are grown perpendicular to the substrate surface. Similar to the TEM image, a re-deposition area can be noticed at the bottom left corner of the image. A high-resolution STEM (HRSTEM) image of the selected area (marked in the yellow square) is shown in Figure 6.2 (d), where the LSMO pillars and BTO matrix are marked as L and B, respectively. From the HRSTEM image, it can be noticed that the LSMO pillars marked with the yellow arrows have ultra-thin diameters of around six unit cells. Large amount of the phase boundary area can be induced by the tiny diameters of the LSMO pillars, which would significantly increase the strain coupling effect between the BTO and LSMO phases along the OP direction. Other pillars without the marks are thinner and lighter than the marked ones, indicating those pillars are not aligned in the same plane and thus are partially covered by the BTO matrix. Figure 6.3 shows the energy-dispersive X-ray spectra (EDS) mapping of the film, where Ti and Mn atoms are marked in yellow and blue, respectively. The EDS mapping confirms the LSMO pillar in BTO matrix structure, however, the resolution is relatively low and only few of the pillars can be observed (marked with red arrows) due to the fine pillar dimension.
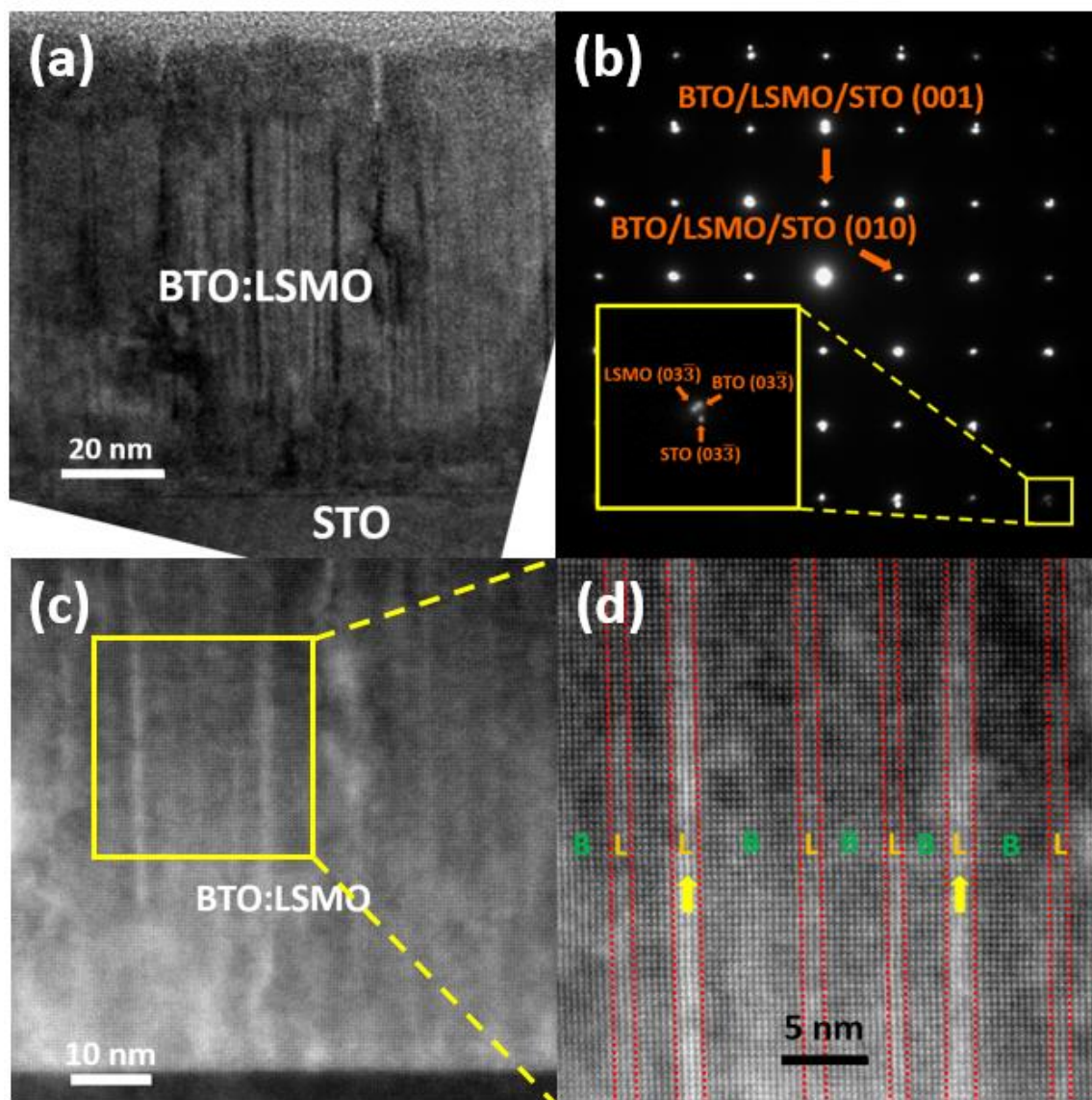
Figure 6.2 (a) Cross-sectional TEM image of the 2 Hz BTO:LSMO thin film. (b) SAED pattern of the film and substrate. The inset shows an enlarged image of the (03$\bar{3}$) dots. Cross-sectional (c) STEM and (d) HRSTEM image of the 2 Hz BTO:LSMO nanocomposite. The letters B and L indicate BTO matrix and LSMO pillars, respectively.
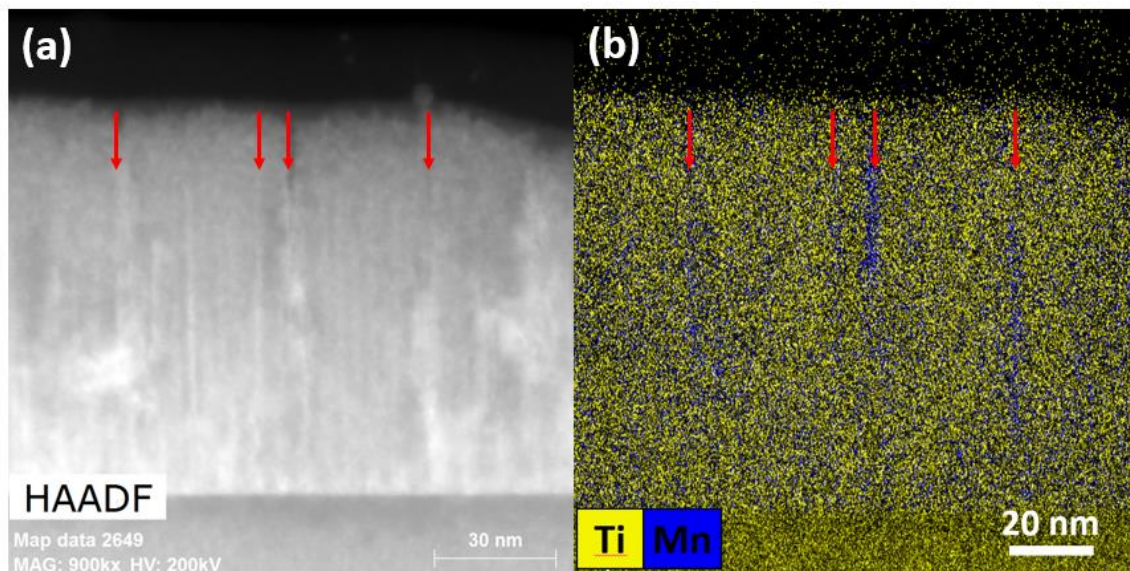
Figure 6.3 Cross-sectional (a) HAADF and (b) EDS mapping of the 2 Hz BTO:LSMO thin film. The Ti and Mn atoms are plotted in yellow and blue, respectively.

The microstructure of the 10 Hz sample was also examined by STEM, as plotted in Figure 6.4. Overall, the film also has the LSMO pillar in BTO matrix structure with the pillar width of around five unit cells. However, unlike the 2 Hz sample, which has the continuous LSMO pillars from the bottom to the top, some of the pillars inside the 10 Hz sample are discontinuous. This phenomenon can be explained by the diffusion of the adatoms during the deposition, which can be expressed as the following equation: $L \approx 2\sqrt{D\tau}$, where L is the diffusion length of the adatoms, D is the diffusion coefficient and the τ is the diffusion time. As the deposition frequency increases from 2 Hz to 10 Hz, the diffusion time (time between the laser pulses) of the adatoms is limited, which generally will cause smaller nucleation islands and decrease the dimension of the pillars grown by those islands, as shown in the top panel of Figure 6.1 (a).[42,97] However, in this work, as the 2 Hz sample already has the ultra-thin pillars that are grown from the tiny nucleation islands, the decreased diffusion time cannot furtherly decrease the dimension of the nucleation islands and the pillar width due to the surface energy. Instead, as the IP diffusion of the adatoms is limited, there is not enough time for the add-on LSMO atoms to move and lie on top of the pre-deposited LSMO atoms to form continuous straight pillars. As a result, some of the LSMO pillars are discontinued or misaligned, as shown in Figure 6.4 (b).
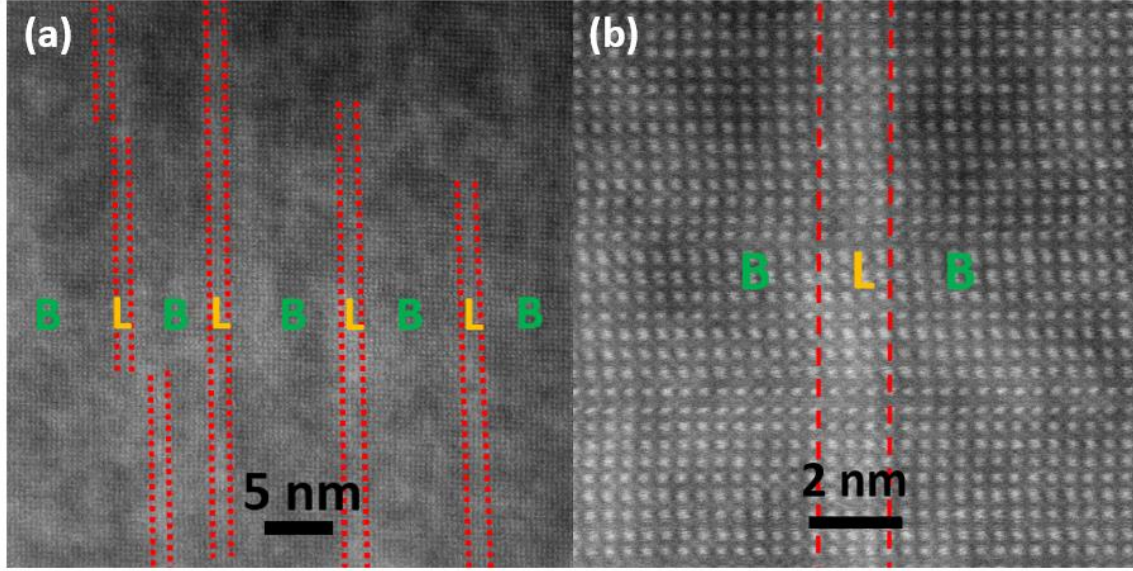
Figure 6.4 Cross-sectional (a) STEM and (b) HRSTEM images of the 10 Hz BTO:LSMO thin film with the BTO and LSMO phases marked as the letters B and L.

The ferromagnetic response of the BTO:LSMO thin films is measured using the MPMS. Figure 6.5 (a) shows the magnetic hysteresis loops of a BTO:LSMO film deposited at 2 Hz, with the magnetic field applied parallel and perpendicular to the substrate surface (the magnetic field direction are illustrated in the inset). It is obvious to see that the BTO:LSMO nanocomposite has the room temperature ferromagnetic response, even though this response is relatively weak as a result of the low concentration of LSMO (20%). Besides, the ferromagnetic response also shows IP anisotropy, which has stronger magnetic response in the IP direction than the OP direction. Similar anisotropic results can be observed in the 10 Hz and pure LSMO thin films, which are plotted in Figure 6.6. Table. 6.1 summarizes the IP (M_{IP}) and OP (M_{OP}) magnetization of different films at 5000 Oe and their ratio (M_{IP}/M_{OP}) showing the degree of anisotropy. Comparing with pure LSMO thin film, it is interesting to see the anisotropy of the BTO:LSMO thin films are switched from IP to OP dominating. As the strain is a key factor of influencing the anisotropic ferromagnetism in LSMO thin films,[51,52] the existence of the tensile strain in the LSMO pillars could possibly change the easy axis direction from IP to OP and result in this switch. Since part of the pillars are disconnected in the 10 Hz sample, the strain effect from the substrate is furtherly restricted while the vertical strain is more dominating (i.e. decreased M_{IP} and increased M_{OP}). The above discussion has demonstrated the tunable room temperature anisotropic ferromagnetic

response of BTO:LSMO thin films via controlling the deposition frequencies (i.e. microstructure of pillars).

Table 6.1 Magnetization of LSMO and BTO:LSMO thin films at 5000 Oe with different measurement orientations

Magnetization at 5000 Oe	LSMO	2 Hz	10 Hz
M_{IP}	316.44	15.29	9.52
M_{OP}	7.01	1.54	1.70
M_{IP}/M_{OP}	45.14	9.93	5.60

In addition to ferromagnetic property, the room temperature ferroelectric response of the BTO:LSMO thin film was studied. Figure 6.5 (b) shows the PFM phase image of a 2 Hz sample, while the reversed tip bias of +10 V and -10 V are applied in a square area with the dimensions of 1 x 1 μm^2 and 0.5 x 0.5 μm^2, respectively. A clear contrast change, indicating the phase change of the thin film, can be noticed as the opposite voltage is applied. From the phase image, the ferroelectric response of the BTO:LSMO thin films is demonstrated, while coupling the ferromagnetic hysteresis loops, the overall room temperature multiferroic response is illustrated. This result suggests the potential application of BTO:LSMO thin films in magnetoelectric devices.
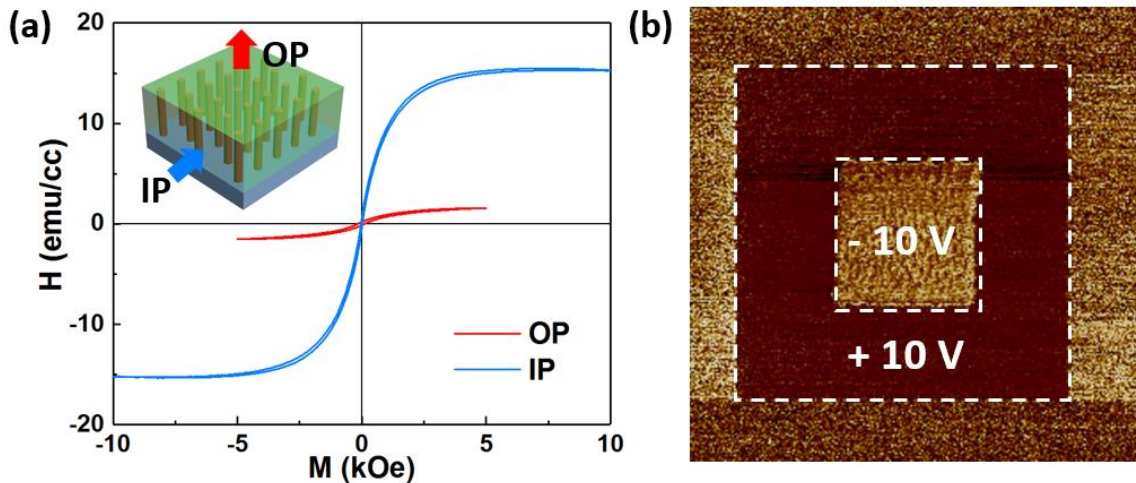
Figure 6.5 (a) The room temperature magnetic hysteresis loops of the 2 Hz BTO:LSMO thin film with the magnetic field applied in both IP and OP directions, as shown in the inserted schematic drawing. (b) The room temperature PFM phase image of the 2 Hz BTO:LSMO thin film with the writing and rewriting tip bias of +10 V and -10 V.

117
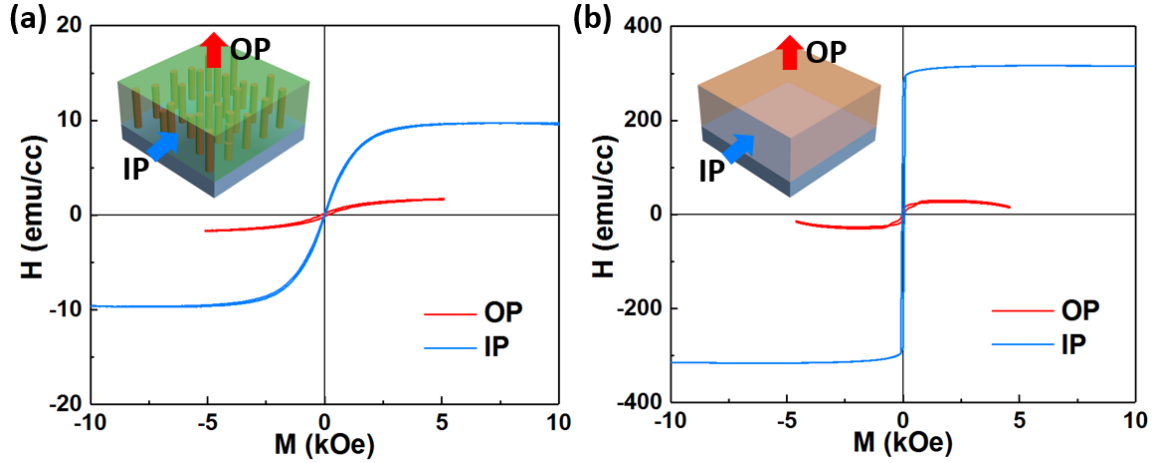
Figure 6.6 The room temperature magnetic hysteresis loops of the (a) 10 Hz BTO:LSMO thin film and (b) pure LSMO thin film with the magnetic field applied in both IP and OP directions. The directions of the applied magnetic fields are shown in the inserted schematic drawings.

The optical properties of the BTO:LSMO thin films were measured by ellipsometer and the real part of the dielectric constants were fitted from the elliposometry results, as shown in Figure 6.7 . As shown in Figure 6.7 (a), anisotropic ellipsometry parameters can be observed in pure BTO film, which has larger OP dielectric constants ($\varepsilon_{//}$) than the IP ones ($\varepsilon_{\perp}$). This phenomenon is originated from the substrate induced compressive strain in the BTO lattices, which elongates the lattices in the OP direction and thus allows the electrons to move vertically. As a result, the single phase BTO thin film has anisotropic dielectric constants with lower values in the OP direction. On the other hand, the LSMO thin film shows isotropic dielectric constants, as shown in Figure 6.7 (b). The isotropic dielectric constants might result from the conducting nature of the LSMO lattices, where the electrons can move equally in both IP and OP directions. Besides, the lower values of the dielectric constants in LSMO film are predictable due to its high conductivity. The dielectric constants in BTO:LSMO nanocomposite are shown in Figure 6.7 (c) and (d), where enhanced anisotropy can be observed. In the 2 Hz sample, the vertically aligned LSMO pillars provide the easy paths for the electrons to move perpendicularly, which lowers the dielectric constant in the OP direction. On the contrary, since the pillars have tiny diameters, the IP transportation of the electrons is still dominated by the BTO matrix, which results in the similar values of the IP dielectric constants comparing with the pure BTO film. Enhanced anisotropic dielectric constants can also be found in the 10 Hz sample, even though the properties are not as

good as the 2 Hz sample due to the discontinuous pillars in the thin film, which limits the transportation of electrons in the OP direction. Overall, the enhanced anisotropic dielectric constants, which are strongly related to the microstructure of the thin films, can be achieved by adding conducting LSMO pillars into the system.
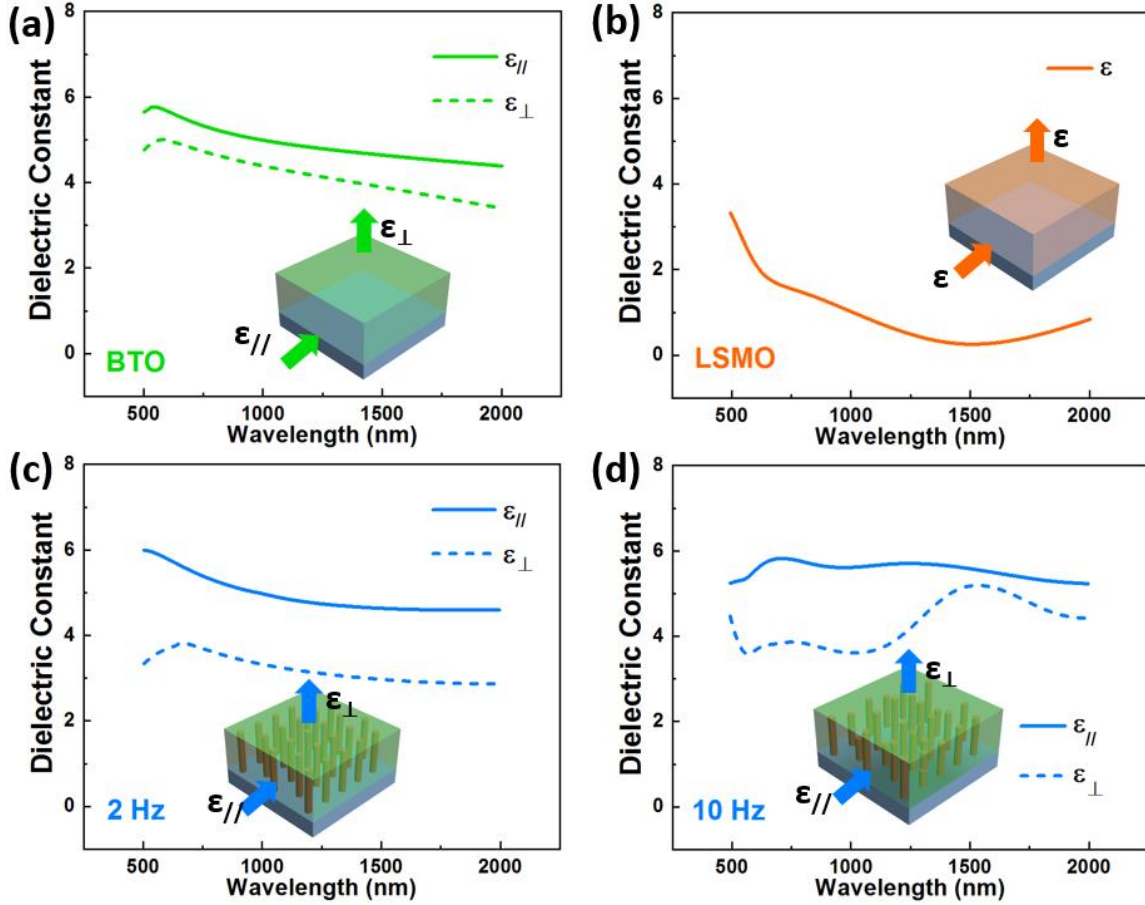
Figure 6.7 Fitted real part of the dielectric constants for (a) pure BTO (b) pure LSMO (c) 2 Hz BTO:LSMO and (d) 10 Hz BTO:LSMO thin films. The ordinary and extraordinary curves are plotted in solid and dashed lines, respectively.

The transmittance of the BTO:LSMO thin films were measured to explore the change of their electronic structures. Figure 6.8 shows the band gaps of the BTO:LSMO nanocomposites deposited at 2 Hz and 10 Hz, which are derived from their transmittance spectra (inset of the figures) via the Tauc method. The result of the pure BTO film is shown in Figure 6.9 as a comparison. It can be noticed that the transmittances of the nanocomposites are lower than the single phased BTO, which might be caused by the introduction of the secondary phase and the formation of the phase

boundaries in the films. Specifically, the 10 Hz sample has lower transmittance than the 2 Hz one as it has less ordered structure. Besides, the BTO:LSMO thin films have lower band gaps than the pure BTO film and are increasing as the deposition frequency increases. The drop of the band gaps in nanocomposites derives from the introduction of the conducting LSMO phase, which has a narrow band gap of 0.63 eV.[183] The LSMO pillars have formed the easy paths for the electron transportation, which subsequently decreases the band gap of the films. From the TEM analysis, these "paths" are more continuously aligned in the 2 Hz sample, thus lower band gap can be found in the sample with a deposition frequency of 2 Hz.
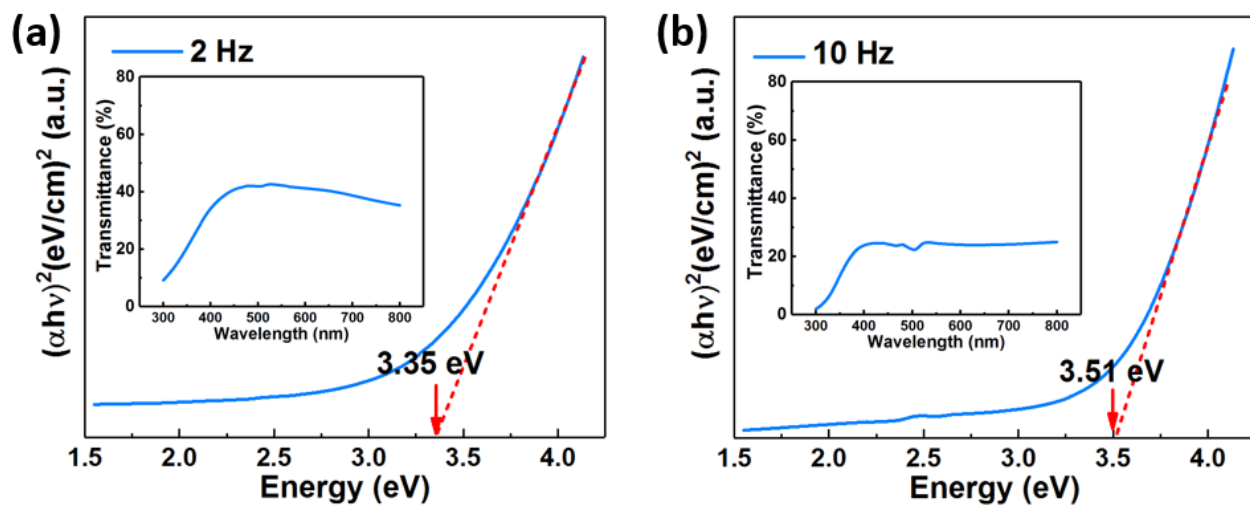
Figure 6.8 Direct band gaps of the (a) 2 Hz and (b) 10 Hz BTO:LSMO thin films. The corresponding transmittance spectra are shown as inset.
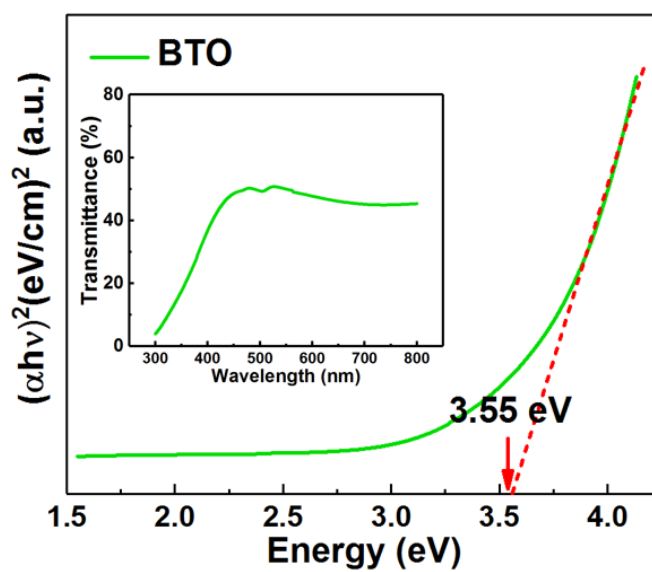
Figure 6.9 Direct band gaps of the pure BTO thin film with the corresponding transmittance spectra shown as an inset.

In this work, the design of embedding conducting oxide pillars into the dielectric oxide matrix presents an approaching of obtaining tunable anisotropic optical properties. The VAN structure can provide multiple tuning parameters, including oxygen pressure, substrate temperature, deposition frequency and energy for the microstructure and strain tuning. By the material selections, tunable anisotropic multifunctionalities, including ferroelectricity, ferromagnetism and optical property can be obtained in VAN thin films.

6.5   Conclusion

In summary, we have firstly reported a VAN system with the composition of $(BaTiO_3)_{0.8}:(La_{0.7}Sr_{0.3}MnO_3)_{0.2}$, which is grown onto the STO (001) substrate via PLD. The cross-sectional TEM and STEM images have demonstrated that the ultra-thin LSMO pillars with a dimension of around five unit cells were embedded in the BTO matrix. By changing the deposition frequencies from 2 Hz to 10 Hz, the arrangement of the pillars are tuned from continuous to partially discontinuous alignment. With the pillar geometry change, the anisotropy of the ferromagnetic property has been tuned from IP dominating to OP dominating, which might be attributed to the change of the easy magnetization axis rotation in the LSMO lattices. Coupled with the ferroelectric response, the room temperature multiferroic property has been obtained. The vertically aligned conducting pillars have provided an easy transport path for the electrons, thus the anisotropic dielectric constants in the nanocomposite have been enhanced comparing to the pure BTO film. In addition to the dielectric constants, tunable band gaps have also been achieved in this system. The BTO:LSMO system presents enormous application opportunities in data storage devices and non-linear optical devices.

7. SUMMARY AND FUTURE WORK

In this dissertation, we systematically investigated the tunable multifunctionalities in oxide-based nanocomposite thin films. Four first-time reported nanocomposite systems have been demonstrated with vertically aligned nanocomposite or multilayered structures. By controlling the deposition frequency, film composition and the element in the system, tunable ferromagnetic, ferroelectric, multiferroic, magnetotransport and optical properties have been achieved. The multifunctionality study on these oxide nanocomposite thin films has shown great potential in real life applications including nanoscale memory devices, sensors, spintronics, data storage devices etc.

First, tunable microstructure has been achieved in all four thin film systems. In BTO:YMO and BTO:LSMO thin films, the structure of the pillars is tuned by deposition frequency, which affects the diffusion time of the adatoms. By increasing the deposition frequency, the pillars in BTO:YMO thin films become thinner and the ultra-thin pillars in BTO:LSMO thin films become discontinuous. The LCMO:CeO$_2$ thin films have a CeO$_2$ pillars embedded in LCMO matrix structure, while the size and density of the pillars can be tuned by controlling the atomic percentage of the CeO$_2$ in the films. In BMoM$_T$O thin films, the transition metal rich pillar-like domains have been formed in Mo-rich matrix. By changing the metal element (Mn, Fe, Co and Ni) in the films, the geometric structures of the domains have been tuned. Second, some functionalities have been achieved in the nanocomposites by the interaction of the materials. The multiferroic property and ME coupling are obtained by combining a ferromagnetic material with a ferroelectric material. The LFMR in LCMO is originated from the phase boundary generated by the insulating CeO$_2$. Third, tunable functionalities have been achieved in the oxide thin films. Strain engineering plays an important role in this process, which affects the ferromagnetic property in BTO:YMO and BTO:LSMO thin films, as well as the metal-to-insulator transition temperature in LCMO:CeO$_2$ thin films. The anisotropic functionalities including ferromagnetism, transmittance and dielectric constants are generated by the anisotropic structures of the thin films, which can be tuned by the deposition frequency, film composition and element in the film. In addition, tunable band gaps have been observed in BMoM$_T$O and BTO:LSMO thin films.

We have shown the strong functionality tuning effect in oxide-based nanocomposite thin films. The future research can be focused on the following aspects:

1. Fundamental growth mechanisms. For example, in BMoM$_T$O thin films, what determines the shape, size and density of the domains? Is it possible to tune the domain microstructures by deposition conditions (e.g., substrate temperature, oxygen pressure, laser energy, laser frequency, etc.)?

2. Multifunctionality exploration. Even though many functionalities have been studied in this dissertation, but other coupling effects such as thermoelectric, photochemical and memristor response are also worth exploring.

3. Growth on other substrates. The commercialized single crystal substrates like STO and LAO are used in this dissertation. However, the cost of these substrates is still unacceptable in industry. The integration of these thin films on Si or flexible substrate like Mica can be explored.

4. Device integration. Can above-mentioned thin films be incorporated in nanoscale devices?

REFERENCES

1. Nath, S., Bodhak, S. & Basu, B. HDPE-Al_2O_3-HAp Composites for Biomedical Applications: Processing and Characterizations. *J. Biomed. Mater. Res. Part B Appl. Biomater.* **88B**, 1–11 (2008).

2. Santos, J. D. S. & Monteiro, F. J. Wear Behaviour of Stainless Steelafter Al_2O_3 Plasma Spraying for Biomedical Applications. *Surf. Eng.* **6**, 209–212 (1990).

3. Hippel, A. Von. Ferroelectricity, Domain Structure, and Phase Transitions of Barium Titanate. *Rev. Mod. Phys.* **22**, 221–237 (1950).

4. Yang, G., Yue, Z., Zhao, J., Wen, H., Wang, X. & Li, L. Dielectric behaviour of $BaTiO_3$-based ceramic multilayer capacitors under high dc bias field. *J. Phys. D. Appl. Phys.* **39**, 3702–3707 (2006).

5. Yasue, T., Komatsu, T., Nakamura, N., Hashimoto, K., Hirano, H., Esashi, M. & Tanaka, S. Wideband tunable Love wave filter using electrostatically actuated MEMS variable capacitors integrated on lithium niobate. *Sensors Actuators A. Phys.* **188**, 456–462 (2012).

6. Chen, Z., Arita, K., Lim, M. & Araujo, C. A. P. De. Graded PZT thin film capacitors with stoichimetric variation by MOD technique. *Integr. Ferroelectr.* **24**, 181–188 (1999).

7. Cuadras, A., Gasulla, M., Ghisla, A. & Ferrari, V. Energy Harvesting From PZT Pyroelectric Cells. in *IEEE Instrumentation and Measurement Technology Conference* vol. April 1668–1672 (2006).

8. Haertling, G. H. & Land, C. E. Hot-Pressed (Pb, La)(Zr, Ti)O_3 Ferroelectric Ceramics for Electrooptic Applications. *J. Am. Ceram. Soc.* **54**, 1–11 (1971).

9. Look, D. C. Recent advances in ZnO materials and devices. *Mater. Sci. Eng.* **B80**, 383–387 (2001).

10. Xu, C., Shin, P. H., Cao, L., Wu, J. & Gao, D. Ordered TiO_2 Nanotube Arrays on Transparent Conductive Oxide for Dye-Sensitized Solar Cells. *Chem. Mater.* **22**, 143–148 (2010).

11. Son, J. Y., Kim, B. G., Kim, C. H. & Cho, J. H. Writing polarization bits on the multiferroic $BiMnO_3$ thin film using Kelvin probe force microscope. *Appl. Phys. Lett.* **84**, 4971–4973 (2004).

12. Wang, J., Neaton, J. B., Zheng, H., Nagarajan, V., Ogale, S. B., Liu, B., Viehland, D., Vaithyanathan, V., Schlom, D. G., Waghmare, U. V, Spaldin, N. A., Rabe, K. M., Wuttig, M. & Ramesh, R. Epitaxial $BiFeO_3$ Multiferroic Thin Film Heterostructures. *Science (80-.).* **299**, 1719–1722 (2003).

13. Wu, M. K., Ashburn, J. R. & Torng, C. J. Superconductivity at 93 K in a New Mixed-Phase Y-Ba-Cu-O Compound System at Ambient Pressure. *Phys. Rev. Lett.* **58**, 908–910 (1987).

14. Paranthaman, M. P. & Izumi, T. High-Performance YBCO-Coated Superconductor Wires. *MRS Bull.* **29**, 533–541 (2004).

15. Hsu, F., Luo, J., Yeh, K., Chen, T., Huang, T., Wu, P. M., Lee, Y., Huang, Y., Chu, Y., Yan, D. & Wu, M. Superconductivity in the PbO-type structure α-FeSe. *Proc. Natl. Acad. Sci. U. S. A.* **105**, 14262–14264 (2008).

16. Hosono, E., Kudo, T., Honma, I., Matsuda, H. & Zhou, H. Synthesis of Single Crystalline Spinel $LiMn_2O_4$ Nanowires for a Lithium Ion Battery with High Power Density. *Nano Lett.* **9**, 1045–1051 (2009).

17. Cao, Q., Zhang, H. P., Wang, G. J., Xia, Q., Wu, Y. P. & Wu, H. Q. A novel carbon-coated $LiCoO_2$ as cathode material for lithium ion battery. *Electrochem. commun.* **9**, 1228–1232 (2007).

18. Choi, K. J., Biegalski, M., Li, Y. L., Sharan, A. & Schubert, J. Enhancement of Ferroelectricity in Strained $BaTiO_3$ Thin Films. *Science (80-.).* **306**, 1005–1010 (2004).

19. Martin, L. W., Chu, Y. & Ramesh, R. Advances in the growth and characterization of magnetic , ferroelectric , and multiferroic oxide thin films. *Mater. Sci. Eng. R Reports* **68**, 89–133 (2010).

20. Smith, M. B., Page, K., Siegrist, T., Redmond, P. L., Walter, E. C., Seshadri, R., Brus, L. E. & Steigerwald, M. L. Crystal structure and the paraelectric-to-ferroelectric phase transition of nanoscale $BaTiO_3$. *J. Am. Chem. Soc.* **130**, 6955–6963 (2008).

21. Huang, J., Gao, X., Macmanus-driscoll, J. L. & Wang, H. *Ferroelectric thin films and nanostructures: current and future*. *Nanostructures in Ferroelectric Films for Energy Applications: Grains, Domains, Interfaces and the Engineering Methods* (Elsevier Inc., 2019).

22. Zener, C. Interaction between the d-Shells in the Transition Metals. II. Ferromagnetic Compounds of Manganese with Perovskite Structure. *Phys. Rev.* **82**, (1951).

23. Mathews, M., Jansen, R., Rijnders, G., Lodder, J. C. & Blank, D. H. A. A. Magnetic oxide nanowires with strain-controlled uniaxial magnetic anisotropy direction. *Phys. Rev. B* **80**, 064408 (2009).

24. Hwang, H. Y., Cheong, S.-W., Radaelli, P. G., Marezio, M. & Batlogg, B. Lattice effects on the magnetoresistance in doped $LaMnO_3$. *Phys. Rev. Lett.* **75**, 914–917 (1995).

25. Malavasi, L., Fisher, C. A. J. & Slam, M. S. Oxide-ion and proton conducting electrolyte materials for clean energy applications: structural and mechanistic features. *Chem. Soc. Rev.* **39**, 4370–4387 (2010).

26.   Jaafar, M. F. Study and Modeling of Ferromagnetic Hysteresis. in *International Conference on Electrical Engineering and Software Applications* vol. March 1–6 (IEEE, 2013).

27.   Valasek, J. Piezo-electric and allied phenomena in rochelle salt. *Phys. Rev.* **17**, 475–481 (1921).

28.   Haertling, G. H. Ferroelectric Ceramics: History and Technology. *J. Am. Ceram. Soc.* **82**, 797–818 (1999).

29.   Aken, B. B. Van, Rivera, J.-P., Schmid, H. & Fiebig, M. Observation of ferrotoroidic domains. *Nature* vol. 449 702–705 (2007).

30.   Spaldin, N. A. & Fiebig, M. The Renaissance of Magnetoelectric Multiferroics. *Science (80-.).* **309**, 391–392 (2005).

31.   Manipatruni, S., Nikonov, D. E. & Young, I. A. Beyond CMOS computing with spin and polarization. *Nat. Phys.* **14**, 338–343 (2018).

32.   Khomskii, D. Classifying multiferroics: Mechanisms and effects. *Physics (College. Park. Md).* **2**, (2009).

33.   Thomson, W. XIX. On the electro-dynamic qualities of metals:—Effects of magnetization on the electric conductivity of nickel and of iron. *Proc. R. Soc. london* **8**, 546–550 (1857).

34.   Baibich, M. N., Broto, J. M., Fert, A., Dau, F. N. Van & Petroff, F. Giant Magnetoresistance of (001)Fe/(001)Cr Magnetic Superlattices. *Phys. Rev. Lett.* **61**, 2472–2475 (1988).

35.   Binasch, G., Grünberg, P., Saurenbach, F. & Zinn, W. Enhanced magnetoresistance in layered magnetic structures with antiferromagnetic interlayer exchange. *Phys. Rev. B* **39**, 4828–4830 (1989).

36.   Siwach, P. K., Singh, H. K. & Srivastava, O. N. Low field magnetotransport in manganites. *J. Phys. Condens. Matter* **20**, 273201 (2008).

37.   Tauc, J. Optical properties and electronic structure of amorphous Ge and Si. *Mater. Res. Bull.* **3**, 37–46 (1968).

38.   Chiu, F. Conduction Mechanisms in Resistance Switching Memory Devices Using Transparent Boron Doped Zinc Oxide Films. *Materials (Basel).* **7**, 7339–7348 (2014).

39.   Narayan, J. & Larson, B. C. Domain epitaxy: A unified paradigm for thin film growth. *J. Appl. Phys.* **93**, 278–285 (2003).

40.   Fan, M., Zhang, W., Khatkhatay, F., Li, L. & Wang, H. Enhanced tunable magnetoresistance properties over a wide temperature range in epitaxial $(La_{0.7}Sr_{0.3}MnO_3)_{1-x}:(CeO_2)_x$ nanocomposites. *J. Appl. Phys.* **118**, 10–15 (2015).

41. Schlom, D. G., Chen, L., Fennie, C. J., Gopalan, V., Muller, D. A., Pan, X., Ramesh, R. & Uecker, R. Elastic strain engineering of ferroic oxides. *MRS Bull.* **39**, 118–130 (2014).

42. Chen, A., Bi, Z., Jia, Q., Macmanus-driscoll, J. L. & Wang, H. Microstructure , vertical strain control and tunable functionalities in self-assembled , vertically aligned nanocomposite thin films. *ACTA Mater.* **61**, 2783–2792 (2012).

43. Zuo, J., Shah, A. B., Kim, H., Meng, Y., Gao, W. & Rouviere, J.-L. Lattice and strain analysis of atomic resolution Z-contrast images based on template matching. *Ultramicroscopy* **136**, 50–60 (2014).

44. Yang, B. H., Wang, H., Yoon, J., Wang, Y., Jain, M., Feldmann, D. M., Dowden, P. C., Macmanus-driscoll, J. L. & Jia, Q. Vertical Interface Effect on the Physical Properties of Self-Assembled Nanocomposite Epitaxial Films. *Adv. Mater.* **21**, 3794–3798 (2009).

45. Gao, X., Li, L., Jian, J., Huang, J., Sun, X., Zhang, D. & Wang, H. Tunable low-field magnetoresistance properties in $(La_{0.3}Ca_{0.3}MnO_3)_{1-x}$:$(CeO_2)_x$ nanocomposite thin films. *Appl. Phys. Lett.* **115**, 053103 (2019).

46. Lebedev, O. I., Verbeeck, J., Tendeloo, G. Van, Shapoval, O., Belenchuk, A., Moshnyaga, V., Damashcke, B. & Samwer, K. Structural phase transitions and stress accommodation in $(La_{0.67}Ca_{0.33}MnO_3)_{1-x}$:$(MgO)_x$ composite films. *Phys. Rev. B* **66**, 104421 (2002).

47. Zheng, H., Wang, J., Lofland, S. E., Ma, Z., L. Mohaddes-Ardabili, Zhao, T., Salamanca-Riba, L., Shinde, S. R., Ogale, S. B., Bai, F., Viehland, D., Jia, Y., Schlom, D. G., Wuttig, M., Roytburd, A. & Ramesh, R. Multiferroic $BaTiO_3$-$CoFe_2O_4$ Nanostructures. *Science (80-.).* **303**, 661–664 (2004).

48. Manus-driscoll, J. L., Zerrer, P., Wang, H., Yang, H., Yoon, J., Fouchet, A., Yu, R., Blamire, M. G. & Jia, Q. Strain control and spontaneous phase ordering in vertical nanocomposite heteroepitaxial thin films. *Nat. Mater.* **7**, 2008 (2008).

49. Zheng, B. H., Straub, F., Zhan, Q., Yang, P., Hsieh, W., Zavaliche, F., Chu, Y., Dahmen, U. & Ramesh, R. Self-Assembled Growth of $BiFeO_3$–$CoFe_2O_4$ Nanostructures. *Adv. Mater.* **18**, 2747–2752 (2006).

50. Zhang, W., Chen, A., Bi, Z., Jia, Q., Macmanus-driscoll, J. L. & Wang, H. Interfacial coupling in heteroepitaxial vertically aligned nanocomposite thin films: From lateral to vertical control. *Curr. Opin. Solid State Mater. Sci.* **18**, 6–18 (2014).

51. Tsui, F., Smoak, M. C., Nath, T. K. & Eom, C. B. Strain-dependent magnetic phase diagram of epitaxial $La_{0.67}Sr_{0.33}MnO_3$ thin films. *Appl. Phys. Lett.* **76**, 2421–2423 (2000).

52. Suzuki, Y., Hwang, H. Y., Cheong, S.-W. & Dover, R. B. van. The role of strain in magnetic anisotropy of manganite thin films. *Appl. Phys. Lett.* **71**, 140–142 (1997).

53. Pesquera, D., Herranz, G., Barla, A., Pellegrin, E., Bondino, F., Magnano, E., Sanchez, F. & Fontcuberta, J. Surface symmetry-breaking and strain effects on orbital occupancy in transition metal perovskite epitaxial films. *Nat. Commun.* **3**, 1–7 (2012).

54. Adamo, C., Ke, X., Wang, H. Q., Xin, H. L., Heeg, T., Hawley, M. E., Zander, W., Schubert, J., Schiffer, P., Muller, D. A., Maritato, L. & Schlom, D. G. Effect of biaxial strain on the electrical and magnetic properties of (001) $La_{0.3}Sr_{0.3}MnO_3$ thin films. *Appl. Phys. Lett.* **95**, 112504 (2009).

55. Miyazaki, T. & Jin, H. *The physics of ferromagnetism. Springer* (2012).

56. Laan, G. van der. Microscopic origin of magnetocrystalline anisotropy in transition metal thin films. *J. Phys. Condens. Matter* **10**, 3239–3253 (1998).

57. V. G., K., N. A., P. & R., W. Thermodynamic theory of epitaxial ferroelectric thin films with dense domain structures. *Phys. Rev. B* **64**, 214103 (2001).

58. Li, Y. L., Hu, S. Y., Liu, Z. K. & Chen, L. Q. Phase-field model of domain structures in ferroelectric thin films. *Appl. Phys. Lett.* **78**, 3878–3880 (2001).

59. Li, Y. L. & Chen, L. Q. Temperature-strain phase diagram for thin films. *Appl. Phys. Lett.* **88**, 072905 (2006).

60. Ederer, C. & Spaldin, N. A. Effect of Epitaxial Strain on the Spontaneous Polarization of Thin Film Ferroelectrics. *Phys. Rev. Lett.* **95**, 257601 (2005).

61. Warusawithana, M. P., Cen, C., Sleasman, C. R., Woicik, J. C., Li, Y., Kourkoutis, L. F., Klug, J. A., Li, H., Ryan, P., Wang, L., Bedzyk, M., Muller, D. A., Chen, L., Levy, J. & Schlom, D. G. A Ferroelectric Oxide Made Directly on Silicon. *Science (80-.).* **324**, 367–371 (2009).

62. Haeni, J. H., Irvin, P., Chang, W., Uecker, R., Reiche, P., Li, Y. L., Choudhury, S., Tian, W., Hawley, M. E., Craigo, B., Tagantsev, A. K., Pan, X. Q., Streiffer, S. K., Chen, L. Q., Kirchoefer, S. W., Levy, J. & Scholm, D. G. Room-temperature ferroelectricity in strained $SrTiO_3$. *Nature* **430**, 758–761 (2004).

63. Qi, X., Dho, J., Tomov, R., Blamire, M. G. & MacManus-Driscoll, J. L. Greatly reduced leakage current and conduction mechanism in aliovalent-ion- doped $BiFeO_3$. *Appl. Phys. Lett.* **86**, 062903 (2005).

64. Phys, J. A., Zhang, J. X., Dai, J. Y. & Chan, H. L. W. Interfacial engineering and coupling of electric and magnetic properties in $Pb(Zr_{0.53}Ti_{0.47})O_3/CoFe_2O_4$ multiferroic epitaxial multilayers. *J. Appl. Phys.* **107**, 104105 (2010).

65. Zhang, W., Fan, M., Li, L., Chen, A., Su, Q., Jia, Q., Macmanus-driscoll, J. L. & Wang, H. Heterointerface design and strain tuning in epitaxial BiFeO3 : CoFe2O4 nanocomposite films Heterointerface design and strain tuning in epitaxial BiFeO 3 : CoFe 2 O 4 nanocomposite films. **212901**, (2015).

66. Mittra, J., Abraham, G. J., Kesaria, M., Bahl, S., Gupta, A., Shivaprasad, S. M., Viswanadham, C. S., Kulkarni, U. D. & Dey, G. K. Role of substrate temperature in the pulsed laser deposition of zirconium oxide thin film. *Mater. Sci. forum* **710**, 747–761 (2012).

67. Bragg, W. H. & Bragg, W. L. The reflection of X-rays by crystals. *Proc. R. Soc. london* **88**, 428–438 (1913).

68. Callister, W. D. & Rethwisch, D. G. *Materials science and engineering: an introduction. Wiley* (2013).

69. Scigaj, M., Dix, N., Gázquez, J., Varela, M., Fina, I., Domingo, N., Herranz, G., Skumryev, V., Fontcuberta, J. & Sánchez, F. Monolithic integration of room- temperature multifunctional $BaTiO_3$-$CoFe_2O_4$ epitaxial heterostructures on Si(001). *Sci. Rep.* **6**, 31870 (2016).

70. Schmid, H. Multi-ferroic magnetoelectrics. *Ferroelectrics* **162**, 317–338 (1994).

71. Scott, J. F. Data Storage: Multiferroic Memories. *Nat. Mater.* **6**, 256–258 (2007).

72. Eerenstein, W., Mathur, N. D. & Scott, J. F. Multiferroic and magnetoelectric materials. **442**, 759–766 (2006).

73. Spaldin, N. A. & Fiebig, M. The Renaissance of Magnetoelectric Multiferroics. *Science (80-.).* **309**, 391–392 (2005).

74. Hill, N. A. & Rabe, K. M. First Principles Investigation of Ferromagnetism and Ferroelectricity in Bismuth Manganite. *Phys. Rev. B* **59**, 8759–8769 (1999).

75. Seshadri, R. & Hill, N. A. Visualizing the Role of Bi 6s 'Lone pairs' in the Off-Center Distortion in Ferromagnetic $BiMnO_3$. *Chem. Mater.* **13**, 2892–2899 (2001).

76. Nan, C. W., Bichurin, M. I., Dong, S., Viehland, D. & Srinivasan, G. Multiferroic magnetoelectric composites: Historical perspective, status, and future directions. *J. Appl. Phys.* **103**, 031101 (2008).

77. Martí, X., Skumryev, V., Laukhin, V., Sánchez, F., García-Cuenca, M. V., Ferrater, C., Varela, M. & Fontcuberta, J. Dielectric anomaly and magnetic response of epitaxial orthorhombic $YMnO_3$ thin films. *J. Mater. Res.* **22**, 2096–2101 (2007).

78. Van Aken, B. B., Meelsma, A. & Palstra, T. T. M. Hexagonal $YMnO_3$. *Acta Cryst.* **C57**, 230–232 (2001).

79. Fujimura, N., Ishida, T., Yoshimura, T. & Ito, T. Epitaxially grown $YMnO_3$ film: New candidate for nonvolatile memory devices. *Appl. Phys. Lett.* **69**, 1011–1013 (1996).

80. Dho, J. & Blamire, M. G. Competing functionality in multiferroic $YMnO_3$. *Appl. Phys. Lett.* **87**, 252504 (2005).

81. Brinks, H. W., Fjellvag, H. & Kjekshus, A. Synthesis of Metastable Perovskite-type $YMnO_3$ and $HoMnO_3$. *J. Solid State Chem.* **129**, 334–340 (1997).

82. Waintal, A. & Chenavas, J. Transformation sous haute pression de la forme hexagonale de $MnT'O_3$ (T′ = Ho, Er, Tm, Yb, Lu) en une forme perovskite. *Mater. Res. Bull.* **2**, 819–822 (1967).

83. Salvador, P. A., Doan, T.-D., Mercey, B. & Raveau, B. Stabilization of $YMnO_3$ in a perovskite structure as a thin film. *Chem. Mater.* **10**, 2592–2595 (1998).

84. Hsieh, C. C., Lin, T. H., Shih, H. C., Hsu, C. H., Luo, C. W., Lin, J. Y., Wu, K. H., Uen, T. M. & Juang, J. Y. Magnetic ordering anisotropy in epitaxial orthorhombic multiferroic $YMnO_3$ films. *J. Appl. Phys.* **104**, 103912 (2008).

85. Martí, X., Sánchez, F., Skumryev, V., Laukhin, V., Ferrater, C., García-Cuenca, M. V., Varela, M. & Fontcuberta, J. Crystal texture selection in epitaxies of orthorhombic antiferromagnetic $YMnO_3$ films. *Thin Solid Films* **516**, 4899–4907 (2008).

86. Dho, J., Leung, C. W., MacManus-Driscoll, J. L. & Blamire, M. G. Epitaxial and oriented $YMnO_3$ film growth by pulsed laser deposition. *J. Cryst. Growth* **267**, 548–553 (2004).

87. Autieri, C. & Sanyal, B. Unusual ferromagnetic $YMnO_3$ phase in $YMnO_3/La_{2/3}Sr_{1/3}MnO_3$ heterostructures. *New J. Phys.* **16**, 113031 (2014).

88. Marti, X., Skumryev, V., Cattoni, A., Bertacco, R., Laukhin, V., Ferrater, C., García-Cuenca, M. V., Varela, M., Sánchez, F. & Fontcuberta, J. Ferromagnetism in epitaxial orthorhombic $YMnO_3$ thin films. *J. Magn. Magn. Mater.* **321**, 1719–1722 (2009).

89. Zheng, H., Wang, J., Lofland, S. E., Ma, Z., Mohaddes-Ardabili, L., Zhao, T., Salamanca-Riba, L., Shinde, S. R., Ogale, S. B., Bai, F., Viehland, D., Jia, Y., Schlom, D. G., Wuttig, M., Roytburd, A. & Ramesh, R. Multiferroic $BaTiO_3$-$CoFe_2O_4$ Nanostructures. *Science (80-.).* **303**, 661–663 (2004).

90. Ortega, N., Bhattacharya, P., Katiyar, R. S., Dutta, P., Manivannan, A., Seehra, M. S., Takeuchi, I. & Majumder, S. B. Multiferroic properties of $Pb(Zr,Ti)O_3CoFe_2O_4$ composite thin films. *J. Appl. Phys.* **100**, 126105 (2006).

91. Zhang, J. X., Dai, J. Y. & Chan, H. L. W. Interfacial engineering and coupling of electric and magnetic properties in $Pb(Zr_{0.53}Ti_{0.47})O_3/CoFe_2O_4$ multiferroic epitaxial multilayers. *J. Appl. Phys.* **107**, 104105 (2010).

92. Zhang, W., Fan, M., Li, L., Chen, A., Su, Q., Jia, Q., MacManus-Driscoll, J. L. & Wang, H. Heterointerface design and strain tuning in epitaxial $BiFeO_3:CoFe_2O_4$ nanocomposite films. *Appl. Phys. Lett.* **107**, 212901 (2015).

93. Wu, H., Xu, B., Liu, A. & Chai, G. Strain-modulated magnetocapacitance of vertical ferroelectric-ferromagnetic nanocomposite heteroepitaxial films. *J. Phys. D. Appl. Phys.* **45**, 455306 (2012).

94.   Wu, H., Chai, G., Zhou, T., Zhang, Z., Kitamura, T. & Zhou, H. Adjustable magnetoelectric effect of self-assembled vertical multiferroic nanocomposite films by the in-plane misfit strain and ferromagnetic volume fraction. *J. Appl. Phys.* **115**, 114105 (2014).

95.   Wu, H., Ma, X., Zhang, Z., Zhu, J., Wang, J. & Chai, G. Dielectric tunability of vertically aligned ferroelectric-metal oxide nanocomposite films controlled by out-of-plane misfit strain. *J. Appl. Phys.* **119**, 154102 (2016).

96.   Choi, K. J., Biegalski, M., Li, Y. L., Sharan, A., Schubert, J., Uecker, R., Reiche, P., Chen, Y. B., Pan, X. Q., Gopalan, V., Chen, L.-Q., Schlom, D. G. & Eom, C. B. Enhancement of Ferroelectricity in Strained $BaTiO_3$ Thin Films. *Science (80-.).* **306**, 1005–1009 (2004).

97.   Bi, Z., Lee, J. H., Yang, H., Jia, Q., MacManus-Driscoll, J. L. & Wang, H. Tunable lattice strain in vertically aligned nanocomposite $(BiFeO_3)_x:(Sm_2O_3)_{1-x}$ thin films. *J. Appl. Phys.* **106**, 094309 (2009).

98.   Chen, A., Bi, Z., Tsai, C., Lee, J., Su, Q., Zhang, X., Jia, Q., Macmanus-driscoll, J. L. & Wang, H. Tunable Low-Field Magnetoresistance in $(La_{0.7}Sr_{0.3}MnO_3)_{0.5}:(ZnO)_{0.5}$ Self-Assembled Vertically Aligned Nanocomposite Thin Films. *Adv. Funct. Mater.* **21**, 2423–2429 (2011).

99.   Makhlouf, S. A., Parker, F. T., Spada, F. E. & Berkowitz, A. E. Magnetic anomalies in NiO nanoparticles. *J. Appl. Phys.* **81**, 5561–5563 (1997).

100.   Farhadi, S. & Safabakhsh, J. Solid-state thermal decomposition of the $[Co(NH_3)_5CO_3]NO_3\cdot0.5H_2O$ complex: A simple, rapid and low-temperature synthetic route to Co_3O_4 nanoparticles. *J. Alloys Compd.* **515**, 180–185 (2012).

101.   Hoerman, B. H., Ford, G. M., Kaufmann, L. D. & Wessels, B. W. Dielectric properties of epitaxial thin films Dielectric properties of epitaxial $BaTiO_3$ thin films. *Appl. Phys. Lett.* **73**, 2248–2250 (1998).

102.   Lorenz, M., Hirsch, D., Patzig, C., Ho, T., Hohenberger, S., Hochmuth, H., Lazenka, V., Temst, K. & Grundmann, M. Correlation of Interface Impurities and Chemical Gradients with High Magnetoelectric Coupling Strength in Multiferroic $BiFeO_3 - BaTiO_3$ Superlattices. *ACS Appl. Mater. Interfaces* **9**, 18956–18965 (2017).

103.   Lorenz, M., Lazenka, V., Schwinkendorf, P., Bael, M. J. Van, Vantomme, A., Temst, K., Grundmann, M. & Höche, T. Epitaxial Coherence at Interfaces as Origin of High Magnetoelectric Coupling in Multiferroic $BaTiO_3$-$BiFeO_3$ Superlattices. *Adv. Mater. Interfaces* **3**, 1500822 (2016).

104.   Prellier, W., Rauwel Buzin, E., Mercey, B., Simon, C., Hervieu, M. & Raveau, B. Strain effects in charge-ordered $Pr_{0.5}Ca_{0.5}MnO_3$ manganite thin films. *J. Phys. Chem. Solids* **64**, 1665–1669 (2003).

105.   Haghiri-Gosnet, A.-M. & Renard, J. CMR manganites : physics , thin films and devices. *J. Phys. D. Appl. Phys.* **36**, 127–150 (2003).

106. Jin, S., Tiefel, T. H., Mccormack, M., Fastnacht, R. A., Ramesh, R. & Chen, L. H. Thousandfold Change in Resistivity in Magnetoresistive La-Ca-Mn-O Films. *Science (80-.).* **264**, 413–415 (1994).

107. Li, X. W., Gupta, A., Xiao, G. & Gong, G. Q. Low-field magnetoresistive properties of polycrystalline and epitaxial perovskite manganite films. *Appl. Phys. Lett.* **71**, 1124–1126 (1997).

108. Zeng, Z., Greenblatt, M., Subramanian, M. A. & Croft, M. Large low-field magnetoresistance in perovskite-type $CaCu_3Mn_4O_{12}$ without double exchange. *Phys. Rev. Lett.* **82**, 3164–3167 (1999).

109. Wang, H. S., Qi, L., Liu, K. & Chien, C. L. Low-field magnetoresistance anisotropy in ultrathin $Pr_{0.67}Sr_{0.33}MnO_3$ films grown on different substrates. *Appl. Phys. Lett.* **74**, 2212–2214 (1999).

110. Mitani, S., Takahashi, S., Takanashi, K., Yakushiji, K., Maekawa, S. & Fujimori, H. Enhanced Magnetoresistance in Insulating Granular Systems: Evidence for Higher-Order Tunneling. *Phys. Rev.* **81**, 2799–2802 (1998).

111. Mathur, N. D., Burnell, G., Isaac, S. P., Jackson, T. J., Teo, B.-S., MacManus-Driscoll, J. L., Cohen, L. F., Evetts, J. E. & Blamire, M. G. Large low-field magnetoresistance in $La_{0.7}Ca_{0.3}MnO_3$ induced by artificial grain boundaries. *Lett. to Nat.* **387**, 266–268 (1997).

112. Wang, X. L., Dou, S. X., Liu, H. K., Ionescu, M. & Zeimetz, B. Large low-field magnetoresistance over a wide temperature range induced by weak-link grain boundaries in $La_{0.7}Ca_{0.3}MnO_3$. *Appl. Phys. Lett.* **73**, 396–398 (1998).

113. Mccormack, M., Jin, S., Tiefel, T. H., Fleming, R. M., Phillipsr, J. M. & Ramesh, R. Very large magnetoresistance in perovskite-like La-Ca-Mn-O thin films. *Appl. Phys. Lett.* **64**, 3045–3047 (1994).

114. Huang, B., Liu, Y., Zhang, R., Xiaobo-Yuan, Wang, C. & Mei, L. Low-field MR behaviour in $La_{0.67}Ca_{0.33}MnO_3/ZrO_2$ composite system. *J. Phys. D. Appl. Phys.* **36**, 1923–1927 (2003).

115. Karmakar, S., Taran, S., Chaudhuri, B. K., Sakata, H., Sun, C. P., Huang, C. L., Yang, H. D., Miao, J., Yuan, S., Karmakar, S., Taran, S., Chaudhuri, B. K., Sakata, H., Sun, C. P., Huang, C. L. & Yang, H. D. Study of grain boundary contribution and enhancement of magnetoresistance in La0.67Ca0.33MnO3/V2O5 composites. *J. Phys. D. Appl. Phys.* **38**, 3757–3763 (2005).

116. O'Donnell, J. & Rzchowski, M. S. Magnetoelastic coupling and magnetic anisotropy in $La_{0.67}Ca_{0.33}MnO_3$ films. *Appl. Phys. Lett.* **72**, 1775–1777 (1998).

117. Chen, A., Bi, Z., Hazariwala, H., Zhang, X., Su, Q., Chen, L., Jia, Q., MacManus-Driscoll, J. L. & Wang, H. Microstructure, magnetic, and low-field magnetotransport properties of self-assembled $(La_{0.7}Sr_{0.3}MnO_3)_{0.5}:(CeO_2)_{0.5}$ vertically aligned nanocomposite thin films. *Nanotechnology* **22**, 315712 (2011).

118. Sun, X., Huang, J., Jian, J., Fan, M., Wang, H., Li, Q., Macmanus-driscoll, J. L., Lu, P., Zhang, X. & Wang, H. Three-dimensional strain engineering in epitaxial vertically aligned nanocomposite thin films with tunable magnetotransport properties. *Mater. Horizons* **5**, 536–544 (2018).

119. Sun, X., Li, Q., Jian, J., Lu, P., Zhang, X., Macmanus-driscoll, J. L. & Wang, H. Strain and property tuning of the 3D framed epitaxial nanocomposite thin films via interlayer thickness variation. *J. Appl. Phys.* **125**, 082530 (2018).

120. Chen, A., Zhang, W., Khatkhatay, F., Su, Q., Tsai, C., Chen, L., Jia, Q. X., Judith, L. & Wang, H. Magnetotransport properties of quasi-one-dimensionally channeled vertically aligned heteroepitaxial nanomazes. *Appl. Phys. Lett.* **102**, 093114 (2013).

121. Zhang, W., Chen, A., Khatkhatay, F., Tsai, C., Su, Q., Jiao, L., Zhang, X. & Wang, H. Integration of Self-Assembled Vertically Aligned Nanocomposite $(La_{0.7}Sr_{0.3}MnO_3)_{1-x}$:$(ZnO)_x$ Thins Films on Silicon Substrates. *ACS Appl. Mater. Interfaces* **5**, 3995–3999 (2013).

122. Bi, Z., Weal, E., Luo, H., Chen, A., Macmanus-driscoll, J. L. & Jia, Q. Microstructural and magnetic properties of $(La_{0.7}Sr_{0.3}MnO_3)_{0.7}$:$(Mn_3O_4)_{0.3}$ nanocomposite thin films. *J. Appl. Phys.* **109**, 054302 (2011).

123. Ning, X., Wang, Z. & Zhang, Z. Controllable Self-Assembled Microstructures of $La_{0.7}Ca_{0.3}MnO_3$:NiO Nanocomposite Thin Films and Their Tunable Functional Properties. *Adv. Mater. Interfaces* **2**, 1500302 (2015).

124. Yang, H., Cao, Z. E., Shen, X., Xian, T., Feng, W. J., Jiang, J. L., Feng, Y. C., Wei, Z. Q. & Dai, J. F. Fabrication of 0-3 type manganite/insulator composites and manipulation of their magnetotransport properties. *J. Appl. Phys.* **106**, 104317 (2009).

125. Gu, J. Y., Kwon, C., Robson, M. C., Trajanovic, Z., Ghosh, K., Sharma, R. P., Shreekala, R., Venkatesan, T., Rajeswari, M. & Ramesh, R. Growth and properties of c-axis textured $La_{0.7}Sr_{0.3}MnO_{3-\delta}$ films on SiO_2/Si substrates with a $Bi_4Ti_3O_{12}$ template layer. *Appl. Phys. Lett.* **70**, 1763–1765 (1997).

126. Angeloni, M., Balestrino, G., Boggio, N. G., Medaglia, P. G., Orgiani, P. & Tebano, A. Suppression of the metal-insulator transition temperature in thin $La_{0.7}Sr_{0.3}MnO_3$ films. *J. Appl. Phys.* **96**, 6387–6392 (2004).

127. Wollan, E. O. & Koehler, W. C. Neutron Diffraction Study of the Magnetic Properties of the Series of Perovskite-Type Compounds [(1-x)La, xCa]MnO_3. *Phys. Rev.* **100**, 545–563 (1955).

128. Chahara, K., Ohno, T., Kasai, M. & Kozono, Y. Magnetoresistance in magnetic manganese oxide with intrinsic antiferromagnetic spin structure. *Appl. Phys. Lett.* **63**, 1990–1992 (1993).

129. Ranno, L., Llobet, A., Tiron, R. & Favre-Nicolin, E. Strain-induced magnetic anisotropy in epitaxial manganite manganite films. *Appl. Surf. Sci.* **188**, 170–175 (2002).

130. Nath, T. K., Rao, R. A., Lavric, D. & Eom, C. B. Effect of three-dimensional strain states on magnetic anisotropy of epitaxial thin films. *Appl. Phys. Lett.* **74**, 1615–1617 (1999).

131. Gao, X., Li, L., Jian, J., Wang, H., Fan, M., Huang, J., Wang, X. & Wang, H. Vertically Aligned Nanocomposite $BaTiO_3:YMnO_3$ Thin Films with Room Temperature Multiferroic Properties toward Nanoscale Memory Devices. *ACS Appl. Nano Mater.* **1**, 2509–2514 (2018).

132. Frit, B. & Mercurio, J. P. The crystal chemistry and dielectric properties of the Aurivillius family of complex bismuth oxides with perovskite-like layered structures. *J. Alloys Compd.* **188**, 27–35 (1992).

133. Zhang, L., Wang, W., Shang, M., Sun, S. & Xu, J. Bi_2WO_6@carbon/Fe_3O_4 microspheres: Preparation , growth mechanism and application in water treatment. *J. Hazard. Mater.* **172**, 1193–1197 (2009).

134. Yan, H., Zhang, Z., Zhu, W., He, L., Yu, Y., Li, C. & Zhou, J. The effect of (Li, Ce) and (K, Ce) doping in Aurivillius phase material $CaBi_4Ti_4O_{15}$. *Mater. Res. Bull.* **39**, 1237–1246 (2004).

135. Du, H. & Shi, X. Dielectric and piezoelectric properties of barium-modified Aurivillius-type $Na_{0.5}Bi_{4.5}Ti_4O_{15}$. *J. Phys. Chem. Solids* **72**, 1279–1283 (2011).

136. Jardiel, T., Caballero, A. C. & Villegas, M. Aurivillius ceramics: $Bi_4Ti_3O_{12}$-based piezoelectrics. *J. Ceram. Soc. Japan* **116**, 511–518 (2008).

137. Spectroscopy, P. A transmission electron microscope and group theoretical study of the new Bi-based high-T_c superconductors and some closely related Aurivillius phases. *J. Phys. C Solid State Phys.* **21**, 6067–6083 (1988).

138. Liang, J. K., Xie, S. S., Che, G. C., Huang, J. Q., Zhang, Y. L. & Zhao, Z. X. Crystal Structure and Superconductivity of $Bi_2Sr_2CaCu_2O_8$ Compound. *Mod. Phys. Lett. B* **2**, 483–489 (1988).

139. Yee, K. A., Albright, T. A., Jung, D. & Whangbo, M. Aurivillius Phases : A Possible New Class of Metal Oxide Superconductors. *Angew. Chemie Int. Ed.* **28**, 750–751 (1989).

140. Kohri, H., Kato, M., Ohsugi, I. J. & Shiota, I. Thermoelectric Generating Properties of Perovskite Like Materials. *Adv. Sci. Technol.* **74**, 72–76 (2010).

141. Kohri, H. & Yagasaki, T. Thermoelectric Generating Properties of Aurivillius Compounds. *Adv. Sci. Technol.* **77**, 285–290 (2012).

142. Naresh, G. & Mandal, T. K. Excellent Sun-Light-Driven Photocatalytic Activity by Aurivillius Layered Perovskites, $Bi_{5-x}La_xTi_3FeO_{15}$ (x = 1,2). *ACS Appl. Mater. Interfaces* **6**, 21000–21010 (2014).

143. Muktha, B., Priya, M. H., Madras, G. & Row, T. N. G. Synthesis, Structure, and Photocatalysis in a New Structural Variant of the Aurivillius Phase: $LiBi_4M_3O_{14}$ (M = Nb, Ta). *J. Phys. Chem. B* **109**, 11442–11449 (2005).

144. Kendall, K. R., Navas, C., Thomas, J. K. & Loye, H. Recent Developments in Oxide Ion Conductors : Aurivillius Phases. *Chem. Mater.* **8**, 642–649 (1996).

145. Li, L., Boullay, P., Lu, P., Wang, X., Jian, J., Huang, J., Gao, X., Misra, S., Zhang, W., Perez, O., Steciuk, G., Chen, A., Zhang, X. & Wang, H. Novel Layered Supercell Structure from Bi_2AlMnO_6 for Multifunctionalities. *Nano Lett.* **17**, 6575–6582 (2017).

146. Kim, S. & Miyayama, M. Anisotropy in oxide ion conductivity of $Bi_4V_{2-x}Co_xO_{11-\delta}$. *Solid State Ionics* **104**, 295–302 (1997).

147. Yan, H., Zhang, H., Ubic, R., Reece, M., Liu, J. & Shen, Z. Orientation dependence of dielectric and relaxor behaviour in Aurivillius phase $BaBi_2Nb_2O_9$ ceramics prepared by spark plasma sintering. *J. Mater. Sci. Mater. Electron.* **17**, 657–661 (2006).

148. Ahn, Y., Seo, J. D. & Son, J. Y. Ferroelectric domain structures of epitaxial $CaBi_2Nb_2O_9$ thin films on single crystalline Nb doped (100) $SrTiO_3$ substrates. *J. Cryst. Growth* **422**, 20–23 (2015).

149. Long, C., Fan, H., Li, M., Dong, G. & Li, Q. Crystal structure and enhanced electromechanical properties of Aurivillius ferroelectric ceramics , $Bi_4Ti_{3-x}(Mg_{1/3}Nb_{2/3})_xO_{12}$. *Scr. Mater.* **75**, 70–73 (2014).

150. Araujo, C. A.-P. de, Cuchlaro, J. D., McMillan, L. D., Scott, M. C. & Scott, J. F. Fatigue-free ferroelectric capacitors with platinum electrodes. *Lett. to Nat.* **374**, 627–629 (1995).

151. Al-Shareef, H. N., Dimos, D., Boyle, T. J., Warren, W. L. & Tuttle, B. A. Qualitative model for the fatigue-free behavior of $SrBi_2Ta_2O_9$. *Appl. Phys. Lett.* **68**, 690–692 (1996).

152. Park, B. H., Kang, B. S., Bu, S. D., Noh, T. W., Lee, J. & Jo, W. Lanthanum-substituted bismuth titanate for use in non-volatile memories. *Lett. to Nat.* **401**, 682–684 (1999).

153. Prellier, W., Singh, M. P. & Murugavel, P. The single-phase multiferroic oxides : from bulk to thin film. *J. Phys. Condens. Matter* **17**, 803–832 (2005).

154. Ramesh, R. & Spaldin, N. A. Multiferroics: progress and prospects in thin films. *Nat. Mater.* **6**, 21–29 (2007).

155. Zvezdin, A. K., Logginov, A. S., Meshkov, G. A. & Pyatakov, A. P. Multiferroics: Promising Materials for Microelectronics, Spintronics, and Sensor Technique. *Bull. Russ. Acad. Sci. Phys.* **71**, 1561–1562 (2007).

156. Uratani, Y., Shishidou, T. & Oguchi, T. First-Principles Study on the Magnetic Anisotropy in Multiferroic $PbVO_3$ and $BiCoO_3$. *J. Phys. Soc. Japan* **78**, 084709 (2009).

157. Zhai, L. & Wang, H. The magnetic and multiferroic properties in $BiMnO_3$. *J. Magn. Magn. Mater.* **426**, 188–194 (2017).

158. Jeen, H., Singh-Bhalla, G., Mickel, P. R., Voigt, K., Morien, C., Tongay, S., Hebard, A. F. & Biswas, A. Growth and characterization of multiferroic $BiMnO_3$ thin films. *J. Appl. Phys.* **109**, 074104 (2011).

159. Wang, H. H., Li, L., Huang, J., Gao, X., Sun, X., Zemlyanov, D. & Wang, H. H. Two-Phase Room-Temperature Multiferroic Nanocomposite with $BiMnO_3$-Tilted Nanopillars in the $Bi_2W_{1-x}Mn_xO_6$ Matrix. *ACS Appl. Mater. Interfaces* **11**, 26261–26267 (2019).

160. Wang, H. H., Li, L., Huang, J., Gao, X., Sun, X. & Wang, H. H. Multiferroic vertically aligned nanocomposite with $CoFe_2O_4$ nanocones embedded in layered Bi_2WO_6 matrix. *Mater. Res. Lett.* **7**, 418–425 (2019).

161. Ismailzade, I. H., Aliyev, I. M., Ismailov, R. M., Alekberov, A. I. & Rzayev, D. A. Ferroelectricity in Bi_2MoO_6. *Ferroelectrics* **22**, 853–854 (1979).

162. Zhang, M., Shao, C., Mu, J., Zhang, Z., Guo, Z., Zhang, P. & Liu, Y. One-dimensional Bi_2MoO_6/TiO_2 hierarchical heterostructures with enhanced photocatalytic activity. *CrystEngComm* **14**, 605–612 (2012).

163. Umapathy, V., Manikandan, A., Antony, S. A., Ramu, P. & Neeraja, P. Structure, morphology and opto-magnetic properties of Bi_2MoO_6 nano-photocatalyst synthesized by sol−gel method. *Trans. Nonferrous Met. Soc. China* **25**, 3271–3278 (2015).

164. Yin, W., Wang, W. & Sun, S. Photocatalytic degradation of phenol over cage-like Bi_2MoO_6 hollow spheres under visible-light irradiation. *Catal. Commun.* **11**, 647–650 (2010).

165. Lisjak, D. & Mertelj, A. Anisotropic magnetic nanoparticles: A review of their properties, syntheses and potential applications. *Prog. Mater. Sci.* **95**, 286–328 (2018).

166. Daboo, C., Hicken, R. J., Gu, R., Gester, M., Gray, S. J., Eley, D. E. P., Ahmad, E. & Bland, J. A. C. Anisotropy and orientational dependence of magnetization reversal processes in epitaxial ferromagnetic thin films. *Phys. Rev. B* **51**, 15964–15973 (1995).

167. Lee, H. N. & Hesse, D. Anisotropic ferroelectric properties of epitaxially twinned $Bi_{3.25}La_{0.75}Ti_3O_{12}$ thin films grown with three different orientations. *Appl. Phys. Lett.* **80**, 1040–1042 (2002).

168. Tocci, M. D., Bloemer, M. J., Scalora, M., Dowling, J. P. & Bowden, C. M. Thin-film nonlinear optical diode. *Appl. Phys. Lett.* **66**, 2324–2326 (1995).

169. Seiberle, H., Benecke, C. & Bachels, T. Photo-aligned anisotropic optical thin films. *J. SID* **12**, 87–92 (2004).

170. Liu, Z., Lee, H., Xiong, Y., Sun, C. & Zhang, X. Far-Field Optical Hyperlens Magnifying Sub-Diffraction-Limited Objects. *Science (80-.).* **315**, 1686 (2007).

171. Rho, J., Ye, Z., Xiong, Y., Yin, X., Liu, Z. & Choi, H. Spherical hyperlens for two-dimensional sub-diffractional imaging at visible frequencies. *Nat. Commun.* **1**, 143 (2010).

172. Jacob, Z., Alekseyev, L. V & Narimanov, E. Optical Hyperlens: Far-field imaging beyond the diffraction limit. *Opt. Express* **14**, 8247–8256 (2006).

173. Guo, Y., Cortes, C. L., Molesky, S. & Jacob, Z. Broadband super-Planckian thermal emission from hyperbolic metamaterials. *Appl. Phys. Lett.* **101**, 131106 (2012).

174. Yang, X., Yao, J., Rho, J., Yin, X. & Zhang, X. Experimental realization of three-dimensional indefinite cavities at the nanoscale with anomalous scaling laws. *Nat. Photonics* **6**, 450–454 (2012).

175. Poddubny, A., Iorsh, I., Belov, P. & Kivshar, Y. Hyperbolic metamaterials. *Nat. Photonics* **7**, 958–967 (2013).

176. Jacob, Z., Kim, J.-Y., Naik, G. V., Boltasseva, A., Narimanov, E. E. & Shalaev, V. M. Engineering photonic density of states using metamaterials. *Appl. Phys. B* **100**, 215–218 (2010).

177. Gao, J., Wu, X., Li, Q., Du, S., Huang, F., Liang, L., Zhang, H., Zhuge, F., Cao, H. & Song, Y. Template-Free Growth of Well-Ordered Silver Nano Forest/Ceramic Metamaterial Films with Tunable Optical Responses. *Adv. Mater.* **29**, 1605324 (2017).

178. Shekhar, P. & Jacob, Z. Strong coupling in hyperbolic metamaterials. *Phys. Rev. B* **90**, 045313 (2014).

179. Su, Q., Zhang, W., Lu, P., Fang, S., Khatkhatay, F., Jian, J., Li, L., Chen, F., Zhang, X., MacManus-Driscoll, J. L., Chen, A., Jia, Q. & Wang, H. Self-Assembled Magnetic Metallic Nanopillars in Ceramic Matrix with Anisotropic Magnetic and Electrical Transport Properties. *ACS Appl. Mater. Interfaces* **8**, 20283–20291 (2016).

180. Misra, S., Li, L., Zhang, D., Jian, J., Qi, Z., Fan, M., Chen, H., Zhang, X. & Wang, H. Self-Assembled Ordered Three-Phase Au–BaTiO$_3$–ZnO Vertically Aligned Nanocomposites Achieved by a Templating Method. *Adv. Mater.* **31**, 1806529 (2019).

181. Huang, J., Wang, X., Phuah, X. L., Lu, P., Qi, Z. & Wang, H. Plasmonic Cu nanostructures in ZnO as hyperbolic metamaterial thin films. *Mater. Today Nano* **8**, 100052 (2019).

182. Steenbeck, K., Habisreuther, T., Dubourdieu, C. & Senateur, J. P. Magnetic anisotropy of ferromagnetic La$_{0.7}$Ca$_{0.3}$MnO$_3$ epitaxial thin films: Dependence on temperature and film thickness. *Appl. Phys. Lett.* **80**, 3361–3363 (2002).

183. Lee, H. & Park, H. Band Structure Analysis of La$_{0.7}$Sr$_{0.3}$MnO$_3$ Perovskite Manganite Using a Synchrotron. *Adv. Condens. Matter Phys.* **2015**, 746475 (2015).